ABSTRACT

Title of Document:	ELLIPTIC FLOW MEASURED WITH THE PHOBOS SPECTROMETER AT RHIC
	Richard Thomas Bindel, Doctor of Philosophy, 2008
Directed By:	Professor Alice C. Mignerey Department of Chemistry and Biochemistry

The Relativistic Heavy Ion Collider (RHIC) at Brookhaven National Laboratory provides experiments with the most energetic nucleus-nucleus collisions ever achieved in a laboratory. These have been used to investigate the phase diagram of nuclear matter at very high temperature and low baryon chemical potential. Under such conditions, quantum chromodynamics predicts a deconfinement of quarks from their hadronic boundaries, and this is believed to result in a phase transition to a quark gluon plasma (QGP).

The characterization of the substance in a microscopic collision system is difficult because the matter undergoes significant changes as it rapidly inflates and cools. The collective expansion of the medium perpendicular to the collision axis is a revealing feature that can be related to the early stages of the system evolution. Arising as a consequence of the natural spatial asymmetry in non-head-on collisions, the back-to-back "elliptic flow" is a particularly informative mode of the expansion.

The collective movement is characterized in terms of the relaxation of a compressed liquid. The magnitude of the elliptic flow constrains the parameters of various hydrodynamics-based models, and these suggest that the matter behaves as an ultra low-viscosity liquid, achieving local thermal equilibrium very early in the collision evolution.

This thesis presents measurements of the elliptic flow anisotropy parameter, v_2, for Au+Au and Cu+Cu collisions at center-of-mass energies of 200 GeV and 62 GeV per nucleon pair. The data was taken at the PHOBOS experiment at RHIC using the spectrometer in conjunction with the ring and octagon multiplicity detectors.

A Monte Carlo Glauber model is used to establish the eccentricity of the overlap region in non-head-on collisions. When this geometry is taken into account, the elliptic flow is shown to evolve smoothly between collision systems. This behavior is evident, not only in the elliptic flow as a function of reaction centrality, but also as a function of the transverse momentum. The agreement lends support to the prevailing theory of a smooth progression with increasing system size and collision energy towards a hydrodynamic limit.

ELLIPTIC FLOW MEASURED WITH THE PHOBOS SPECTROMETER AT RHIC

By

Richard Thomas Bindel

Dissertation submitted to the Faculty of the Graduate School of the
University of Maryland, College Park, in partial fulfillment
of the requirements for the degree of
Doctor of Philosophy
2008

Advisory Committee:
Professor Alice C. Mignerey, Chair / Advisor
Professor Thomas D. Cohen
Professor Sang Bok Lee
Professor Amy S. Mullin
Professor William B. Walters

for Sarah

Table of Contents

List of Tables

List of Figures

Chapter 1: Introduction to Relativistic Heavy Ion Physics

1.1: A chemist's interest in nuclear physics

The forerunner of chemistry, alchemy, was purely an empirical pursuit, and of course it was concerned less with understanding matter and more with transmuting lead into gold. At its inception, chemistry was a conglomerate of observations and cobbled-together rules, each one with little predictive power beyond its own immediate domain. For example, it became clear that reactants are consumed in fixed proportions, but those proportions could not be found *a priori*. The periodic behavior of the elements was the first important discovery that fostered a broad understanding of observable chemical phenomenon. Even more so, in the 20th century, the quantum depiction of the atomic world (along with the venerable subjects of thermodynamics and statistical mechanics) established a set of first principles from which chemical behavior could be predicted. In one sense, the modern age of chemistry was ushered in with the introduction of these fundamental and, therefore, broadly applicable principles. Yet a quantum description will lead the chemist only exactly as far as the Hamiltonian of a Hydrogen atom. It is in approximations and the messy exceptions rather than a handful of immutable rules where the complexities of chemistry flourish.

In contrast, the field of particle physics has a reductionist bent by necessity, and the distillation of the subject has led to a model of amazing breadth and accuracy. Several decades ago, the science that arguably began with Rutherford's scattering experiment was in crisis. From numerous studies using energetic cosmic rays, and from results driven by the recent success of particle accelerators, a myriad of apparently

elementary particles had been discovered. The sizable collection (which is now large enough to fill an annually published handbook) was appropriately referred to as the "particle zoo". A theory was sorely needed to bring order to the growth. In 1964 Murray Gell-Mann and George Zweig proposed that these many seemingly elementary particles were themselves composites of yet lesser particles, quarks. The theory did not gain immediate traction, since the postulated fractionally charged quarks could not be found. Yet at the end of the decade, an experiment strongly analogous to Rutherford's showed that protons, particles previously thought to be fundamental, indeed have internal structure. The experiment was the deep inelastic scattering of electrons on a proton target, and the small internal objects were given the moniker "partons" by Richard Feynman. By the time the appropriate corrections had been applied to the preliminary results, it was clear that partons and quarks were (and are) one and the same. Quarks became a mainstay of particle physics, a cornerstone of the extraordinarily accurate model of fundamental matter. (For a historical perspective see [Rio92].)

Nuclear physics has ties to both subjects. It has the complexities of chemistry, the tools of particle physics, and the mutual goal of understanding matter. To a chemist, who is initiated to the field through studies of Uranium bearing ores, the decay properties of nuclei are of central importance. However, decay is dictated by structure. Naturally, there are certain quantum mechanical rules that play a role in the structure. Protons and neutrons are fermions, filling energy levels of the nucleus based on unique sets of quantum numbers, just as electrons fill the atomic energy levels. Other aspects of the nuclear structure are less distinct, and empirical descriptions must be found. The structure of an *unstable* nucleus can be investigated to some extent by characterizing its

emissions. Yet to access excited states or probe otherwise *stable* nuclei, some external disturbance is needed. Just as molecular spectroscopy uses light, nuclear studies use particles to perturb and probe a nucleus. The energy at which a projectile is absorbed and likewise the energy of any subsequent emissions are both important in understanding structure, just as absorption and emission are used in optical measurements.

This thesis focuses on a high-energy subset of nuclear physics involving the force that holds the nucleus together as well as the interactions of quarks. A common progression in nuclear and particle physics is to use projectiles to probe for physical structures, then to vary the projectile speed to look for energy levels (spectroscopy), and finally, to seriously deform, shatter, or annihilate a projectile and target and observe the outcome. This research takes the latter approach. Fast electrons impinging on protons revealed the presence of quarks decades ago, but such experiments are not sufficient to understand the behavior of quark-quark interactions (the reasons for which will be covered shortly). To do so requires large populations of freely interacting quarks, and this can be achieved in the laboratory by colliding large nuclei at very high relative kinetic energies. Rather than the low-energy probes exploited in nuclear spectroscopy, the goal here is to impart a tremendous amount of energy into a body of nuclear material. With enough energy, the nuclear medium is theorized to melt, revealing the nature of interactions among quarks and the particles called gluons that bind them together. In contrast to the austere billiard-ball experiments of particle physics, high-energy nuclear collisions involve an exceptional number of degrees of freedom, and they are frequently characterized in terms of thermal and chemical equilibrium. It is in this messy, complex phase of matter that a chemist's experience contributes.

1.2: The standard model: matter

The cornerstone of fundamental physics is the standard model, which describes the elementary particles of matter and their interactions. It is a remarkable incorporation of several well-developed theories under a single mathematical framework, and it has been rigorously tested for over three decades. As evidence of its success, the model has predicted the existence of several fundamental particles before their experimental discovery, and, for a myriad of well-measured observables, only a very few contradictions between theory and experiment have arisen.

According to the standard model, the material that makes up the universe is constructed from a dozen spin $\pm\frac{1}{2}\hbar$ fermions. The fermions are divided equally into two families: *quarks* and *leptons*. Additionally, a handful of spin $\pm 1\hbar$ bosons convey the four fundamental forces through which the particles interact.

Table 1.1 gives the name, symbol, and electric charge of each member of the lepton family. Each charged lepton and corresponding neutrino makes up one of three *generations* of leptons (the three rows of Table 1.1), and each of these particles, having a different set of quantum numbers, is said to have a different *flavor*. The massive muon and tau are rarely observed because they quickly decay into the much lighter electron.

Table 1.1: Leptons and their Properties

Name	Symbol	Electrical Charge
electron	e	-1
muon	μ	-1
tau	τ	-1

Name	Symbol	Electrical Charge
electron neutrino	υ_e	0
muon neutrino	υ_μ	0
tau neutrino	υ_τ	0

Table 1.2 shows the members of the quark family. Like the leptons, the family is divided into three generations, and again each particle is described as a having a different flavor. Each generation is increasingly massive, so the down and up quarks are relatively light, while the bottom and top quarks are the heaviest. The heavier quarks quickly decay into the lighter down and up quarks, which therefore make up the ground state matter around us. Protons, for example, are made of two up quarks and a down quark, while two down quarks and an up quark make a neutron.

Table 1.2: Quarks and their Properties

Name	Symbol	Electrical Charge
down	d	-1/3
strange	s	-1/3
bottom	b	-1/3

Name	Symbol	Electrical Charge
up	u	+2/3
charm	c	+2/3
top	t	+2/3

Each of these fermions also has an antimatter counterpart, most notably characterized by its opposite charge. An important consequence of $E=mc^2$ is that, given sufficient energy, particle-antiparticle pairs can be created, and inversely, they can annihilate to release energy. For example, a very energetic photon (more than 1.022 MeV) can produce an electron and its antiparticle, a *positron*, each of which has a mass of 0.511 MeV/c^2. This point is very important in understanding highly energetic collisions, though it is not necessarily intuitive to chemists, who generally work in the regime of interactions of a few eV.

1.3: The standard model: forces

According to quantum field theory, the interactions among the above fermions are themselves mediated by other particles. The four forces by which particles interact are the strong force, the electromagnetic force, the weak force, and the gravitational force. Gravity is so weak in comparison to the other forces that, in a microscopic view, it has no observable effect.

The relative strengths of the remaining three forces are compared by means of their respective, dimensionless *coupling constants*. These, along with the natural length scales over which the forces act, are given in Table 1.3 [Roh94].

Table 1.3: The Strengths of Three Fundamental Forces

Name	Symbol	Strength	Length Scale
strong	α_S	1	10^{-15}
electromagnetic	α	7×10^{-3}	infinite
weak	α_W	10^{-6}	10^{-16}

The weak force, as its name suggests, does not produce a significantly forceful interaction among particles, and it also has a limited range (roughly 10^{-16} m). The range arises due to the mass of the bosons that convey the force: the W^{+1}, W^{-1}, and Z^0. These messenger particles require an amount of energy equivalent to their mass to come into existence. This energy can be "borrowed" as long as it is "returned" [1] within the brief time dictated by Heisenberg's uncertainty principle, $\Delta E\, \Delta t \geq \frac{1}{2}\hbar$. In turn, traveling at the speed of light for the time interval Δt dictates the distance spanned by the force. This is a useful example, because the motif of transient virtual particles is a recurring theme in our

[1] "Borrow" and "return" are used in lieu of the more formal terminology, "transient energy conservation".

understanding of fundamental physics. In fact, despite its colloquial meaning, physicists consider a "vacuum" to be full of virtual particles, blinking in and out of existence as dictated by the uncertainty principle. As was the case before, the amount of energy in question is the energy equivalent of the mass of the particle, given by the equation $E=mc^2$.

Though the weak force is feeble, its microscopic effect is easily observed. It is not an attractive force. Instead, it is the only force that can change the flavor of one quark into another (down to up for example). A notable example of this effect is the beta decay of the neutron into the proton, depicted in Fig. 1.1. The weak force acts on both quarks and leptons, yet despite its broad influence, it has the peculiarity of preferentially acting on left-handed (spin = $-\frac{1}{2}\hbar$) matter.[1]

[1] The "handedness" of the weak force is known as a *parity symmetry violation*. Conceptually this can be visualized as a physical process (β^- decay, for example) that can be distinguished from its mirror image (when the angular momentum of the parent nuclei is aligned in a magnetic field for example).

In his famous lecture series [Fey63], Feynman presents an amusing parable regarding handedness. It supposes that you (yes, you dear reader) contact an extraterrestrial being, and that a beam of light is used as a sort of celestial telegraph. You build the basis of communication, starting with prime numbers, and continuing with increasing complexity. The average height of a human could be communicated for example using wavelengths as a meter stick, and a light-frequency clock could communicate the average human lifespan. In preparation for ultimately meeting the alien, you describe how to shake hands in greeting. "Extend your right hand," you say, to which the alien responds, "What is right?" Using the handedness of the weak decay, you could describe an experiment to convey this information to the aliens. However, if the experiment were performed with antimatter, it would express the opposite behavior. Therefore the parable urges caution; upon meeting your alien counterpart, do not accept the kind gesture if it extends its left hand!

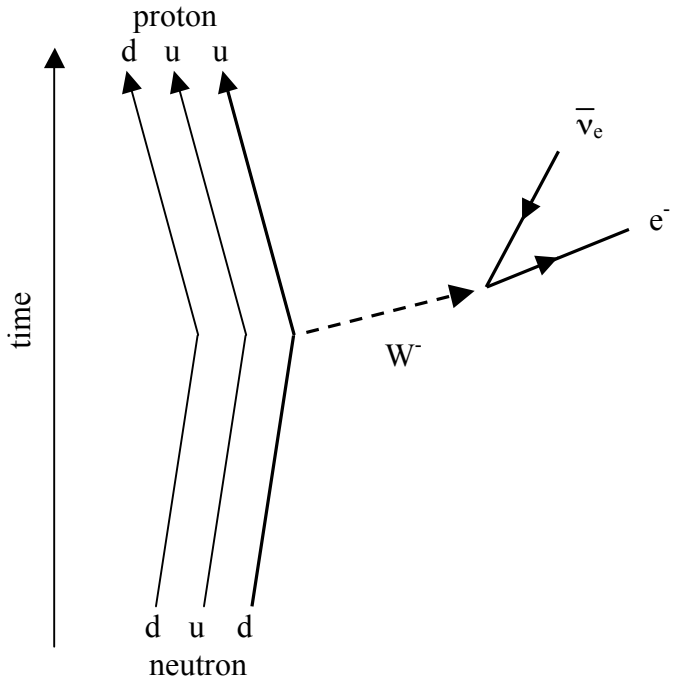

Figure 1.1: A Feynman diagram of the beta decay of a neutron into a proton. Notice that in its decay to a proton, one of the quark constituents of the neutron changes from 'd' to 'u'. This is an example of the weak force. (Adapted from [Gri89].)

Among the four forces, the quantum depiction of the electromagnetic force is certainly the most familiar to chemists. It is mediated by the massless photon, γ, which interacts with charged particles. This force has been well understood for many decades, and is the subject of the field of quantum electrodynamics (QED). QED has successfully withstood experimental scrutiny to levels of precision surpassed only by measurements of general relativity, and it is by far the most well understood component of the standard model. Finally, the strong force binds quarks together, and it is mediated by the exchange of massless bosons called *gluons*. In analogy to electrical charge, quarks carry color charge designated as red, green, and blue and oppositely, anti-red, anti-green, and anti-blue. The theory of color charge and strong interactions is called quantum chromodynamics, or

QCD (in parallel to the previously mentioned quantum electrodynamics). Quarks are bound together by gluons in groups of two or three to form color neutral particles called *hadrons*. Beyond the requirement of global color neutrality, the similarity to electrical charge breaks down. Unlike photons, which are uncharged and do not transmit electrical charge, gluons themselves carry an intrinsic color charge (or, rather, a combination of a color charge and an anti-color charge[1]), and, moreover, they actually shuttle color charge between quarks. The need for a color charge quantum number is clear when considering particles with two otherwise identical quarks, *e.g.* the two degenerate down quarks inside a neutron. Quarks are fermions, and fermions cannot share the same set of quantum numbers. Therefore, the color quantum number is necessary to distinguish between the two particles.

Hadronic particles are further subdivided according to the number of constituent quarks, as shown in Table 1.4. Groups of two are called *mesons*, and groups of three (such as the proton and neutron in Fig. 1.1) are called *baryons*. Mesons are comprised of a quark and an anti-quark pair, and they carry a color charge and corresponding anti-color charge. This makes the bound particle color neutral. Baryons, have three quarks and the RGB combination leads to color neutrality (*i.e.* analogous to the sum of colors in a color wheel producing white). Alternatively, baryons may have three anti-quarks, and therefore an anti-RGB color combination.

[1] For example, a green quark emits a green/anti-red gluon to become a red quark. This way color charge is always conserved. Like fractional electric charge, color charges have never been observed, and, therefore, particles must be color neutral.

Table 1.4: The Two Types of Hadrons

Type of Hadron	Quark and Anti-quark Makeup
Meson	$q\bar{q}$
Baryon	qqq or $\bar{q}\bar{q}\bar{q}$

The color carrying nature of gluons leads to some unexpected properties of the strong force. Again, an analogy with the electromagnetic force is useful in illustrating those unexpected features. Electrical screening (*i.e.* Debye screening) is familiar to a chemist, for example in the context of ionic solutions. Even in non-ionic, polar liquids such as water, the positive ends of nearby dipoles will orient towards a negative charge. A sphere drawn around the negative charge tends to be slightly positive, and this gives rise to the charge screening. Surprisingly, a similar screening exists even in what is classically thought of as a vacuum. Virtual electron/positron pairs populate the vacuum, and they are able to screen electric charge even though they exist only momentarily [Com95]. Virtual quark/anti-quark pairs might be expected to screen color charge in a similar mechanism, but, quite differently, the color-carrying gluon field itself becomes polarized. The result is generally described as anti-screening[1], and it implies that, as two color charged particles are drawn apart, the force between them does not diminish [Ols86]. Consequently, the potential energy of the quark pair increases with increasing

[1] Charge screening and anti-screening can be conceptualized in analogy to the behaviors of diamagnetic and paramagnetic materials in an external magnetic field. These behaviors result from the coupling of the field with either the total orbital angular motion of the electron in the case of diamagnetic material, or with the spin of an unpaired electron in the case of paramagnetic material. In diamagnetic material, an external field influences the electron orbit, and the tiny induced magnetic moment is in opposition to the field. The electrical analog to this magnetic picture is charge screening. Paramagnets are familiar to a chemist as arising from unpaired electrons, and the spin of such an electron aligns so that the induced magnetic field propagates the applied field. The color charge analog to this picture is anti-screening. [Nie81, Hug81]

distance, and, unlike an electrically charged pair of particles, infinite energy would be required to infinitely separate two color charges.

A qualitative functional depiction of the strong force potential between quarks, evaluated for a heavy meson, is shown in Fig. 1.2. A cartoon illustrating the force lines for the strong force and electromagnetic force is provided in Fig. 1.3.

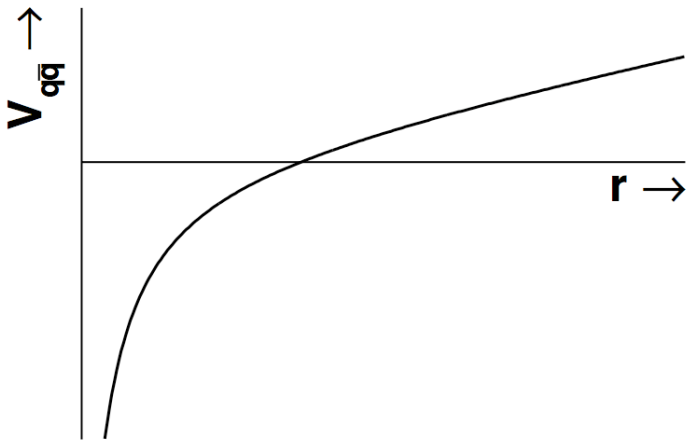

Figure 1.2: The energy potential between quark and anti-quark as a function of separation distance [Ols86].

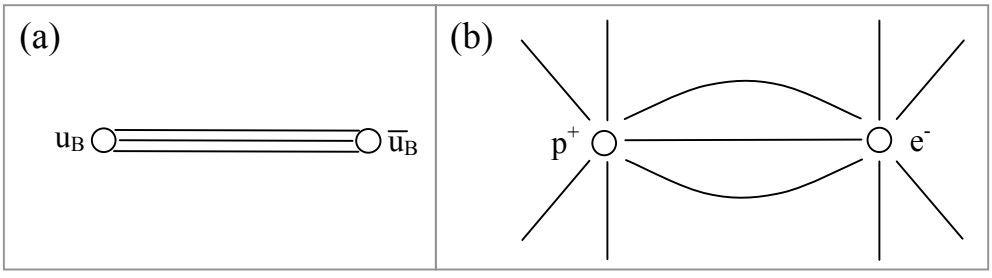

Figure 1.3: Frame (a) shows the force lines drawn between two color charged particles (a 1-dimensional tube). In frame (b), the force lines are shown between two electrically charged particles (isotropic in 3 dimensions). The intercepted lines (and therefore the force) remain constant between color charges, while it drops as $1/r^2$ for electrical charges. (Adapted from [Roy99].)

Conversely, when the distance between quarks is small, there is little anti-screening from an intervening gluon field, and the energy required for quarks to move about diminishes. This unfettered movement within small distances is called *asymptotic freedom* [GW75] (a profound mathematical discovery that led to the 2004 Nobel Prize in physics). This theory considers the strong force coupling constant as a *running coupling constant*, which is to say that it is constant at large distances but it becomes smaller when quarks are nearby. The MIT bag model is a common depiction of quark aggregation, presenting a picture of hadrons as elastic bag boundaries in which massless quarks are free to move without any particular structure [Cho74].

Interestingly, the attractive force among protons and neutrons within the nucleus is a secondary effect, and yet it is still comparable to, or stronger than the electrical repulsion between the positively charged protons. Protons and neutrons are color neutral, so, unlike the color charged quarks, they are not inherently bound by the strong force. However, the movement of color charges within these hadrons creates temporary color dipoles, and the nucleus is therefore held together through the strong force equivalent of the van der Waals attraction.

As a final, yet most significant point, though the potential energy increases linearly beyond small distances, the bond can still be broken. In generic terms, Rutherford's gold foil experiment showed that a stream of sufficiently energetic projectiles is able to probe for smaller internal particles. At even higher energies, an impinging projectile can be used to knock out one of these constituent particles. What happens when a single quark is jarred by a forceful collision? The result of such an experiment is shown as a cartoon in Fig. 1.4.

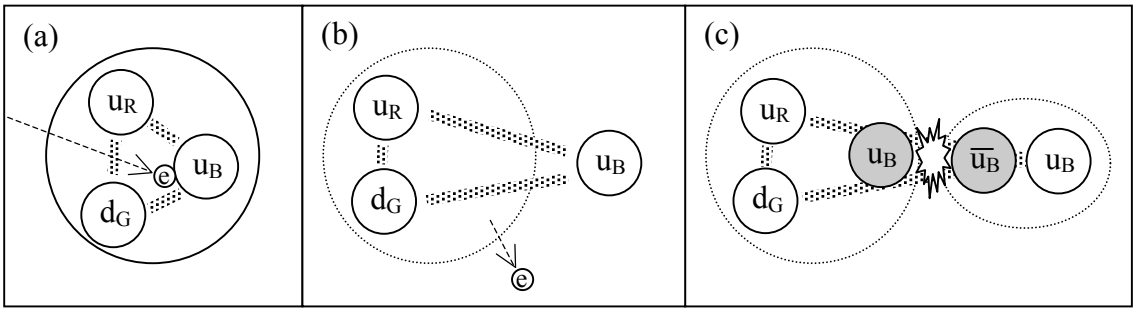

Figure 1.4: A cartoon of the high-energy impact of an electron on a proton. In each frame, the large, encompassing circles are meant to delineate the hadronic boundary (*i.e.* the bag surrounding the quarks). Shaded lines represent the strong force attraction. In frame (a), an electron strikes a single quark. In frame (b), as the quark is pushed away, the potential energy held in the color field increases. By frame (c), the color field holds so much energy that it snaps, and the energy is converted into a new matter/antimatter pair of quarks. (To help identify these quarks, the newly produced $u\bar{u}$ pair is shaded gray.) This produces a meson (in this case, a π^0), as well as regenerating the original proton.

At sufficient energies, a quark can be struck such that the energy stored in the color field becomes greater than the energy needed to generate a new quark/anti-quark pair.[1,2] So, while the function for the potential energy in the color field continues to rise, the situation of infinite energy at infinite separation is not a physical limit since the bond will ultimately break [Cas79].

[1] Interestingly, this is not the only instance of a field snapping to bring a pair of otherwise virtual particles into existence. With a high enough electric field, a virtual electron/positron pair will become real particles as they "spark" the vacuum.

[2] This sort of experiment raised problems with the long held idea that a fundamental particle is a thing that can be knocked out of another thing. Mesons came out of collisions of protons, and protons and anti-protons came out of collisions of mesons. Now it is clear that neither one is elementary.

1.4: Exploring the QCD phase diagram

The previous sections dealt purely with the fundamental physics of particles and their interactions. This section deals with matter in a manner that is more familiar to chemists. The phase diagram in Fig. 1.5 shows some configurations of QCD matter (that is matter made up of quarks and held together by gluons).

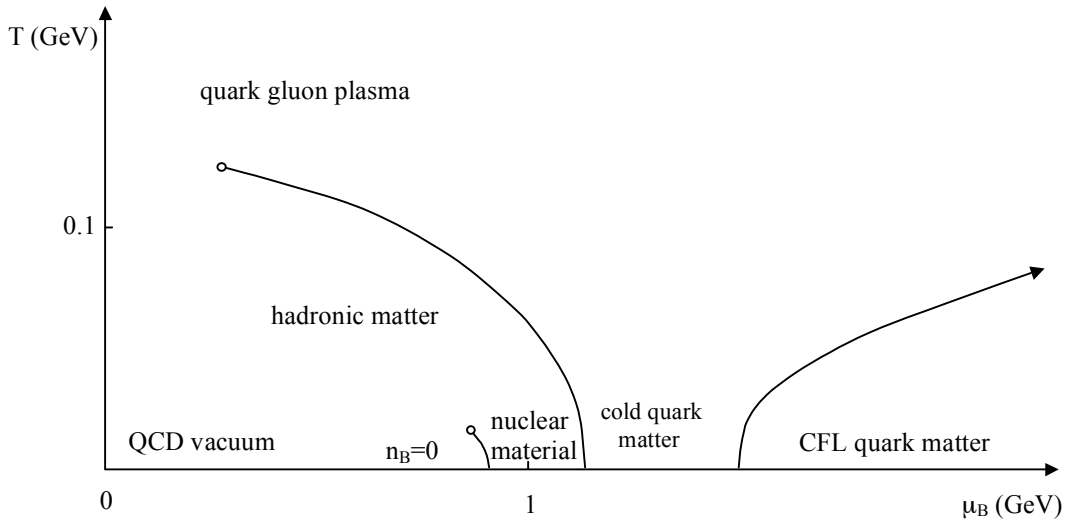

Figure 1.5: The QCD phase diagram. (Adapted from [Step04] and [Han01].)

Before each region of the phase diagram is described, the axes bear some measure of explanation. Temperature is an expression of the energy of the medium per degree of freedom, scaled by an appropriate Boltzmann constant. (As a matter of comparison, using the equation $E=kT$, where $k = 8.617\times10^{-5}$ eV/K, reveals that 0.1 GeV corresponds to roughly 1.2 billion Kelvin.) The matter has some degrees of freedom that are generally unfamiliar to chemists, namely that energy can be turned into mass as equal parts matter and antimatter. This will be discussed in further detail momentarily. Also,

instead of describing the system using temperature, sometimes it is simply stated in terms of energy density (which encompasses both mass energy and kinetic energy).

On the horizontal axis, baryon chemical potential μ_B is the change in the energy of the system as the baryon number n_B is changed (and all other thermodynamic variables are held constant). Recall that among the hadrons, mesons have equal parts matter and antimatter, while baryons are entirely one or the other. Since our environment is made of matter, the baryon number is the net excess of matter (counted in terms of baryons), and therefore the conjugate variable μ_B is an energy expression of the imbalance of matter over antimatter. Some phase diagrams choose baryon *density* as the horizontal axis, and this is a useful mental comparison to make. The baryon chemical potential increases with increasing baryon density, so the phase diagram regions maintain the same ordering. However, μ_B is generally chosen because the phase boundaries are lines, whereas in terms of density the phase transitions are regions.[1]

The cold QCD vacuum resides in the lower left hand corner, at low temperatures and equal abundance of matter and antimatter. The lowest limit of the temperature axis corresponds to empty space, since the presence of matter and antimatter produces energy upon annihilation (and therefore finite temperature). However, for the sake of bookkeeping, the vacuum is still populated with virtual particle/anti-particle pairs as dictated by the uncertainty principle. In other words, even at zero temperature there is the transient appearance of energy.

As temperature increases along the vertical axis, equal parts matter and antimatter begin appearing. Virtual quark/anti-quark pairs coalesce as mesons (along with the

[1] A familiar comparison would be the melting of ice into liquid water. The density changes but the chemical potential remains constant throughout the phase change.

introduction of non-QCD matter such as unbound electron/positron pairs). The color bonds between these pairs stretch as the quarks gain thermal motion. When the bonds are stretched with sufficient energy, they may snap (as shown previously in Fig. 1.4), generating in their place new quark/anti-quark pairs. The π^0 meson, which was briefly mentioned in Sec. 1.3, is one of three particles called *pions*. Pions are mesons formed solely from up and down quarks and anti-quarks.[1] They are the lightest form of QCD matter (about $1/7^{th}$ the mass of a proton), and therefore, they are the most populous in a thermal distribution. Again, mass is coupled to energy, so a thermal distribution implies not only a Boltzmann energy distribution, but also ratios of populations of particles dictated by their respective masses. The region, above the vacuum and below the quark gluon plasma, along the vertical axis, is generally described as a pion gas. To a lesser extent, and more so as the temperature increases, heavier mesons containing strange quarks and also baryon/anti-baryon pairs will exist. The populations are described using a grand canonical ensemble in which different species are allowed to enter and leave as determined by their respective chemical potentials. A few examples of particles, including some heavy mesons and baryons, are provided in Appendix D.

As the temperature increases further, more energy is converted into particles. In addition, (in a classical depiction) one can imagine that the bag-like boundaries of the hadrons expand as the quarks inside them gain increasing thermal motion. Though quarks are confined within hadrons when particles are sparse, something different happens as the particle density increases. When hadrons are crowded with other hadrons, the quarks inside become equally attracted to quarks in nearby particles. The medium

[1] The pions, π^+ and π^-, are $u\bar{d}$ and $\bar{u}d$ respectively, and π^0 is $d\bar{d}$ or $u\bar{u}$ (or, rather the mixing $(u\bar{u} - d\bar{d})/\sqrt{2}$).

changes from a phase in which the hadrons (mesons and also baryon/anti-baryon pairs) are distinguishable, to one in which the boundaries have melted away. This is shown in Fig. 1.6.

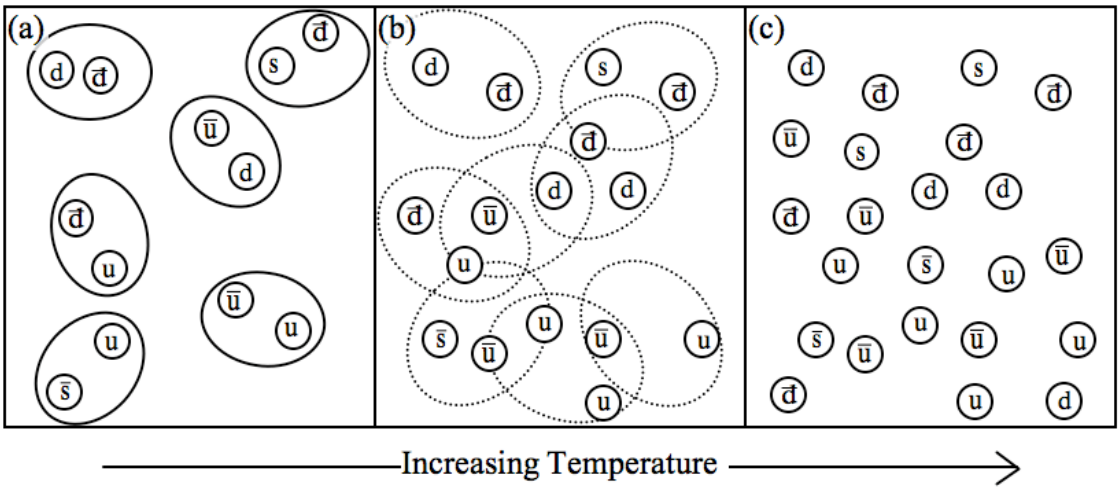

Figure 1.6: A cartoon depicting hadronic matter transitioning into quark matter as the temperature increases at zero baryon chemical potential. In frame (a), quarks are bound in discrete hadrons. These are predominantly light mesons. In frame (b), as the particle density increases, it becomes less clear which quarks belong to which hadrons. Finally, in (c), a quark density has been achieved so that each quark is attracted to multiple quarks around it, rather than being bound to one or two partners within a hadron.

The quarks are equally attracted to quarks in all directions, and the previously mentioned idea of asymptotic freedom suggests that they are free to move about without constraint. This freedom of quarks at high temperature is colloquially described as the "melting" of the QCD vacuum. At low baryon chemical potential, current theory predicts no discrete phase boundary between the hadronic medium and the quark matter. Since the color charges are free to move throughout the medium, this high-temperature phase of quark matter is generally described as a *quark gluon plasma* (QGP).[1] Initially the QGP was theorized to be gas-like, with minimal interaction between the constituent particles.

[1] Of course, this is in analogy to conventional plasmas in which electrical charges are free to move about.

Recent experimental evidence suggests that a form of QGP exists in which the constituents interact – more like a fluid than a gas. Weakly interacting QGP (wQGP) and strongly interacting QGP (sQGP) are descriptors that have developed to distinguish the two behaviors (the former gaseous and non-interacting, and the latter liquid-like and self-interacting).

The theoretical tools used to describe QCD matter are various numerical calculations based on lattice gauge theory [Cre83]. These have been used to aid in the search for the QGP critical point, although at finite baryon chemical potential these calculations are difficult. The value of T_c is thought to lie between 150 to 200 MeV, or alternatively at an energy density of around 1 GeV/fm^3. (For example, T_c = 175 MeV, or an energy density of 700 MeV/fm^3 ± 50%, is suggested in [Kar02].) Interestingly, an energy density of 1 GeV/fm^3 is less than an order of magnitude greater than the energy density of a proton (~500 MeV/fm^3) or the energy density of a nucleus (~150 MeV/fm^3) [Ani80].

Beginning at the QCD vacuum, increasing μ_B is yet another way to access a quark matter phase (albeit cold, and not necessarily a plasma). First, at low T and μ_B around 0.94 GeV there is a phase transition to normal nuclear matter (in which hadrons are cohesive, forming nuclei). Recall that μ_B is the change in energy of the system as the baryon number increases. Protons and neutrons are the lightest baryons, so the energy equivalent to their mass (roughly 0.94 GeV) is the minimum possible energy change with the addition of a baryon (at low T). Since this is the smallest physical limit of μ_B in a system containing discrete amounts of baryonic matter, the area to the left of this transition on the phase diagram is QCD vacuum. Our immediate environment lies on this

phase transition line at very low temperature. The nuclei of atoms around us behave as a mixed phase – droplets of baryonic matter (roughly $\rho \approx 1.4$ baryons/fm^3) surrounded by vacuum. On this phase transition boundary, as the temperature increases, the transition reaches a critical point. Here, any additional energy boils away the protons and neutrons from the cohesive nuclear droplets. The resulting phase of dispersed hadrons is similar to the pion gas, though there is some dissimilarity in the composition. While the pion gas at $\mu_B = 0$ has equal parts matter and antimatter, at greater μ_B, baryon matter exists without complementary antimatter.

Continuing along the horizontal axis, at low T and increasing μ_B, there exists the other end of the phase boundary between hadronic matter and quark matter. This quark matter is given the qualifier "cold", but the fundamental reason for the transition from hadronic to quark matter is the same as before. When many hadrons are squeezed together, quarks are attracted to other quarks in nearby hadrons as greatly as they are to their initial partners. This is illustrated in Fig. 1.7.

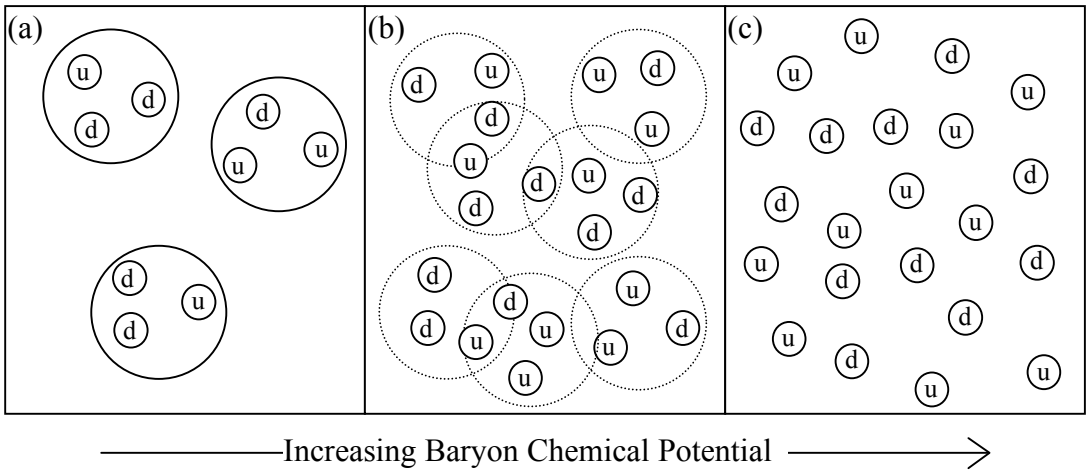

Figure 1.7: A cartoon depicting hadronic matter transitioning into quark matter as the baryon chemical potential increases at low temperature. In frame (a), quarks are bound in baryonic matter. In frame (b), as the particle density increases, it becomes less clear which quarks belong to which hadrons. Finally, in (c), a quark density has been achieved so that each quark is attracted to multiple quarks around it, rather than being bound to several partners within a baryon.

1.5: Generating and observing the QGP using heavy ion collisions

Increasing baryon density and increasing the temperature are both means of generating a quark gluon plasma, and collisions of heavy ions fulfill both of these measures. Heavy ions refer to elements with large nuclei, ionized to facilitate their acceleration. Once they are sufficiently accelerated, these nuclei are used as projectiles against either stationary or oppositely accelerated matter. The baryon density is increased by the compression when two opposing nuclei collide, and the energy of the impact heats up the particles.

The resulting hot, dense material from a high-energy collision occupies a very small amount of space, and it also disperses very quickly—an expanding *fireball* as it is

called in the research vernacular. Direct observation of the medium is impossible. Instead, experimenters search for the expanded and cooled remnants of collisions and the directly emitted, highly energetic gamma rays. These remnants carry information about the hot medium, and also about any phase change from unbound quarks to a cooler hadronic matter. The fireball is a microscopic phenomenon, but as it dissipates, the cooled particles are flung outward at nearly the speed of light, where they are observed with macroscopic detectors. The composition, momentum, and spatial distribution of these particles are all taken as evidence in the characterization of the compressed matter.

Figure 1.8 shows the many particles passing through a detector following a collision of two gold nuclei at high speed. For head-to-head collisions, thousands of particles are expelled. This is many more than the 394 protons and neutrons carried in by the two impinging gold nuclei. Clearly particles are generated in great abundance from the kinetic energy of the collision, and inspection shows that nearly equal amounts of matter and antimatter arrive at the detectors.1 This is the same behavior that was described when the QCD vacuum was heated, but is it fair to describe this microscopic system in terms of a phase diagram? If so, what temperature and density are achieved?

[1] Since matter and antimatter are generated equally, this is a way of emphasizing the dilution of the original matter by generated particles.

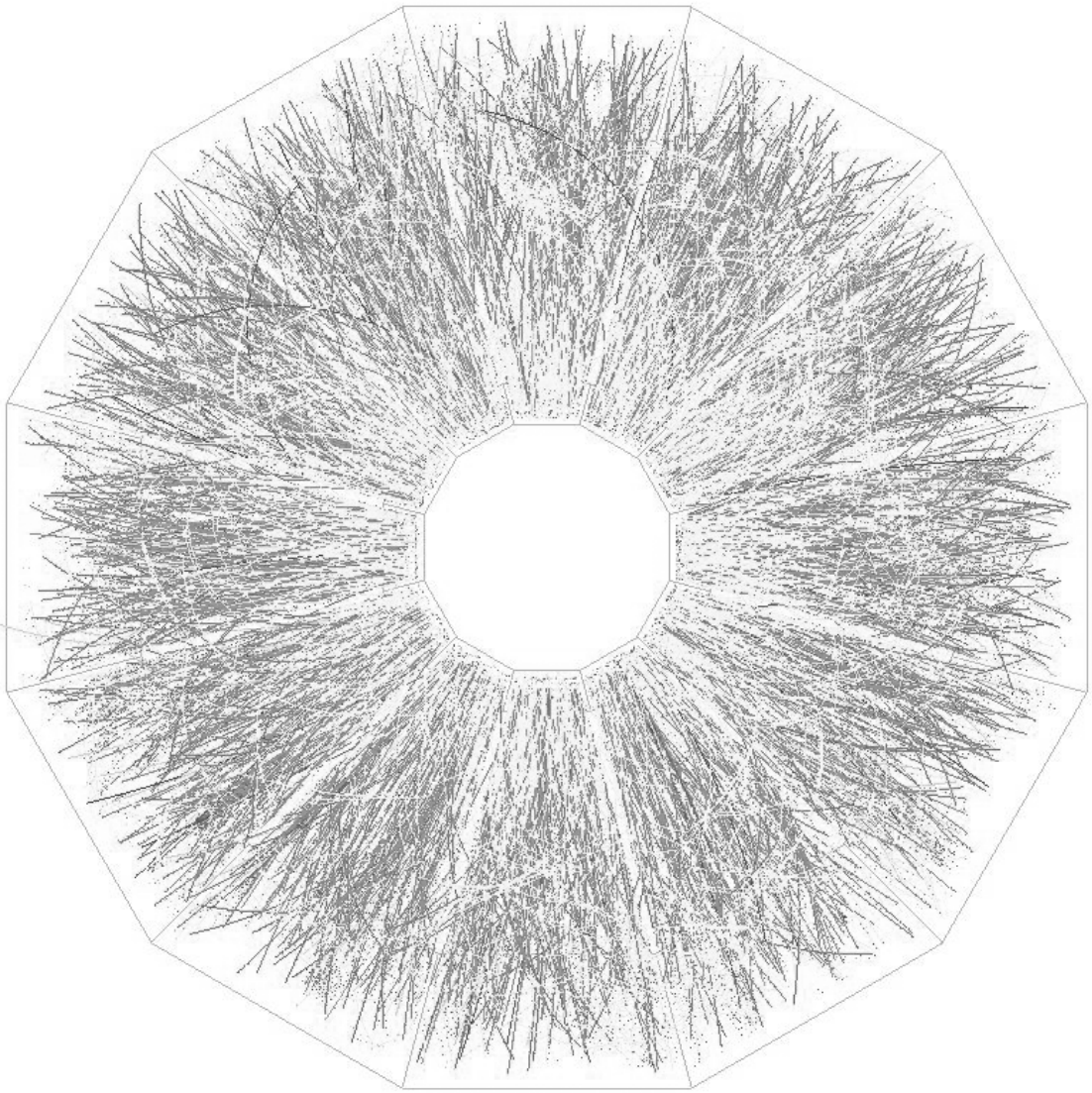

Figure 1.8: The remnants of a collision of two gold nuclei at the STAR experiment. The outline represents an end view of a cylindrical (dodecagonal) detector. Heavy ion beams pass through opposite ends of this barrel shape, colliding in the center (the middle of this figure). The paths of the particles ejected from a single collision are shown as the many curved tracks traversing the detector volume.

1.6: Evolution of a heavy ion collision

The defining aspects of a heavy ion collision are the kinetic energy and the number of protons and neutrons (collectively known as *nucleons*) in the opposing nuclei. The kinetic energy is frequently presented in terms of the energy per nucleon (E/A) rather than the kinetic energy of the whole nucleus.

Consider the collision of two gold nuclei, each traveling oppositely at 100 GeV per nucleon (roughly 99.995% the speed of light). At the writing of this thesis, this is the most energetic heavy ion system that has been created in the lab. The center-of-mass energy per nucleon is expressed by the relativistic-invariant variable $\sqrt{s_{NN}}$ (note the subscript $_{NN}$ delineating nucleon-nucleon collision energy), and, in this case, $\sqrt{s_{NN}} = 200$ GeV. The variable $\sqrt{s_{NN}}$ is used to represent the collision energy because it does not depend on the reference frame from which it is observed. For identical projectiles moving oppositely with equal energy, $\sqrt{s_{NN}}$ is just twice the per-nucleon beam energy. At this relativistic speed, a stationary observer perceives the approaching nuclei as compressed along the axis of motion. The factor of the compression is given by the relativistic variable γ, which is defined in Appendix B. At $\sqrt{s_{NN}} = 200$ GeV, γ is ~100, so the initially spherical nuclei are flattened to $1/100^{th}$ of their initial length along the axis of the collision.

At low collision speeds, two approaching nuclei may be repelled through Coulomb forces, or they may touch and reconfigure to form a large compound nucleus. At 100 GeV per nucleon, the nuclei gain a degree of mutual transparency, actually passing through one another. For an instant, the two nuclei completely overlap and the baryon density and the energy density are the greatest. However, the energy is coherent

kinetic energy rather than equilibrated thermal energy, so this is not a useful situation with regards to the goal of studying the QCD phase diagram. Although they mutually appear as dense walls of matter, the two nuclei pass through each other before the strong force is effectively transmitted. In their wake, a color field conveys the attraction of the two disintegrating nuclei. The energy of the color field relaxes through the production of matter and antimatter, or in other words, the intervening QCD vacuum melts. A cartoon of this progression is shown in Fig. 1.9.

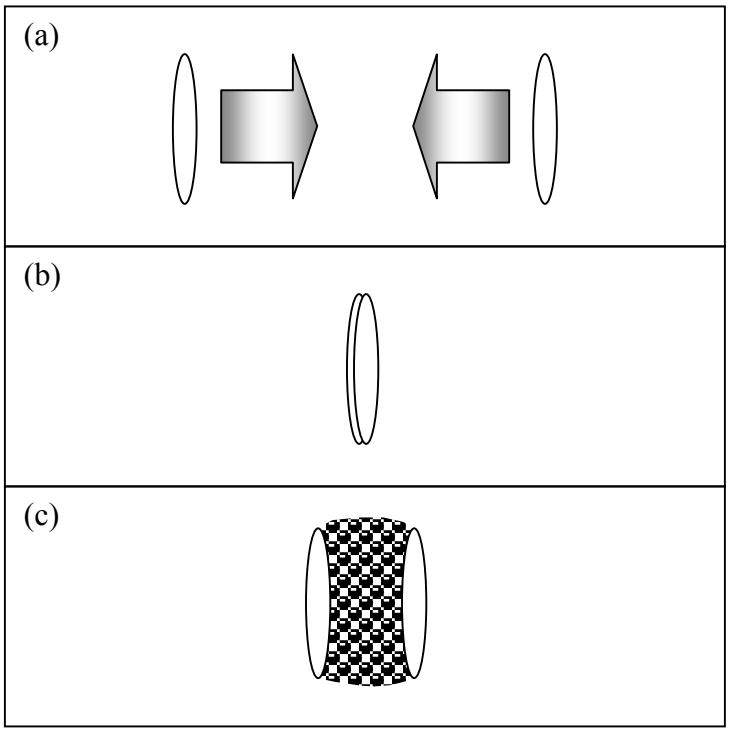

Figure 1.9: A cartoon depicting the appearance of two approaching nuclei at 100 GeV per nucleon. The nuclei have an aspect ratio roughly 1:100 due to relativistic contraction (not to scale in the illustration). In frame (a), two nuclei approach at relativistic speeds. In (b), the nuclei have collided and are overlapping in the same space, and the energy density is highest. In frame (c), the energy held in the color field that tethers the two nuclei relaxes through the production of matter and antimatter.

It is believed that, within this heated vacuum, a quark gluon plasma is formed in which quarks are free to move about, and that the mean free path is very small compared to the size of the system. As the system cools, the quark phase of matter changes to hadrons. In this epoch of the expansion, hadrons are still very energetic, and the mean free path is still much smaller than the system size. Suffering many relatively energetic collisions, these hadrons may trade constituent quarks, and it is not until the system has further expanded that the particle species become fixed. The end of this period is qualified as "chemical freezeout". For some additional time, as the system expands and cools further, hadrons continue to collide at lower energy. During this period, kinetic energy can be redistributed among the particles, until the expansion has progressed much further. The time at which the produced particles cease colliding is known as "thermal freezeout".

1.7: Evidence of thermalization in heavy ion collisions

In the study of gold-on-gold heavy ion collisions at relativistic speeds, there is considerable evidence that thermalization occurs sometime between the first moments of the collision and the later chemical freezeout. For the purpose of discussion, just two simple observations will be presented to establish this claim. First, consider that prior to their impact, the initial energy of the colliding nuclei is comprised essentially of coherent kinetic energy along the beam axis. (This is said to be the *longitudinal* direction.) However, following the collision, a large number of particles, and correspondingly a great deal of energy, is radiated in a direction orthogonal to the initial axis of approach (called *transverse* directions).

More concrete evidence of thermalization is found in the population distribution of various particle species. In Sec. 1.4 it was mentioned that the masses of the different particles should be considered analogous to energy states in a Boltzmann-like distribution. Particles of greater mass are less likely to appear than lower mass particles. The ratios of the different species and the ratios of matter over antimatter can be used in conjunction to determine both the temperature and the baryon chemical potential. From the fits of the particle ratios indicated by the dashed lines in Fig. 1.10, for $\sqrt{s_{NN}} = 200$ GeV, the temperature is 0.155 GeV and the baryon chemical potential is 0.026 GeV. Although the system has thermalized, the measured temperature reflects the system at chemical freezeout, when the identity of each particle is fixed.

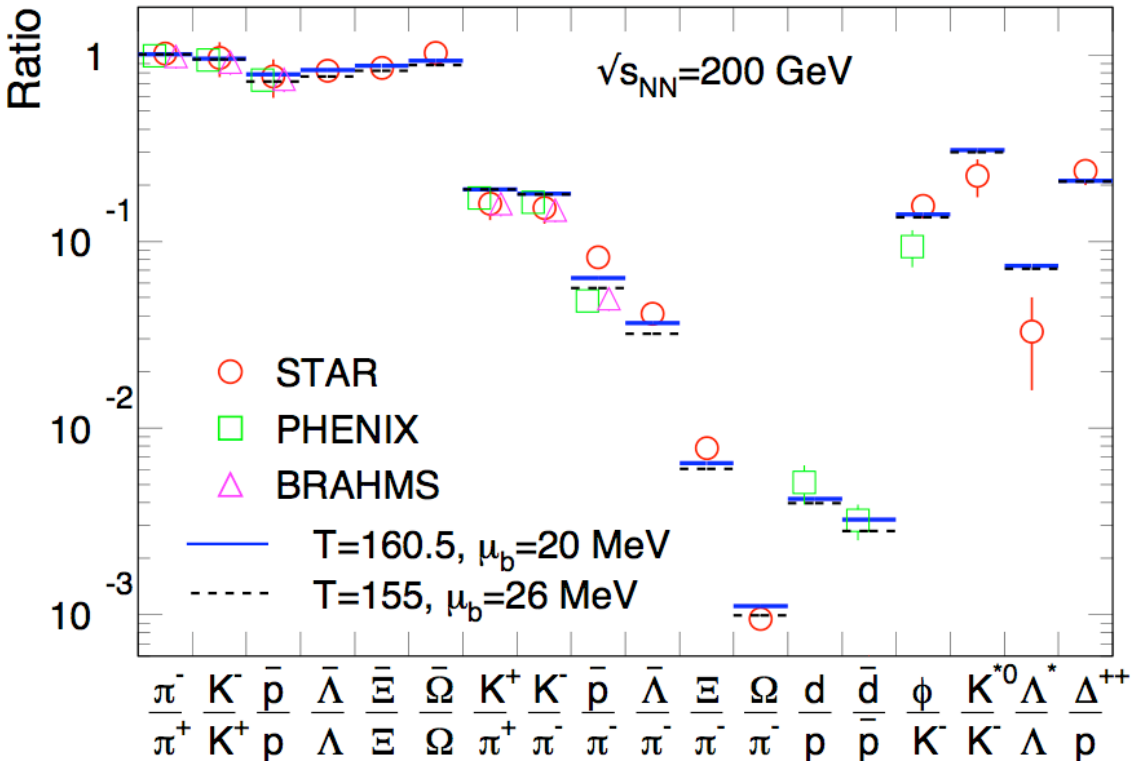

Figure 1.10: The symbols are measurements of particle ratios made by different experiments at collisions of $\sqrt{s_{NN}}$ = 200 GeV, and the solid and dashed horizontal lines show the results of a global fit to a thermal distribution [And06]. The rightmost three ratios, which involve resonance particles, were excluded from the fit. The solid line is a fit to the remaining ratios, and the dashed line additionally excludes $\bar{p}/\pi^-$ and $\bar{\phi}/K^-$.

With respect to characterizing QCD matter on a phase diagram, what is more valuable is the temperature and baryon density just as the system thermalizes, when it is densest and hottest. This is, in other words, just as the energy of the system switches from coherent, directional energy to random, thermal motion. The initial energy of the system is well defined, and the expansion rate (and therefore the volume of the system) is constrained by the speed of light. Therefore, the energy density of the system as a whole (or at least the lower limit) is easily estimated as a function of time. As it expands, the

system cools, or, in other words, the energy density decreases. The difficult problem involves determining at what point in time (or what point in the expansion) the switch from coherent to thermal energy occurs. This is the critical piece of information needed to define the maximum temperature, which in turn is needed to characterize the produced medium on the phase diagram. (Of course, this train of thought neglects the complication that a transition from coherent energy to thermal energy might be a prolonged process rather than an instantaneous switch. Nevertheless, it is a convenient abstraction to make to simplify the theoretical treatment.)

1.8: Hydrodynamic description of thermalized matter

Ideal hydrodynamics is a macroscopic treatment of a non-viscous fluid involving equations of conservation of momentum and energy and additional constraints for conserved charges. It should not be surprising that this macroscopic theory relies upon the presumption of a thermalized system—not necessarily in global equilibrium, but subject to description by a few thermodynamic variables on a local scale. Governed by Euler's equations of motion (and in this case, their relativistic generalizations), an ideal fluid reacts instantaneously to any changes in the macroscopic thermodynamic fields. In essence, the set of equations describes how macroscopic pressure gradients generate *collective flow* of the matter. The prerequisite that the system must be thermalized is quite important. In practice, it means that the timescale of local thermal equilibrium must be much, much smaller than any macroscopic dynamical behavior (*i.e.* the response to macroscopic pressure gradients).

A hydrodynamic description of nuclear collisions was first employed in 1953 by Landau, who used it as a basis for explaining the expansion of a collision system in the

direction of the beam axis (*i.e.* the longitudinal expansion) [Lan53, Fei98]. The solution to Landau's conceptual framework was worked out by Bjorken, though only as a 1-dimensional (plus time) approximation, restricted to the direction of the beam axis [Bjo83]. Therefore, the solution did not quantify the hydrodynamic expansion away from the beam axis (*i.e.* transverse expansion).

Landau's picture of hydrodynamic expansion (which interestingly includes an unrealistic assumption of the nuclei completely stopping on top of one another) has withstood the test of time remarkably well [Stei05]. However, prior to the latest (*i.e.* highest energy) regime of nuclear collisions, the expansion in the transverse directions did not *quantitatively* agree with hydrodynamic predictions. It was therefore debated whether hydrodynamics could fairly be applied to such a highly excited, few-particle system. Recent results in other branches of physics have lent themselves to the argument that hydrodynamics can indeed be extended to systems with relatively few particles (provided that the systems are in local thermal equilibrium). Two very interesting results are noted in Appendix A. In the recent high-energy regime of collisions, the observed collective flow is, for the first time, on the same scale as the hydrodynamic predictions, although not precisely in agreement [Bac05a]. There is, however, some variation in the hydrodynamic models, their input parameters, and the models that describe the preceding period of the collision [Son08]. All together, these result in a measure of uncertainty in the hydrodynamic predictions.

One example of collective behavior of particular interest is the *elliptic flow* (the subject of this thesis). This has received particular attention as evidence of hydrodynamic behavior in the early stages of the collision. Elliptic flow is a

characteristic, liquid-like expansion in the transverse direction, and it will be described in detail in Chapter 4.

How does elliptic flow help researchers study the phase diagram of nuclear matter? Primarily it acts as a chronometer, indicating at what point in the evolution of the collision the thermalization of matter occurs. It signals the point at which the easily estimated energy density can justifiably be considered in terms of temperature. As mentioned before, this is critical for tracing the path of the hot system on the phase diagram (*i.e.* indicating the maximum temperature reached).

Secondly, beyond simply indicating thermalization, elliptic flow potentially offers access to some thermodynamic properties of the medium [KH03]. To begin with, in hydrodynamics the equations of conservation of momentum, energy, and charge are not sufficient to close the system of equations. A final relationship is needed, and that is the nuclear equation of state (EoS), which generally relates the pressure P to the energy density e and the baryon charge density n_b . The speed of sound in the medium c_s (which is $\sqrt{\partial P/\partial e}$) is the variable frequently used to compare EoS's, and a "soft" EoS is one with a relatively small speed of sound compared to a "stiff" EoS. The elliptic flow is expected to be proportional to c_s^2. The transition from a hadronic gas to a QGP has been theorized to be accompanied by a softening of the EoS, so this parameter is of particular interest [Ris96a].

Chapter 2: The PHOBOS Detector at RHIC

2.1: The Relativistic Heavy Ion Collider

The research in this thesis was conducted at the Relativistic Heavy Ion Collider (RHIC), at Brookhaven National Laboratory in Long Island, New York. This collider is constructed with two counter-circulating particle beams, moving oppositely through adjacent pipes in a circular track. At a few positions along the track, the adjacent pipes merge into a single beam pipe, and the counter-circulating beams inside are directed so that they overlap in opposition. At these points, experimentalists can observe the head-to-head collisions of the particles.

RHIC is the latest fully operational machine in the evolution of increasingly energetic accelerators dedicated, in part, to the study of the QCD phase diagram. Previously, the Alternating Gradient Synchrotron (AGS) at Brookhaven, and the Super Proton Syncrhotron (SPS) at CERN (in Europe) have both used heavy ion probes for similar research [Har96]. While these lower energy accelerators generate lower temperature collisions, there is also less nuclear transparency, meaning the baryon density and baryon chemical potential are higher. RHIC probes a path that reaches very high in temperature at low baryon chemical potential. Many of the experimental techniques used at RHIC are extensions of techniques developed from observations at these lower energies. Very shortly, the Large Hadron Collider (LHC) is slated to begin operation at CERN, and eventually it will probe even higher energy nuclear collisions.

At the Brookhaven campus, RHIC is constructed at the end of a chain of previously established particle research facilities. This array of equipment allows for the generation of heavy ions and some subsequent acceleration prior to injection into the RHIC rings. The path taken by heavy ions, specifically gold ions, will be described here (though protons, deuterons, and copper ions have been accelerated at RHIC as well). The details are mainly taken from [Stes01] and [Rhic00]. Cesium sputtering is used as the ion source for Au. A heated vapor of Cs^{+} is accelerated to a gold cathode, ablating the surface. Cesium lowers the work function, increasing the quantity of negative gold ions extracted. The cathode subsequently repels the liberated Au^{-1}, and a positively charged extractor plate draws the ions onward. Thereafter, the negative ions are sent through duel Tandem Van de Graaff accelerators (which, like a tabletop Van de Graaff generator, uses a belt or chain to physically carry charge away to maintain the high potential). The negative ions are first drawn through a +14 *MV* potential. Immediately beyond this, the ions pass through a thin carbon film that strips away a number of electrons. The positive field behind these ions now repels them, and they are further accelerated toward a grounded terminal before them. At the far terminal, another carbon film strips even more electrons away. This and the ensuing removal of electrons increases the subsequent leverage that the accelerator has on the ions. Though a distribution of charge states is created after each stripping, only the most abundant charge state, +32 (at 182 MeV, or roughly 1 MeV per nucleon), is allowed to continue through the booster transfer line to the booster synchrotron. Rather than a continuous stream of ions, the ion source generates pulses, which is important for the operation of subsequent accelerators.

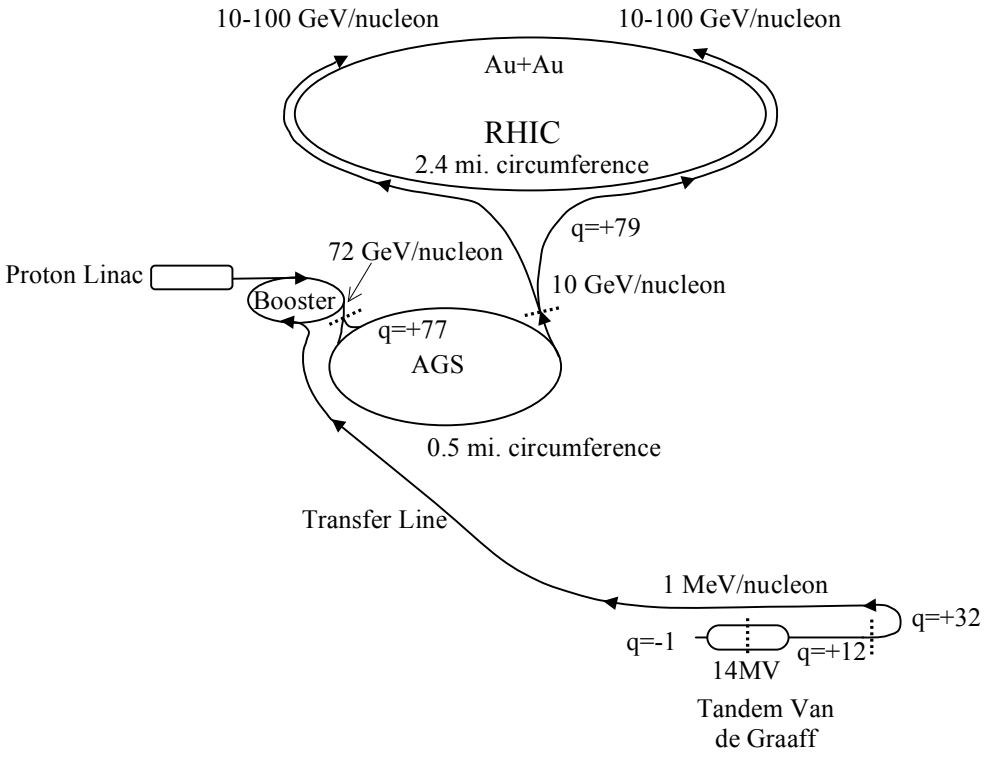

Figure 2.1: The accelerator facilities leading to RHIC [Rhic00]. Gas and foil strippers are shown as dotted lines. The selected charge states and the energy per nucleon are also noted. These are representative of the arrangement in 2001.

Figure 2.1 shows the three rings, the Booster, the AGS, and RHIC, which further accelerate heavy ions to their full energy. While the Tandam Van de Graaff is an example of electrostatic acceleration, the subsequent acceleration is done by synchrotrons, which use radio frequency (RF) waves as well as increasing magnetic fields. As a pulse of ions enters the circular synchrotron, a magnetic field is required to turn the particles inward, keeping them on a circular course. The greater the energy of the ions, the faster they go, and the greater the magnetic field strength needed to turn them within the same radius. To accelerate the ions, the beam passes through large RF cavities, which generate a momentary electrical field to give the ions a "kick" each

revolution around the ring. The radio waves have the correct frequency and are in phase such that they are at the same point in the cycle each time the ions make a full revolution. As the ions speed up, the frequency of the RF waves increase to meet this qualification. For the most part, the system is self-correcting.[1] If a particle is going faster than the intended speed, it hits the RF cavity off-time, and does not receive as forceful a push. This corrective behavior squeezes the ions together into *bunches* contained within RF *buckets*. The balancing act between RF waves and increasing magnetic field strength is handed off between the increasingly powerful and larger rings.

The largest of the facilities, the RHIC rings, use superconducting magnets so that the beams (actually discrete bunches of ions) can circulate for hours without excessive energy consumption.[2] The low temperature superconducting niobium titanium wires are bathed in liquid helium at the boiling point of 4 Kelvin. Additionally, throughout the system, the pipes that carry the ions must be kept under a vacuum. Particularly, in the RHIC rings, where beam is circulated for hours, any residual gases will degrade the beam over time. Vacuums are maintained on the order of 10^{-11} *mbar* in the cooled regions, and less than $7x10^{-10}$ *mbar* in the few uncooled regions.

The RHIC rings have six regions where the adjacent pipes holding counter-circulating beams merge into one pipe. It is in these *interaction regions* (IRs) that the collisions occur. Focusing magnets constrain beam widths to a few milimeters in diameter, and, during acceleration, the opposing beams pass by one another. Only once the beams are brought to full energy are they further steered so that they overlap. Though the bunches are constrained into very narrow beams, the angle at which they meet is so

---

[1] The exception at RHIC is the notorious point in the acceleration cycle called the *transition energy*.

[2] The refrigeration system alone requires around 15 *MW*, so the energy savings are relative. The collider is shut down during the summer since electricity demands of the Long Island populace increase at that time.

shallow that they overlap for many centimeters before diverging again. The volume in which the beams overlap, and therefore the volume in which the collisions occur, is called the *interaction diamond*. Once the beams are steered into one another, the bunches of ions most frequently pass through one another without incurring a collision. The 56 bunches generally occupying each ring revolve at roughly 80,000 cycles per second. Even while there may be thousands of collisions per second, each bunch holds perhaps 10^{10} heavy ions, and, therefore, the loss of ions from the beam due to these collisions is a negligible fraction of the whole ensemble of ions. The rings continue to circulate for hours before other considerations, such as diverging orbits, lead to instability.

The RHIC rings have six interaction points, and four of these interaction points have been occupied by heavy ion experiments. STAR and PHENIX are two large detectors, each several stories high, while PHOBOS and BRAHMS are smaller arrangements of detectors and magnets. The PHOBOS detector operated beginning in an engineering run in 1999, and continued through 2005, and it is at this experiment where the research for this thesis was conducted.

2.2: The PHOBOS detector

The PHOBOS detector is comprised of many different sub-detectors arranged around a nominal interaction point. The actual interaction diamond where collisions occur generally reaches some tens of centimeters to either side of this point along the beam axis. Surrounding the interaction point and extending 6 m in either direction along the beam axis is a beryllium beam pipe, about 8 cm in diameter and with walls of a thickness of only 1 mm. Both the thickness and the choice of material reflect the need for transparency to outgoing particles while still maintaining the mechanical rigidity and

impermeability needed to hold a vacuum. The length of the beam pipe allows even particles with very small deflection from the beam direction to pass through, though a shallow angle of incidence upon the beam pipe necessitates passing through a greater amount of material. (A cartoon illustrating this idea is provided in Fig. 2.2.) Beryllium is chosen because it has a very small interaction cross-section with hadrons. Putting as little absorbing material as possible between the collision and the detector was a guiding design consideration in PHOBOS, and the sensitive nearby detectors are meant to observe particles even with very low momentum.

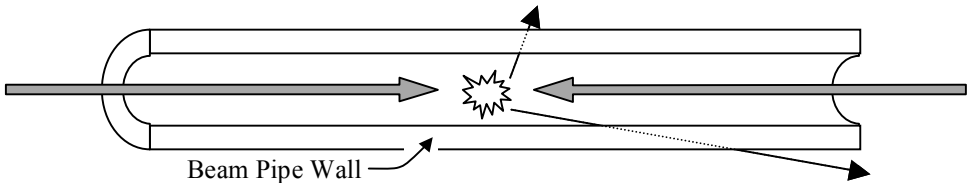

Figure 2.2: A cut-away cartoon of the beam pipe. Particles exiting with only slight deflection from the beam direction pass through more material.

A schematic overview of several detectors and structures near to the interaction point is shown in Fig. 2.3. A few additional detectors are too peripheral to show at this scale. This figure is representative of the detector configuration during the 2003 run.

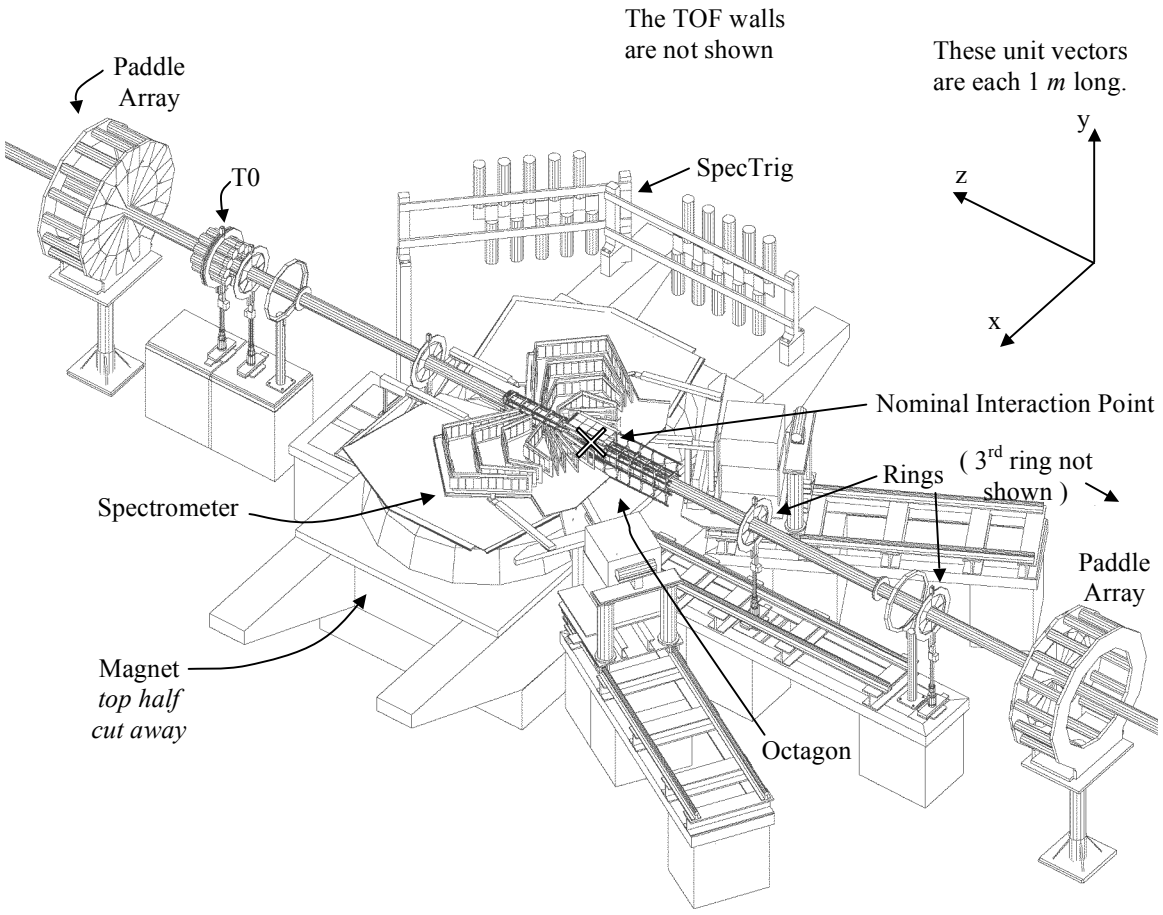

Figure 2.3: A schematic overview of the PHOBOS detector showing some of the sub-detectors near the interaction point.

In the upper right-hand corner of Fig. 2.3, the orientation of the *laboratory coordinate system* is shown. By convention, the *z* axis is oriented along the beam line, though the choice of the positive and negative direction was made arbitrarily. The y axis points towards the ceiling, and the x axis is chosen to form a right-handed coordinate system. The origin of the laboratory coordinate system is chosen to be the nominal interaction point, though, in reality, collisions are distributed as dictated by the collision diamond.

Sometimes it is useful to use a polar coordinate system. Normally, the azimuthal coordinate (in the *xy* plane) is ϕ, and the polar coordinate (in the *z* direction, or along the beam axis) is θ. However, routinely, very small angles of deflection away from the beam axis are important, and so an alternative coordinate is useful for dealing with these small values. This alternative variable is called the *pseudorapidity*

$$\eta = -\ln\left[\tan\left(\frac{\theta}{2}\right)\right] \quad . \tag{2.1}$$

Here, θ is the angle measured with respect to the beam axis. Figure 2.4 shows θ and η for a few angles for illustration.

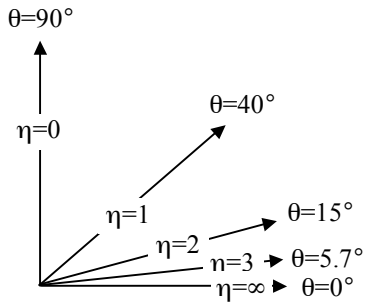

Figure 2.4: Several angles to illustrate the transformation from θ to η.

Shallow angles relative to the beam axis are said to be at *forward rapidity*. *Midrapidity* describes angles perpendicular to the beam axis, particularly those from $-1<\eta<1$. Pseudorapidity is more than just a convenient transformation of the polar coordinate. It is also related to the relativistic-invariant variable for speed, the *rapidity y*, which is discussed in Appendix B.

The pseudorapidity ranges for a few of the key detectors in this analysis are shown in Fig. 2.5.

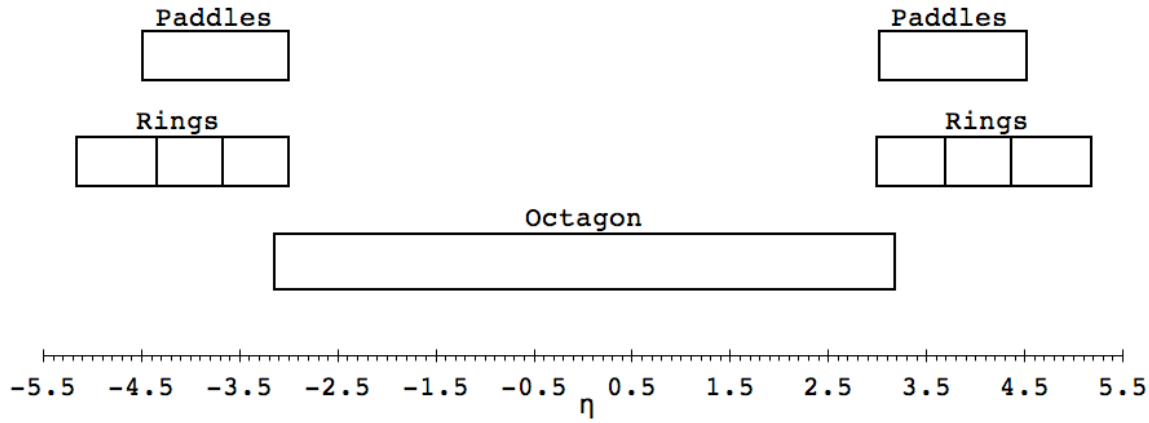

Figure 2.5: The pseudorapidity range subtended by the octagon, the sets of rings, and the paddle counter arrays as viewed from the nominal interaction point.

A variety of different detector types are used at PHOBOS, and these are generally designed to be sensitive to the many hadrons emanated from a collision. The detectors each have some material with which the particles interact. The deposited energy is ultimately turned into an electrical signal that can be digitized and recorded. Most of the detectors at PHOBOS are relatively transparent and sensitive only to charged particles. Fast moving hadrons pass through these depositing only a small amount of their energy in their wake. While slow particles interact with the detector material for an extended time and therefore deposit greater energy, fast particles deposit nearly a fixed amount of

energy per distance traveled once they have surpassed a threshold speed. Therefore, particles passing through such detectors are commonly detected as minimum ionizing particles (MIPs). Additionally, a few detectors called calorimeters are designed to stop particles by placing dense materials in their path. Through multiple scattering interactions, a particle ideally looses all of its energy to the calorimeter detector. These are sensitive to both charged and uncharged particles.

The majority of the data from PHOBOS comes by way of silicon semiconductor detectors. In these detectors, a PN junction is reverse biased to form a depletion zone. Charged particles passing through the silicon create electron-hole pairs, and the number of electrons elevated into the conduction band is proportional to the energy deposited. Very little energy is required to generate an electron-hole pair, so the statistically driven energy resolution is very good. Numerous embedded anodes and cathodes, respectively, collect the electrons and the holes before they can recombine. The density of electrical contacts that can be squeezed onto a single silicon wafer leads to very good spatial resolution. These individual silicon detector elements are called *pixels*, and there are several hundred thousand of them among all of the sub-detectors of PHOBOS. The silicon detectors are placed around the interaction region in order to observe very precisely where particles have passed and how much energy they have deposited.

The remaining detectors at PHOBOS use either scintillators or Cerenkov radiators to detect particles. Scintillators are frequently prepared as translucent plastics doped with organic fluorophores. Charged particles passing through such materials excite the fluorophores, and an affixed photomultiplier tube (PMT) measures an amount of light, which is proportional to the energy deposited. Such detectors are quite fast and have

good time resolution. In a similar detector setup, when a particle exceeds the speed of light in a medium, Cerenkov radiation is emanated. This faint light can also be detected using PMTs.

The dominant physical feature of the PHOBOS detector is the double dipole magnet at its center (shown alone in Fig. 2.6). The purpose of the magnet is to differentially bend, and therefore distinguish, particles based on their momentum.[1] In Fig. 2.6, the four pillars at the corners support a sandwich-like steel frame. Affixed near the center are adjacent poles that form the lobes of the figure-eight shaped magnetic field. The field lines run vertically between opposite poles. In one lobe they are oriented upward, while in the other lobe they are oriented downward. The magnet is reversible, which means that the fields can change directions, but the lobes always point oppositely. This is a non-superconducting magnet, and when fully energized at 3600 A and 115 V DC, it consumes 342 kW and produces a field around 2 T near the center. Interestingly, the huge steel supports are actually drawn together by several millimeters when the magnet is energized.

[1] Chemists are generally familiar with magnetic sector mass spectrometers, which separate ions by their mass to charge ratio. This is possible because the acceleration of the ion prior to entering the magnetic field is well defined. In fact, charge and momentum are the two factors that dictate magnetic deflection. In this experiment, the detected particles have ±1 charge, so the amount of curvature communicates the momentum.

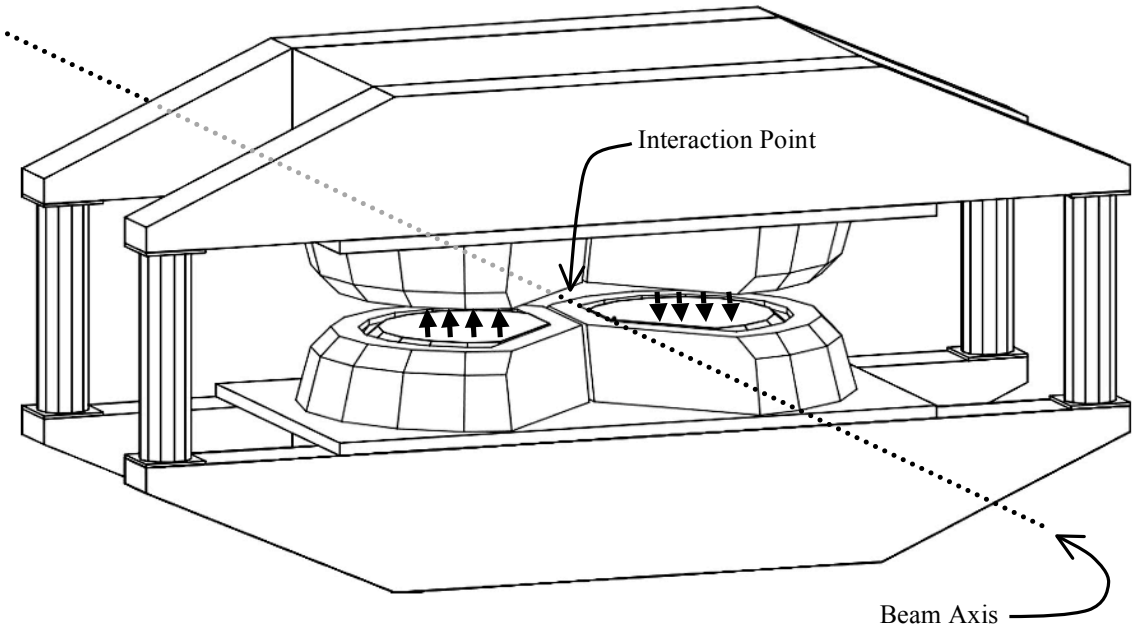

Figure 2.6: A structural diagram of the PHOBOS magnet. The arrows sandwiched within the magnet illustrate that the two lobes have oppositely oriented fields (though the polarity of the pair may be in the reverse configuration as well).

Returning to Fig. 2.3, below the nominal interaction point (near the center of the drawing) is the structure of the bottom half of the magnet. The curved yolk of one of the dipoles is visible just below an aluminum plate, which is used to support several detector elements. These detectors are sandwiched within the magnet, with some parts inside the field and others beyond it. The upper half of the magnet has been removed from this drawing so that the detectors can be seen.

Figure 2.7 shows a zoomed in view of the detectors in and around the magnet and also their support structures. Flanking either side of the beam pipe in the horizontal plane are two spectrometer arms. These detectors are comprised of a number of planes of silicon arranged in a concave pattern around the interaction point. Particles traversing the spectrometer deposit energy, referred to as *hits*, into each plane. The trajectories of the particles, called *tracks*, can be reconstructed from the hits in the spectrometer. In the absence of a magnetic field, the tracks point in a straight line back to their origin, called the *particle vertex*. Generally the particles point back to the *collision vertex*, but they may also point back to a *decay vertex*, or to the point where they scattered off of some surrounding material. Particles originating at the collision vertex are designated as *primary* particles, and scattered particles are called *secondaries*. In this thesis, the word "vertex" by itself refers to the collision vertex.

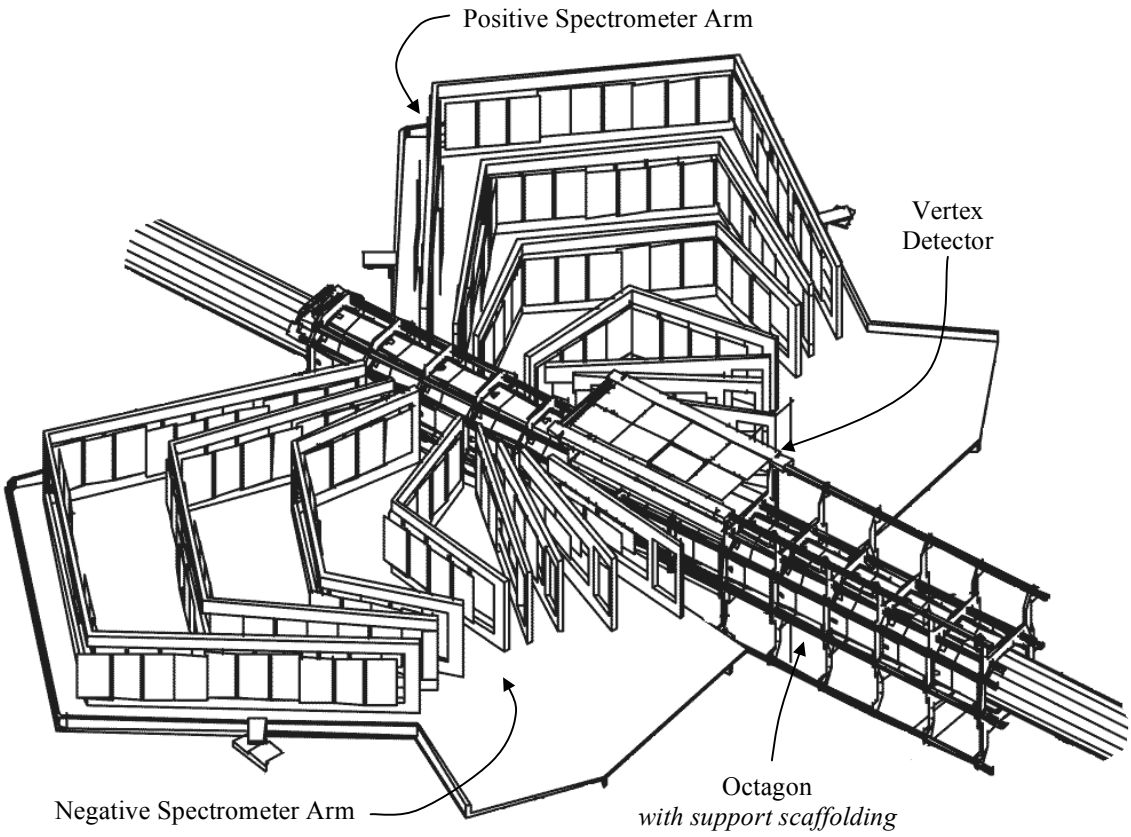

Figure 2.7: The spectrometer arms, the vertex detector, and the octagon.

In the presence of a magnetic field, useful information can be determined from the trajectory of a charged particle. By itself, the curvature can be used to find the momentum. In conjunction with dE/dx (the energy deposition per length of detector material), the identity of the particle (PID) can potentially be determined as well. To facilitate track finding, the first few planes of the spectrometer (those closest to the IR) reside in a field free region, while the peripheral planes are within a broadly-uniform field. Figure 2.8 illustrates the positioning of the spectrometer arms within the magnetic field, and it also provides an example of tracks passing through the spectrometer planes. See Appendix J for a further example of tracks in the spectrometer.

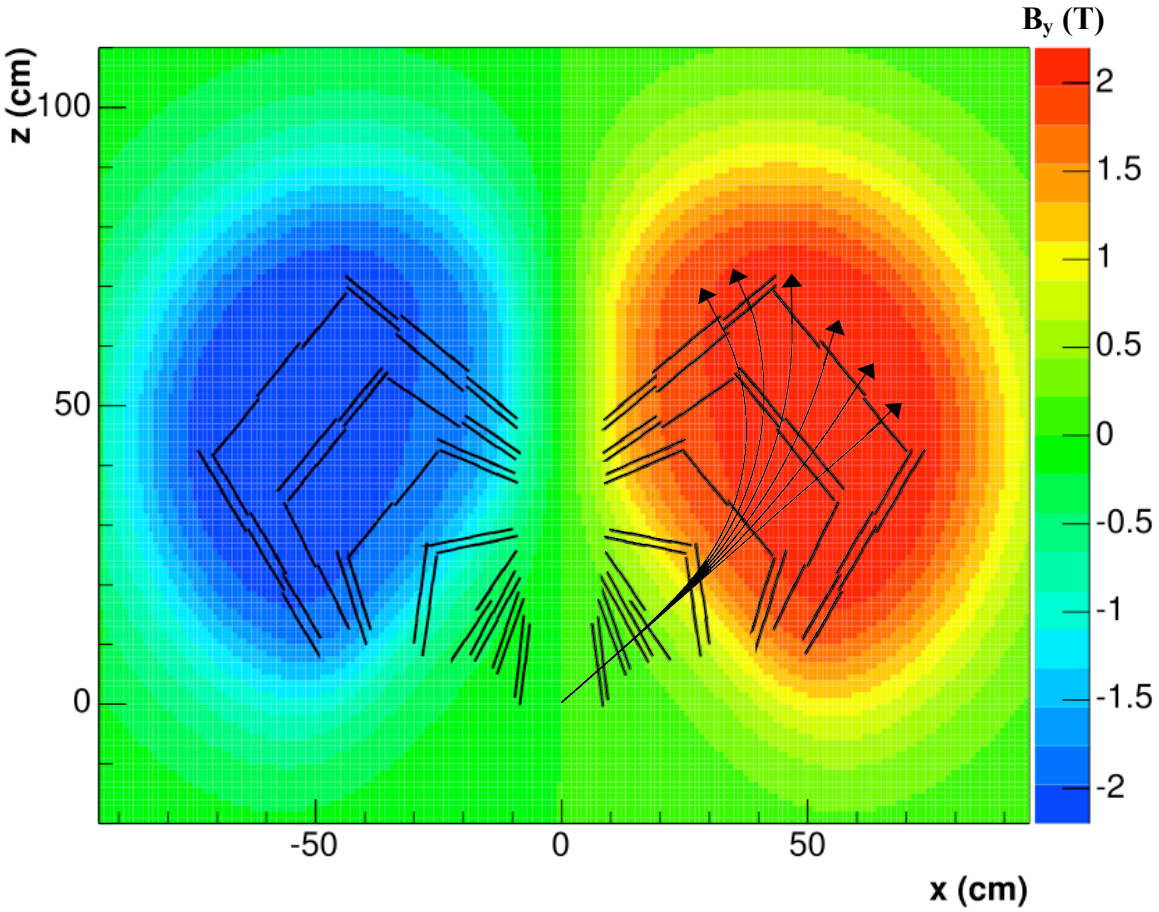

Figure 2.8: The top-down view of the two spectrometer arms overlaid with the magnetic field strength. The curves originating at (0,0) and extending through the positive spectrometer arm are the tracks of six simulated pions with momentum of $p=\infty$ (straight), 1.0, 0.5, 0.33, 0.25, and 0.20 GeV/c (most curved) [Gul04]. These illustrate that there is virtually no bending in the field free region where the six innermost spectrometer planes reside.

While the spectrometer tracks particles in order to determine their characteristics, it is limited in its angular acceptance in azimuth. (Here, "acceptance" means the angular region subtended by the detector, and it is frequently qualified as the *geometrical* acceptance. In detectors such as the spectrometer, in which momentum determines the amount of bending, acceptance is depicted in phase space.)

The vertex detectors are finely segmented silicon detectors above and below the interaction region. The uppermost plane is visible in Fig. 2.7. Another plane lies just beneath it (yet above the beam pipe), and a mirror image pair of detectors are placed below the beam pipe. These can be seen all together in Fig. 2.9. The vertex detectors all reside in a field free region, so the many straight-moving particles passing through either the top or bottom pair can be used to determine the location of a collision along the *z* axis (beam direction).

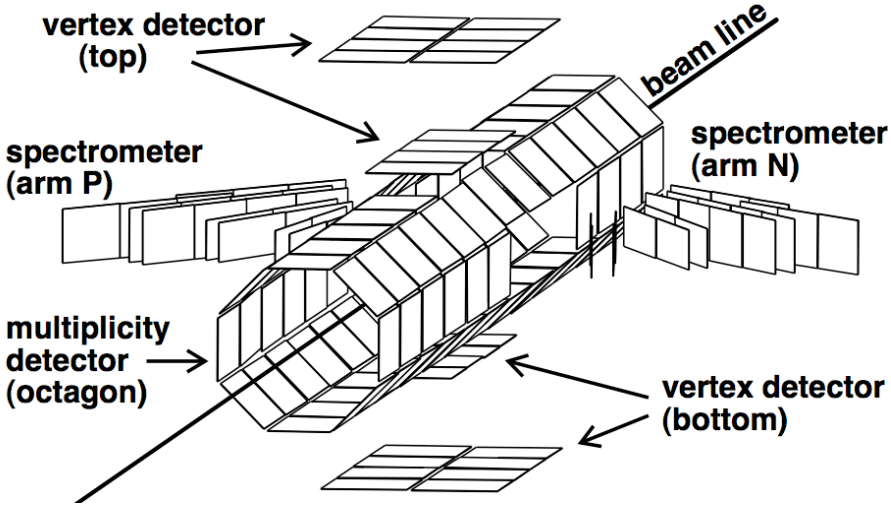

Figure 2.9: Active detector regions of the octagon, the four levels of the vertex detector array, and the first eight planes of either arm of the spectrometer [Woz06].

The remaining silicon sub-detectors are the octagon and the rings. These are multiplicity detectors, which means that they only gather information on the number and positions of particles passing through. They are unable to reconstruct the particle trajectories, momentum, *etc.* The octagon detector, visible in Fig. 2.7, is an octagonal barrel that surrounds the beam pipe with just a few centimeters of intervening space. It is 1.2 m long, centered at the nominal interaction point. There are holes in the horizontal faces and in the vertical faces that expose the vertex detectors and inner spectrometer layers. The octagon provides good angular coverage, however many particles traveling near to the beam direction still pass through the open ends. Particles with minor deflection from the beam axis are instead observed by the several arrays of ring counters, which can be seen in Fig. 2.3. These roughly circular arrays are spaced several meters apart, so that from the interaction point they each appear to fill a different annulus beyond where the octagon coverage ends. In concert, these many silicon sub-detectors are able to count particles emerging in almost any direction. Together they cover a pseudorapidity range from $-5.4 \leq \eta \leq +5.4$, as shown in Fig. 2.5. Many more details about the construction and performance of the silicon sub-detectors are available in [Bac03].

In either direction surrounding the beam axis, a little over 3 m away from the interaction point, are two inward facing arrays of scintillator detectors called paddle counters. Unlike the finely segmented silicon detectors, each of the 16 paddle counters that constitute an array has a roughly 100-cm^2 face. This slab of scintillator is connected through a light guide to a PMT to form a single paddle. Several tens of particles may hit a paddle, but the response from each PMT is linear. The paddles have a dynamic range

from 1 to up to 50 particles. More information on the paddle counters is provided in [Bin01].

Originating at the collision vertex, primary particles travel close to the beam axis to reach the paddle counters. These are fast moving particles, still retaining some of the initial momentum of the beam. Because they are moving very nearly along the beam axis, any given particle will strike a paddle counter with an angle of incidence nearly normal to the face of the scintillator. Since they are high-energy and they follow the same short, direct path through the scintilator, these particles nearly all deposit the same amount of energy (*i.e.* there is little deviation in the 1 MIP signal). Therefore, the total energy deposited in the paddle arrays can be quickly and simply related to the number of particles passing through them.

In addition to counting the number of particles, the two arrays can be used in conjunction to roughly determine the collision vertex along the z axis. This is accomplished by comparing the arrival times of the opposite waves of particles striking the two arrays. The technique is based on the assumption that the particles are traveling at essentially the speed of light. If the signals arrive at the same time, then the collision has occurred directly between the arrays, and the particles have taken the same amount of time to reach each array. If the signal from one array precedes the other by, for example, 6 ns, then the collision is 0.9 m nearer to that array and 0.9 m farther from the other (since the speed of light is roughly 0.3 m/ns). The resolution of this method is at its best limited in accuracy to around 0.5 m because of natural variations in the response times of the paddle arrays. However, it is sufficient to identify whether a collision occurs near the nominal interaction point or whether it is too far away to be of interest.

Since they can quickly and simply detect the number of particles in a certain pseudorapidity range and also the approximate collision vertex position, the paddle arrays serve as the primary trigger for the PHOBOS experiment. The signals from the paddles are quickly fed through fast logic electronics, and, if the conditions indicate that a collision has occurred, the signals from the remaining detectors are read out. The silicon detectors have on-board buffers that collect and retain a brief memory of the recently deposited charge. While this buffering is continuous, the readout of the information takes a moment (since it involves the analog-to-digital conversion and subsequent transmission of hundreds of thousands of data channels). Rather than attempt to continually read them out, the silicon detectors are only queried for their recent history when something interesting happens. In this respect, the trigger is the shutter button to the experiment, recognizing the occurrence of a collision and setting the moment when the changing image on the silicon detectors will be captured.

The impact of two particles is called a *collision*. When a collision is detected, the trigger causes the readout of the rest of the PHOBOS detectors. The data from all of the detectors all together is called an *event*. (In other words, an event is a picture of a collision.)

A little outside of the boundaries of Fig. 2.3 in the negative x direction are two time-of-flight (TOF) walls. The spectrometer uses bending direction to determine momentum and additional dE/dx information to determine the particle species. This becomes less distinguishing with high momentum particles, where the energy deposited becomes increasingly similar. The TOF walls are used to extend the particle identification to higher momentum. Bending in the spectrometer still establishes the

momentum, and the time of flight determines the velocity. The resulting mass term distinguishes among the possible particle species. The two TOF walls are each constructed of 120 scintillator slats, 0.8-cm^2 by 20-cm high. These slats have PMTs affixed to either end to accurately determine the arrival time of a particle irrespective of its position on the slat.

In order to determine the elapsed flight time, the TOF system needs to know when to start its timer, as well as the time of arrival of each particle. This zero time is measured by the T0 detectors. Arranged in two inward facing arrays surrounding the beam pipe, these detectors operate similarly to the paddle detectors. While the cerenkov radiators used in the T0 detector are smaller than the scintillators in the paddles, both detectors arrays are sensitive to the timing of the initial wave of particles generated from a collision. The T0 PMTs have a very well defined transit time, and slower tubes are additionally moved nearer to the interaction region to increase the uniformity of their timing.

The zero degree calorimeters (ZDCs) are not shown within the scale of Fig. 2.3 because they are positioned on either side of the interaction region at distances of over 18 m along the *z* axis. This is just beyond the point at which the two oppositely circulating beams, previously occupying a single tube, diverge into two separate paths. The magnetic field that accomplishes this deflection is the precise strength to bend the paths of the heavy ion beams. Any lighter charged particles (protons for example) are deflected out of the beam pipe to sharper angles, and neutral particles traveling in the direction of the beam do not turn at all. The ZDCs are positioned within this split, such that neutral particles pass into them. Many plates of tungsten act as a dense wall into

which neutral particles enter. The resulting scattering slows down the neutral particles, and generates showers of secondary particles, including many charged particles. These illuminate scintillating fibers sandwiched between the tungsten plates, which lead to photomultiplier tubes [Adl01].

The data acquisition system (DAQ) was ultimately responsible for reading the output of every channel of every detector. Over 135,000 silicon channels (each with energy digitized as a 16 bit word) and 2,000 additional scintillators (each containing several bytes of energy and timing information) were read at a peak rate of 575 Hz. Fiber optic cables (120 MB/s) carried information encoded at the silicon detectors to an array of 24 PowerPC processors where the data underwent lossless compression (with a potential for 200 MB/s). At this stage, the data was "zero-suppressed" to remove empty pixels from the data stream. The data was ultimately saved on magnetic tape at the High Performance Storage System (HPSS) at the RHIC Computing Facility (RCF) via a single Gigabit fiber optic cable, but the transfer rate to this facility was only 50 MB/s over prolonged periods. A 3.2 TB storage system was installed as a buffer, and it allowed for recording (50 MB/s) and simultaneous read-out to HPSS (50 MB/s sustained). This provided breathing room during HPSS downtime and prolonged data taking.

2.3: Basic data manipulation

A great deal of work has gone into understanding the response of the various detectors. In every instance, the data that is directly read out from the detector undergoes some manipulation before it can be used in a physics analysis.

Briefly, the manipulations of the silicon signals are as follows. First, the analog-to-digital converters (which collect and digitize a charge) have a quasi-static offset

known as the pedestal. This is the current collected from a pixel when there is no signal. The silicon channels were read out periodically between collisions to establish the pedestal value, which in turn was subtracted from the signal. A second type of charge offset called the common mode noise (CMN) was variable with each readout. Since it was shared among all of the elements in the same detector region, it could also be isolated and eliminated. Using the MIP peak from real data, the differing degree of preamplification and signal shaping done onboard each silicon chip was measured. Calibration factors were used to relate the digitized signal with respect to the energy deposited. After all of this, each *hit* provided both the pixel position and the energy deposited by the particle. In those situations where a single particle was likely to traverse more than one detector element, the energy deposited in adjacent silicon pixels was combined in a process called *hit merging*.

The manipulation of the PMT-based detectors varied according to their functions. In every case, a pedestal subtraction was required. Sometimes adjustments were made in the hardware to normalize detector response, and other times corrections were applied to the data. In some cases, the high voltage was adjusted so that several adjacent PMTs produced the same energy output for minimum ionizing particles. Similarly, in some timing applications, those PMTs that were slower than their peers were moved centimeters closer to the interaction region in order to normalize the time response. In those cases where there was no hardware correction, a correction would be applied directly to the data. (Even with hardware corrections, data corrections were used as a refinement.)

While many years of collaborative effort (including my own) went into refining the detector response at PHOBOS, by the time the detector was decommissioned, these corrections were a common starting point for all physics analyses. Many of these basic manipulations are described in [Bac03]. This thesis will therefore (perhaps unjustly) avoid a proper description of this subject, and instead focus on the steps of the analysis that diverged from the common treatment of data.

2.4: Hit merging in the octagon detector

The pixels in the octagon are very broad in azimuth (only 32 pixels in 2π radians), but the segmentation along the longitudinal axis is much finer (3 mm per pixel). Owing to the geometry of the octagon, particles emitted from a vertex near the mid-span and having a small deflection from the beam will pass through the peripheral regions of the detector at an angle. This is illustrated in Fig. 2.10. This has two immediate consequences. First, an oblique particle will pass through more material than a particle traversing normal to the face of the detector. Therefore, for the same dE/dx, this means that more energy will be deposited. Secondly, beyond a certain angle of incidence, it becomes probable that the particle will pass through multiple adjacent pixels, and it is necessary to combine nearby hits to find the full energy deposited. After that, the energy needs to be normalized based on the angle. Both procedures require the collision vertex, and the energy normalization requires an exact knowledge of the position of all elements of the detector. Interestingly, instead of using a known collision vertex to determine the number of pixels that should be merged, the distribution across multiple pixels can be used to triangulate back to the vertex position.

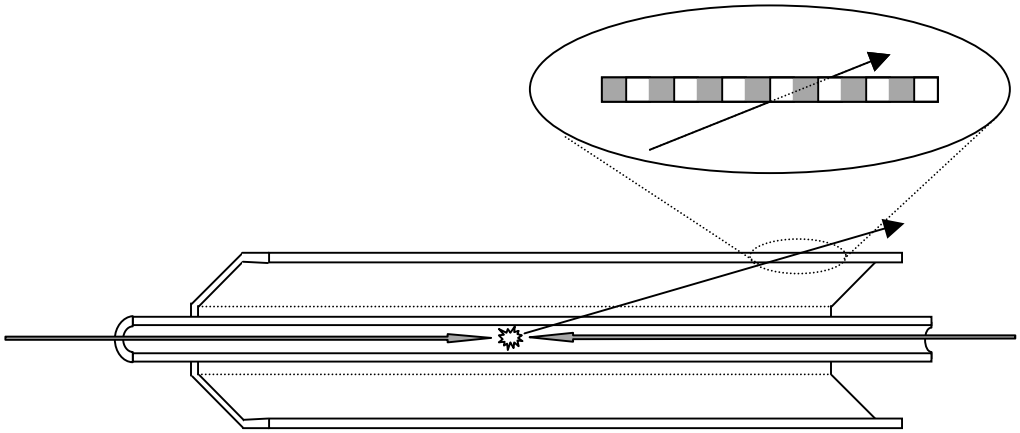

Figure 2.10: A cartoon depicting a cutaway of the beam pipe and surrounding octagon detector. The elliptical region is a magnification of a particle passing through a wall of the octagon. Because it enters at an angle, the particle will pass through more material than if it entered normal to the surface. Also, this illustrates how a particle might traverse more than one pixel (alternately shaded gray and white) along the *z* direction.

2.5: Tracking

Tracks are the reconstructed trajectories of particles passing through the spectrometer, and *tracking* is the process of finding tracks based on the hits within the sequential spectrometer layers. In the PHOBOS spectrometer, tracks are made up of two distinct portions. *Straight tracks* are the trajectories of particles within the six innermost layers of the spectrometer. These layers reside between the two lobes of the magnet, in the so-called "field-free" region (see Fig. 2.9). Particles energetic enough to pass through the first 6 layers of the spectrometer are high enough momentum that their curvature in the "field-free" region is negligible. The subsequent layers of the spectrometer reside within the magnetic field to varying extents. Since the particles have electric charge of ±1, the second portion of the tracks is a curved region, with the degree of curvature indicating the momentum. *Curved tracks* are completely reconstructed tracks (*i.e.* the

union of the straight track with its adjoining curved region.) The tracking algorithm is discussed in detail in [Bac07].

Tracks are described by two important variables. The *distance of closest approach* (DCA) is the difference between the reconstructed particle vertex and the best estimate of the collision vertex. If the DCA is too large, it suggests that the particle is a decay product or a secondary. The second variable is the *track probability*, and this is a goodness-of-fit parameter that comes from the tracking algorithm. Sometimes, random hits align to produce "ghost" tracks, and these are generally distinguishable from real tracks by their very low track probability (<0.05).

2.6: Vertexing

Vertexing refers to finding the collision vertex on an event-by-event basis. The vertex positions in the *x* and *y* directions are tightly bunched from event to event, and the average position in the *xy* plane as a function of time is defined by the *beam orbit*. The final coordinate, the *z* position, is the most difficult coordinate to determine because it changes from event to event.

There are two PHOBOS-standard vertexing algorithms used in this analysis. The first, RMSSelVertex, is actually a conglomerate of vertexing algorithms using various detectors, and it is most useful in an environment where there are many particles and many hits in the detectors. The following are some of the methods that RMSSelVertex employs:

1. The combinations of hits in the vertex detectors can be used to point back to a common origin in the *z* and *y* directions. A schematic showing the principle of this technique is shown in Fig. 2.11.

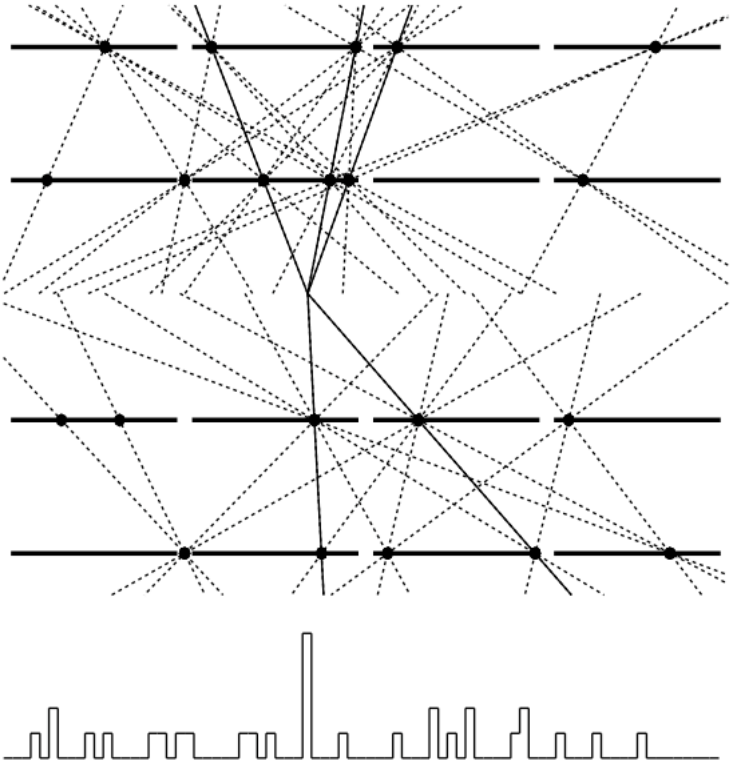

Figure 2.11: A cartoon illustrating the principle of vertex finding along the *z* axis using the vertex detectors. A profile in the *yz* plane shows the hits (circles) in the silicon pads of the vertex detectors (horizontal bars). The dashed lines are all of the possible linear combinations projected back to the beam orbit. The frequency of intersections along the *z* axis is shown as a histogram at the bottom. The linear combinations originating from the most probable vertex position are presented as solid lines [Woz06].

2. Likewise, the straight tracks in the spectrometer can be used to point back to the collision vertex.
3. The profile of hits in the octagon along the *z* axis (*i.e.* the hit density) may be fit with a Gaussian curve. Then the mean can be taken as the collision vertex position in the *z* direction. This algorithm is named OctMultProb.

In addition, the paddle vertex, though it has a poor spatial resolution, can be used to verify that the other methods have not failed catastrophically.

The second standard vertexing procedure is designed for situations in which there are few particles and, correspondingly, few hits in the silicon detectors. The procedure uses two algorithms: OctMultProb and OneTrackVertex. OneTrackVertex does a combinatorial analysis on the hits in the vertex detectors and the first planes of the spectrometer. Those combinations that produce straight lines that do not intersect with the known beam orbit are rejected. The vertex pointed to by the greatest density of the remaining lines is taken as the final position in the *z* direction. More information about the PHOBOS vertex algorithms is available in [Gar07], [Woz06], and [Hol05].

Chapter 3: Relating the Initial Geometry to Experimental Observables

3.1: The collision evolution from fireball to freezeout

Figure 3.1 is a qualitative illustration of the evolution of the collision showing four possible phases of matter. This sort of diagram is known as a *light cone*, and it illustrates the spatial-temporal progression of the fireball as it cools.

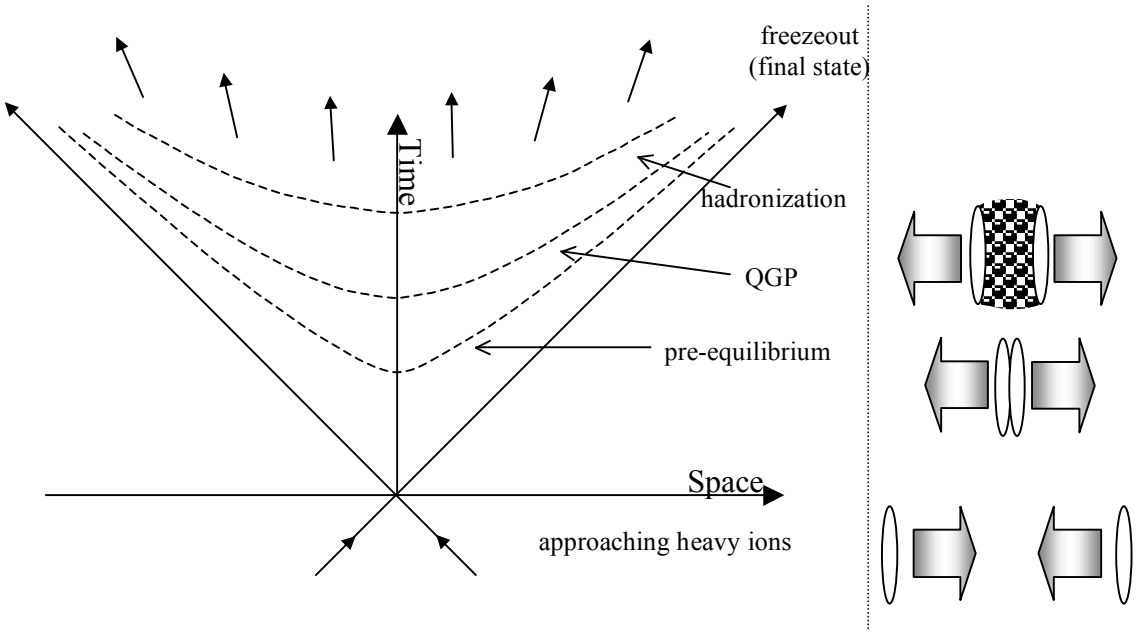

Figure 3.1: A light cone diagram of the evolution of a heavy ion collision. The diagonal lines have the slope of 1 second per light-second, which is the maximum rate of expansion of the system. To the right are several cartoons illustrating the progression of the system from the approaching ions, to pre-equilibrium, to a QGP or hadronic phase. Adapted from [McL03].

The collision occurs at the origin of Fig. 3.1, where the diagonal lines intersect. Scientists studying the nuclear phase diagram are generally interested in the quark gluon plasma phase, though the progression through the other phases cannot be wholly neglected. For example, understanding the pre-equilibrium system helps to shed light on

the initial conditions of the QGP phase. Following the QGP phase, the hot matter undergoes at least two more phase transitions before arriving at the detector as free-streaming (*i.e.* no longer interacting) particles. Like the transition preceding the QGP, it is helpful to understand the later phase transitions in order to deconvolute the *final-state interactions* from the characteristic signatures of the plasma itself. Ultimately, what began as a microscopic system is studied using the final distribution of particles on a macroscopic scale (for example, those particles seen by the STAR detector in Fig. 1.8).

In essence, the overarching task for the RHIC experiments is to make connections between the particles reaching the detector and the conditions earlier in the collision. The next section introduces the vocabulary used to describe the collisions. Section 3.3 introduces a model used to characterize the initial state and to relate initial conditions to the final-state observables.

3.2: The geometry of a heavy ion collision

There are three important features of the collision geometry that will be discussed at length throughout this thesis. If such things could be seen directly, these would be observed by looking down the beam pipe (along the z axis) at the positions of the colliding nuclei in the transverse (xy) plane. For the sake of discussion, consider a collision system where the center of mass is at (0,0,0). The things to note are:

1. The colliding nuclei only ever overlap to a degree; complete overlap is vanishingly rare. Therefore, for each event, there is some distance that separates the center points of the nuclei (the centers of mass) in the xy plane. This distance is called the *impact parameter*, and it is denoted as b.

2. The centers of the nuclei also establish the orientation of the collision in the *xy* plane. With respect to the laboratory, the orientation will be different from event to event. The *reaction plane angle*, denoted as Ψ_R, is the azimuthal angle of the line passing through the center points of the nuclei.
3. The overlapping region in the *xy* plane is nearly circular when *b* is small, but the shape becomes elliptical with less overlap. The *eccentricity* describes the extent to which the overlapping matter is longer along the major axis than along the minor axis. This will be discussed again in Sec. 3.7.

A basic diagram of the features in the transverse plane is provided in Fig. 3.2. The circles represent the radii of the nuclei, but these sharp lines belie the actual diffuse nuclear edges. In order to present a sense of the amount of overlapping matter, the product of two overlapping density functions is shown using a series of contours. (These are three-dimensional density profiles of ^{197}Au nuclei projected onto the transverse plane. More details regarding the nuclear density functions are given in Sec. 3.3.)

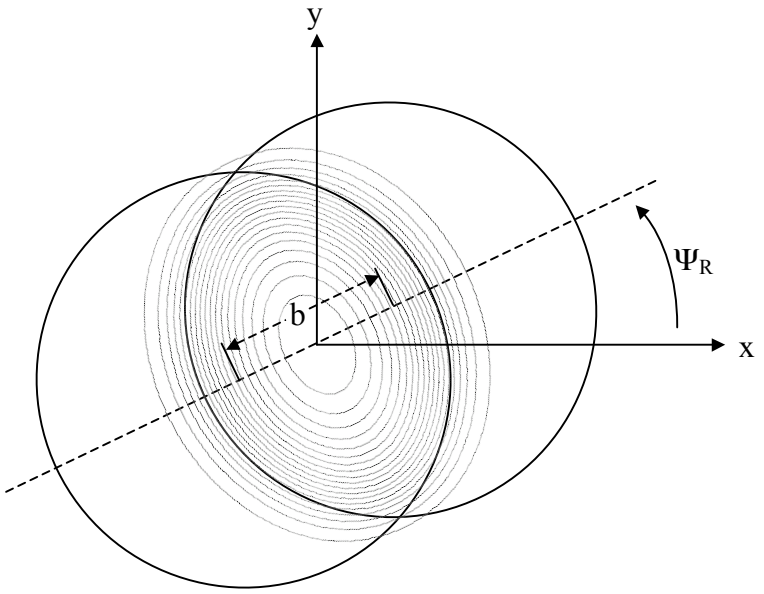

Figure 3.2: An illustration of the geometry of a collision. The contours show the product of two overlapping density functions for ^{197}Au separated by b = 5 fm. The outermost contour represents 5% overlap, and each contour thereafter is an additional 5% up to the innermost 95% contour. The magnitude of the impact parameter b and the eccentricity of overlap region change from event to event, as does the reaction plane angle Ψ_R.

Since the reaction plane angle Ψ_R was cited as an important feature of the geometry, what is the *reaction plane* itself? Considering again the collision system centered at (0,0,0), the reaction plane is defined by the z axis and, in the xy plane, by the line connecting the center points of the nuclei. Since Ψ_R changes event-by-event while the z direction does not, the "orientation of the reaction plane" will here forward refer only to the angle in the xy plane, while the alignment with the beam axis will be assumed.

Two terms are useful for describing the distribution of emitted particles relative to the collision orientation. Particles escaping the collision in the azimuthal direction

aligned with the reaction plane, in other words ($\phi_{particle} - \Psi_R$) ≈ 0 or π rad, are said to be *in-plane*, while those away from the reaction plane, at ($\phi_{particle} - \Psi_R$) ≈ $^1/_2$ π or $^3/_2$ π rad, are said to be *out-of-plane*.

The overlapping matter in a heavy ion collision is referred to as *participant matter*, or as the participating nucleons, while the unimpeded matter is called *spectator matter*. The number of participating nucleons is denoted as N_{part}. This value includes nucleons from both nuclei, therefore a collision of two gold nuclei, each having 197 nucleons, leads to a maximum N_{part} of 394. When the nuclei collide, the unopposed spectator matter nearly instantly shears away, continuing along its initial trajectory. It moves away so rapidly that it does not play a role in the very hot, dense medium created at the collision center. The spectator matter is unstable, and it quickly breaks apart into unbound protons and neutrons as it continues its unimpeded movement along the beam axis.

Finally, the impact parameter *b* is a means of quantifying the *centrality* of the collision. Highly overlapping nuclei are described using the relative terms *central* or *most central*, while lesser overlap is described as *mid-central*, and, in the case of grazing events, *peripheral*.

3.3: Introduction to the Glauber Model

A RHIC collision has a complex evolution, and, therefore many models are used (or are combined together) to describe different aspects of its progression. This section describes the principles behind one simple model called a Glauber[1] model. This model is commonly used to connect the *initial geometry* (*i.e.* the spatial distribution of the participant matter) to an experimental observable (for example, the total number of particles produced from a collision). Glauber models are also used to reveal interrelationships among the variables of the initial geometry (such as the impact parameter b and the number of participants N_{part}).

A Glauber model essentially treats a nucleus-nucleus collision as the superposition of many constituent nucleon-nucleon collisions. The opposing nucleons, approaching at relativistic speeds, are assumed to be frozen in position in the transverse (xy) plane during the course of the collision. In other words, it is assumed that the nucleons travel in straight-line trajectories along the beam axis. (This means that Glauber models only need to deal with the projection of the nucleons in the xy plane.)

A Glauber model relies on two basic inputs: (1) a nucleon-nucleon interaction cross-section (*i.e.* the target size a nucleon presents to an opposing nucleon) and (2) a probability function for the distribution of the nucleons within the nuclei.

The inelastic cross-section for proton-proton collisions (measured in millibarns mb) is used as the value for the nucleon-nucleon cross-section σ_{inel}^{NN} because it is well

---

[1] In the heavy ion community, any mention of Glauber is concerned exclusively with the scattering of high-energy particles on a nuclear potential. However, elsewhere, Roy Glauber is largely known for his work in quantum optics, for which he received the Nobel Prize in physics in 2005. The timing of the Nobel Prize ceremony precluded his attendance at the anual Ig Nobel Prize ceremony, where Glauber traditionally performs the duty of "keeper of the broom". In this position he is responsible for sweeping away paper airplanes that are thrown onto the stage during the Ig Nobel ceremony.

known up to and beyond $\sqrt{s}$ = 200 GeV. At $\sqrt{s}$ = 200 GeV, σ_{inel}^{NN} is 40 mb, and at $\sqrt{s}$ = 62.4 GeV, σ_{inel}^{NN} is 35.6 mb [Yao06]. The behavior of high-energy colliding neutrons is unknown, but it is assumed to be similar to protons. At this energy, the strong force is far more influential than the dissimilarities arising from the electrical charge. Diffractive and elastic processes among nucleons are generally ignored in high-energy, multi-particle collisions since they require a full treatment of the nuclear wave function [Mil07].

The Glauber model also requires a parameterization of the spatial distribution of the nucleons within the nuclei. A common parameterization of the Fermi density distribution for spherical nuclei is given in Eq. 3.1. This is based on a Woods-Saxon nuclear potential function [WS54]. The density distribution can also be thought of as the quantum-mechanical probability distribution for the position of a single nucleon.

$$\rho(r) \propto \frac{1}{1+\exp(\frac{r-r_0}{a})} \quad . \tag{3.1}$$

In Eq. 3.1, $\rho(r)$ is the nucleon density at some radial distance from the nucleus center, r_0 is the radius where $\rho(r)/\rho(0)$ falls to 50%, and a dictates the diffuseness[1] of the nuclear surface. For ^{197}Au, r_0 is 6.38 fm, and a is 0.535 fm, while for ^{63}Cu, r_0 is 4.20 fm, and a is 0.596 fm. These values reflect the charge distribution (*i.e.* the distribution of protons) within a nucleus determined via the elastic collisions of high-energy (short de Broglie wavelength) electrons [deV87].[2] The distributions are plotted for both nuclei in Fig 3.3.

[1] A more intuitive variable might be t, which is approximately 0.446 a and is defined as the distance over which the relative nuclear density falls from 90% to 10%. This is commonly referred to as the skin thickness.

[2] The charge density distribution may not accurately reflect the nucleon spatial distribution in certain nuclei with neutron skins.

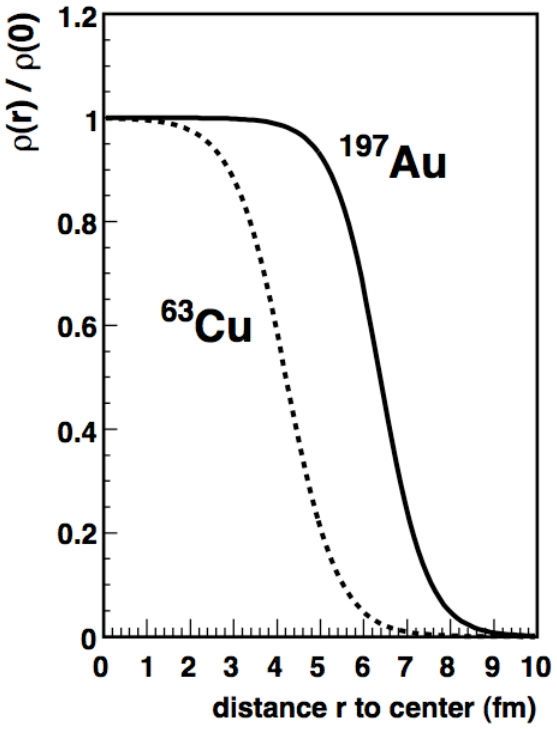

Figure 3.3: Fermi nuclear density distributions for ^{197}Au and ^{63}Cu scaled against their respective densities at $r = 0$ [Mil07].

3.4: Implementing a Glauber Model

There are two common methods of implementing a model based on the Glauber picture. One method, called an *optical Glauber model*, determines the attributes of the initial geometry simply by considering the overlap between the two smooth nuclear probability functions, separated by a distance b and weighted at each position by the nucleon-nucleon cross-section [Bia76]. Though some of the details of the model are neglected here (they can be found, for instance, in [Mil07] and [Sor03]), the smooth, overlap density profile in Fig. 3.4 is a useful picture to keep in mind regarding the optical model.

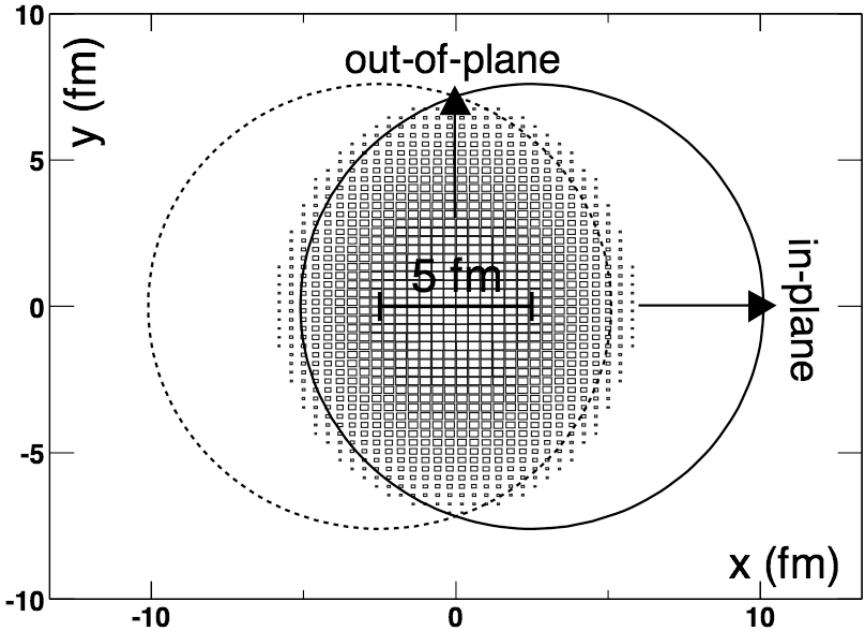

Figure 3.4: The overlap density profile of two colliding Au nuclei separated by b = 5 fm. The areas of the boxes are proportional to the magnitude of the overlap density. The interaction density comes from a wounded nucleon model, and this is all described in [Sor03].

The second sort of Glauber model, the kind used in this thesis, is a *Monte Carlo* (MC) simulation. Monte Carlo implies that, based on the relevant probability distributions, some aspects of the model are assigned randomly in each of many *events*. When a large number of these events are taken as a group, they essentially fold together the various input probability distributions to create a more complete (and not necessarily trivial) probabilistic picture.

The Monte Carlo method lends itself to illustration because it is based on several simple geometric rules. Figure 3.5 shows a single, random collision of two opposing nuclei. This is the type of picture that is generated again and again (the distributions are said to be *thrown* in a Monte Carlo simulation) to form a probabilistic understanding of the initial geometry.

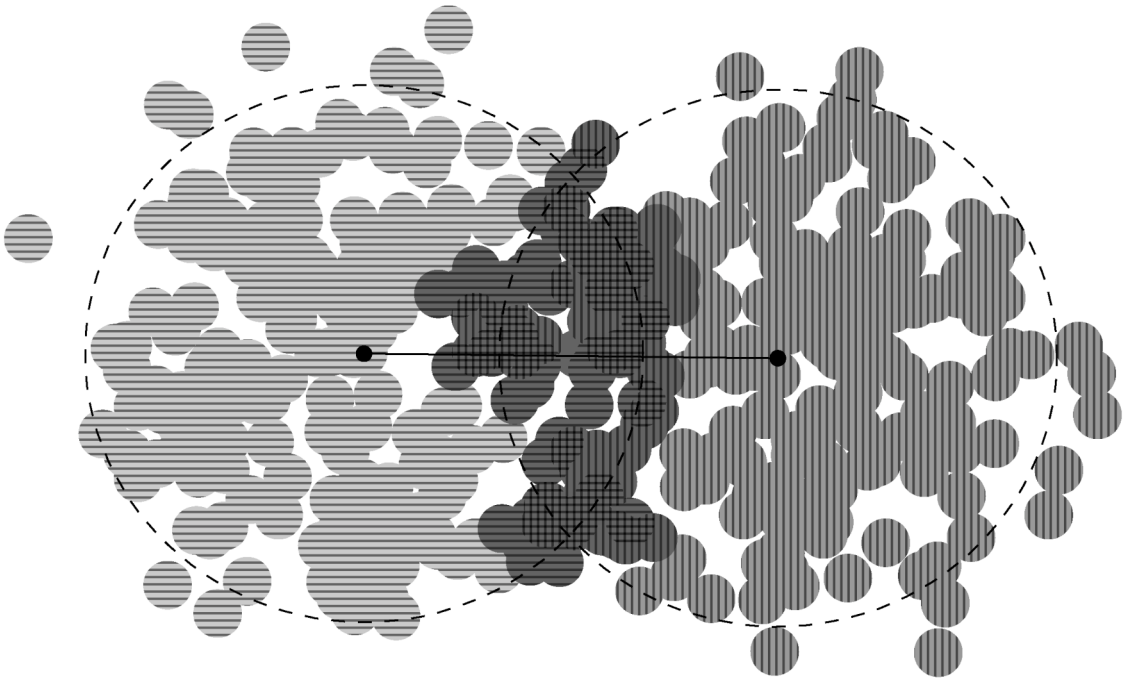

Figure 3.5: The randomly generated distribution of nucleons in a Au+Au collision from the PHOBOS MC Glauber model. (This model is described in [Alv08a].) The lighter shaded circles on either side represent the spectator nucleons. The darkest circles are participant nucleons. The size of the circles are based on the nucleon-nucleon cross section (*i.e.* ½ $\sigma_{inel.}^{NN}$). The spatial positions of the nucleons are based on Woods-Saxon probability distributions (with each nucleus centered along the horizontal direction at ± ½ *b*). Participant nucleons are those circles from one nucleus that are touching one or more circles from the opposing nucleus. Horizontal and vertical hashes are shown here to help distinguish which nucleons belong to which nucleus.

As a simple example of how this model is used, consider the relationship between the impact parameter b and the number of participating nucleons N_{part}. Even for a constant impact parameter, from event to event the number of participant nucleons will vary. Both a mean value and also the spread of the N_{part} distribution can be found for a single value of b, and this, in turn, can be done over many values of b to form a complete distribution. Such a distribution is shown in Fig 3.6.

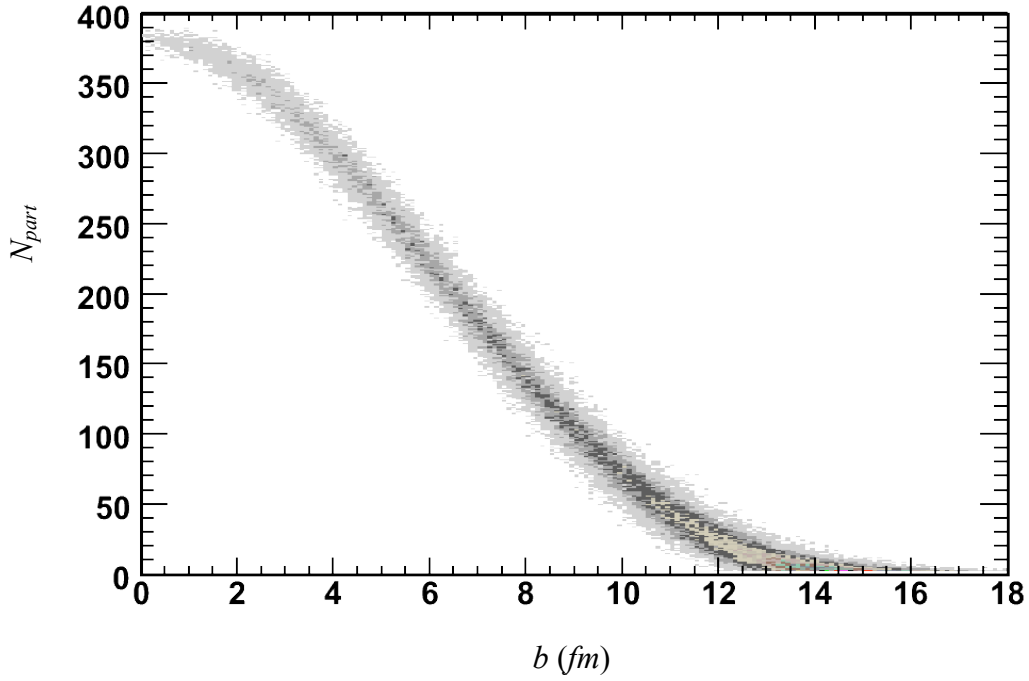

Figure 3.6: The relationship between N_{part} and b for Au+Au collisions as calculated by the PHOBOS Glauber Monte Carlo model.

The MC Glauber model is preferred because it takes into account some correlations among nucleons that are neglected in the optical model. The MC model addresses the real possibility that one nucleon sits behind another (along the beam axis). In a collision, either both or neither of the nucleons will be struck, but rarely just one or

the other [Bak04, Alv08b]. The optical model misses this nucleon shadowing interaction since it treats each nucleon independently.

3.5: Quantifying the centrality

In Sec. 3.2, collisions were described as peripheral and central, but *centrality* also has a quantitative meaning. It is a variable used to categorize collisions according to their degree of overlap. Figure 3.7 was generated using a Glauber MC model, and it illustrates the probability that a collision will have an impact parameter of less than some value b. The low slope near $b = 0$ fm means that it is unlikely to have a direct head-to-head collision, and the low slope beyond $b = 16$ fm means that it is unlikely that two nuclei will touch when they are largely separated.

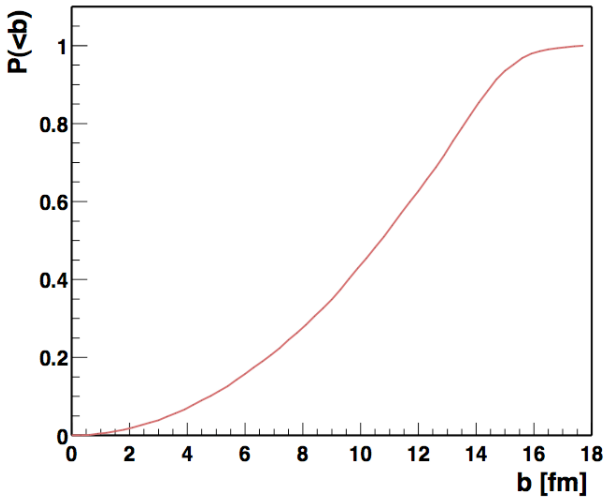

Figure 3.7: The probability, for Au+Au collisions at $\sqrt{s_{NN}} = 200$ GeV, of having an impact parameter less than b [Hol05].

With Fig. 3.7 in consideration, the top 10% centrality refers to those collisions starting at $b = 0$ fm up to the point where $P(<b) = 0.1$ (that is 0 fm < b < ~5 fm). In

practice, the collisions are divided up into centrality bins, *e.g.* 10-15% centrality, 15-20%, and so on, with the lower numbers being the more central bins.

3.6: Experimental measurement of the centrality

A Glauber model provides relationships among properties of the initial geometry (*e.g.* number of participants, impact parameter, and percent centrality). However, none of these initial properties are directly observable, and, like everything else in the experiment, they must be reconstructed from the final-state particle distributions.

Two particular final-state observables are most commonly used to establish a connection to the degree of nuclear overlap:

1. The number of spectator nucleons escaping the collision is the complementary variable to the number of participant nucleons (*i.e.* $N_{total} = N_{part} + N_{spectators}$). Note that, of those spectator nucleons, only the neutrons proceed, undeflected by subsequent steering magnets, to be detected at the zero degree calorimeters (ZDCs) at each of the RHIC experiments.
2. The *multiplitiсy*, which is the number of particles emanating from a collision, increases as the degree of initial overlap increases. The PHOBOS experiment uses many detectors that are insensitive to neutral particles, and, therefore, a relationship is formed between the *charged-particle multiplicity* and the centrality. In practice, the multiplicity is deduced from the number of particles arriving at a single detector in a limited region of pseudorapidity. For example, the number of particles arriving at the paddle counter arrays can be related to the full multiplicity (*i.e.* the multiplicity integrated over all angles).

The relationship between the total energy deposited in the ZDCs and the mean energy in the paddle counters[1] is explored in Fig. 3.8.

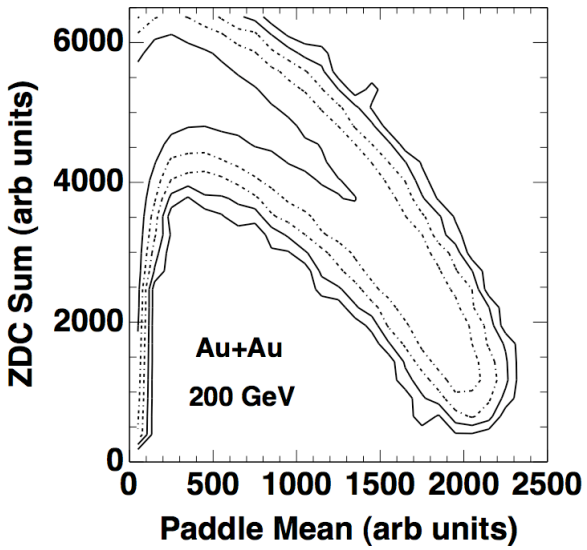

Figure 3.8: A contour plot illustrating the relation between the signal from the ZDC arrays (a measure of spectator neutrons) versus the signal in the paddle arrays (multiplicity dependent) [Bac05a]. The contours are logarithmic, growing by a factor of 4 moving inward through each successive contour.

For the most part, there is an expected anticorrelation between the paddle mean and the ZDC sum. This agrees with the presumption that the multiplicity is directly related to the size of the participant region, and that this, in turn, is inversely related to the number of spectators.

At the lowest paddle mean values, there is no longer a strong correlation between the paddles and the ZDCs. This behavior arises from a class of ultra-peripheral collisions in which there is only a slight excitation of the two nuclei. This may be from a strong-force interaction, or it may even be an electromagnetic interaction as the nuclei pass by

[1] PHOBOS uses a truncated paddle mean, which was found be a better measure of the centrality. The truncated mean simply excludes the two paddles with the highest response in a given event from the calculation of the mean.

one another [Bau98]. The minor excitation leads to a variety of results, ranging from the evaporation of a single nucleon to the complete spallation of the two nuclei (with many intermediate possibilities). In the situation where the nuclei completely disintegrate, a comparatively large number of neutrons arrive at the ZDCs. At the same time, there is the possibility of some nucleons being ejected with enough transverse kinetic energy that they arrive at the paddle counters. If, however, the nuclei are only slightly excited as they pass, then there is little chance of particles reaching the paddle counters while there is still the probability of seeing a range of neutrons arriving at the ZDCs. The least substantial collisions that can be discerned experimentally are those in which a single neutron is detected at each ZDC. In this analysis these peripheral situations do not play a role.

In theory, it is quite simple to establish centrality bins in the data. Since the number of particles in the paddle counters increases with increasing nuclear overlap, the paddle energy spectrum (paddle mean) can be simply divided into bins (*i.e.* 10% of the area under the histogram correlates to the top 10% centrality). This partitioning is illustrated in Fig. 3.9, which is the data from Fig 3.8 projected onto the paddle mean axis.

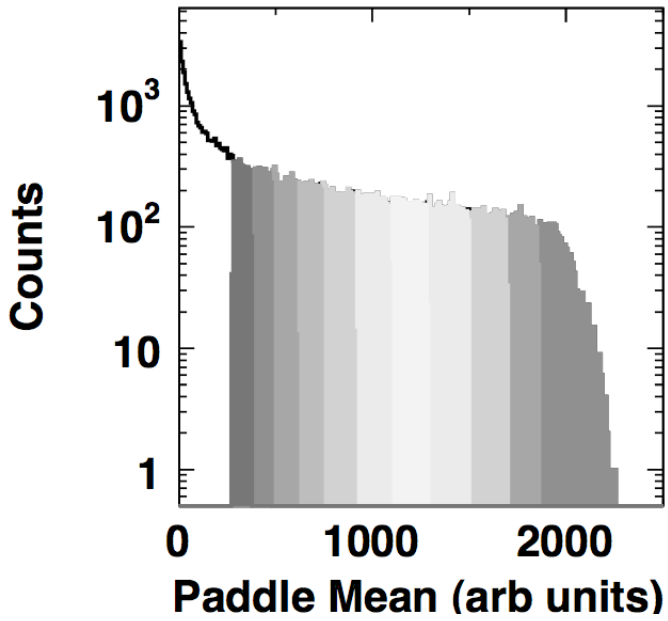

Figure 3.9: The paddle signal, divided into bins of centrality [Bac05a]. Starting at the right, the bins are from 0-3%, 3-6%, 6-10%, followed by bins of 5% width down to 50% centrality.

The reality is somewhat more complicated because the experiment does not trigger on all events with equal efficiency. In peripheral events particularly, the multiplicity is low and the few outgoing particles may miss either of the two paddle arrays completely. (Remember that the paddle arrays act as trigger detectors, as well as providing a measure of the centrality.) In contrast, for the more central events where the multiplicity is high, it is very likely that the experiment will be triggered and that the collision will be recorded. What this means, regarding Fig 3.9, is that there should be more counts at the low paddle mean portion of the histogram than are actually observed. The problem is, without knowing the area of the full distribution (*i.e.* without knowing the trigger inefficiency), it is impossible to say what range of paddle mean energy corresponds to *e.g.* the top 10%.

To resolve this problem, two models are used together. The first is the Monte Carlo event generator HIJING that uses known particle distributions from p+p collisions to pattern heavy ion collisions. The number of overlaid p+p collisions is based on N_{part}, which is found using an internal Glauber model. Details of this model can be found in [Wan91]. A second MC simulation, GEANT, is used to propagate the particles from HIJING through a simulated detector [GEA94]. Together these form a probabilistic model that can be used to find, among other things, the fraction of collisions that the trigger misses and the corresponding paddle mean energy for those collisions (*i.e.* the simulated data needed to find the correct integral of Fig 3.9). A description of this procedure is included in the Appendix of the PHOBOS "white paper" [Bac05a].

Having established the connection between an experimental observable (the mean paddle energy) and a property of the initial geometry (the centrality), the rest of the interrelationships among the initial geometry can be considered. Figure 3.10, for example, illustrates the distribution of N_{part} within each of the centrality bins shown in Fig 3.9.

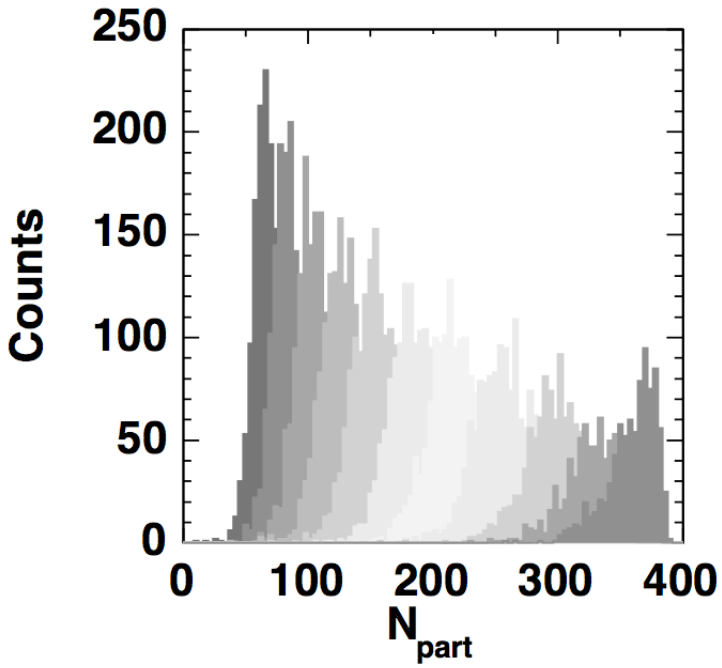

Figure 3.10: The number of participant nucleons for each centrality bin as determined from HIJING and GEANT MC models [Bac05a].

3.7: Eccentricity modeling

Turning to a different aspect of the initial geometry, the eccentricity was mentioned in Sec. 3.2 as a term for describing the shape of the participant matter. In this section, the definition of eccentricity is further formalized. Considering the initial spatial distribution of the participant nucleons, the variance σ^2 (for example, $\sigma_x^2 = \langle x^2 \rangle - \langle x \rangle^2$) is chosen as the measure of length of the distribution along some direction. (This follows the convention set in [Alv08b]). The variance along the minor axis is denoted σ_{min}^2, and, along the major axis, it is σ_{maj}^2.

The eccentricity is defined in Eq. 3.2 as

$$\varepsilon = \frac{\sigma_{\text{maj}}^2 - \sigma_{\text{min}}^2}{\sigma_{\text{maj}}^2 + \sigma_{\text{min}}^2} \quad . \tag{3.2}$$

It should be noted, though, that the definition of eccentricity in the nuclear community is different from the normal mathematical definition of the eccentricity of an ellipse.[1]

The Glauber MC model is used to relate the eccentricity to other geometric parameters such as N_{part}, b, and the centrality bin. In a single Glauber MC event (Fig. 3.5) the participant nucleons are not really distributed in a smooth elliptical shape. Rather, the finite number of colliding nucleons often leads to a relatively lumpy distribution.

Two possible interpretations of the Glauber MC model have arisen, and the difference between them is namely how the major/minor axes are orientated. By convention, the Glauber model initializes the two nuclear density functions so that they are separated along the x axis, centered at either + or - ½ b. (Also, after the nucleons are thrown, the nuclei are generally translated slightly so that their respective centers of mass lie on the x axis at ± ½ b as well.) In this configuration, the reaction plane orientation is always along the x axis (*i.e.* $\Psi_R = 0$).

The first Glauber MC interpretation of the eccentricity is one in which the minor axis is always defined as the x axis (*i.e.* in-line with the reaction plane orientation). Taken on average over many events, this is the shortest dimension of the participant

---

[1] The formula used in mathematics to describe the eccentricity of an ellipse is $\varepsilon = \sqrt{1 - \frac{b^2}{a^2}}$, where a is the semimajor axis and b is the semiminor axis.

distribution. Because of its particular orientation, this interpretation is denoted as the *reaction plane eccentricity*, and it is defined in Eq. 3.3

$$\varepsilon_{RP} = \frac{\sigma_y^2 - \sigma_x^2}{\sigma_y^2 + \sigma_x^2} \quad . \tag{3.3}$$

In a second interpretation of the eccentricity, the orientations of the major and minor axes are found on an event-by-event basis. The random placement of a finite number of nucleons means that the overlap region will have a slightly different shape from event to event (even while having the same impact parameter). Figure 3.11 illustrates a circumstance in which, owing to these random position fluctuations, the participant region is tilted. This is an example where the *reaction plane eccentricity* does not accurately reflect the elongation of the participant region. Therefore, instead, the *participant eccentricity* is calculated relative to the principal axis of the participant distribution y' and its perpendicular x', as in Eq. 3.4.

$$\varepsilon_{part} = \frac{\sigma_{y'}^2 - \sigma_{x'}^2}{\sigma_{y'}^2 + \sigma_{x'}^2} \quad . \tag{3.4}$$

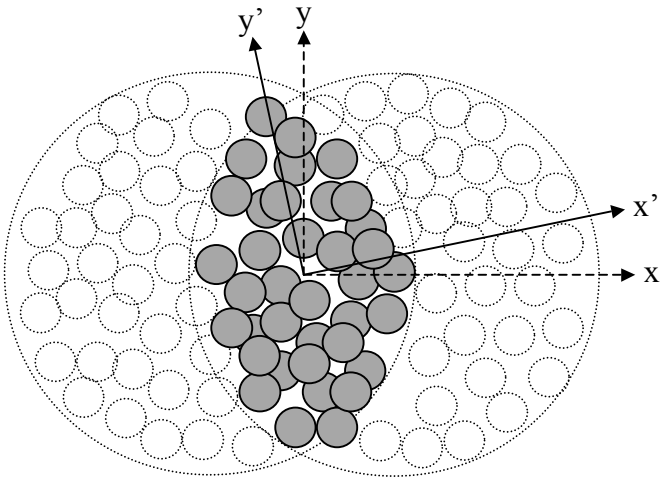

Figure 3.11: A cartoon illustrating the position of the nucleons in the transverse plane [Alv08b]. In this case, random position fluctuations result in a slightly tilted participant region (shaded nucleons) relative to the nominal x and y axes. The principal axes (x' and y') of the participant nucleon distribution provide an alternative orientation against which the eccentricity can be measured.

In practice, the participant eccentricity calculation need not involve the rotation of the coordinate system. Regardless of the initial, arbitrary rotation, the participant eccentricity is provided by Eq. 3.5,

$$\varepsilon_{part} = \frac{\sqrt{(\sigma_y^2 - \sigma_x^2)^2 + 4(\sigma_{xy})^2}}{\sigma_y^2 + \sigma_x^2} \quad , \tag{3.5}$$

in which σ_{xy} is the covariance ($\sigma_{xy} = \langle xy \rangle - \langle x \rangle \langle y \rangle$).

A few important behaviors of ε_{RP} and ε_{part} should be noted:

The first is that the possible range of ε_{RP} returned by the Glauber MC extends from -1 to +1, while the range of ε_{part} is between 0 and +1. What is the physical interpretation of negative ε_{RP}? While the participant nucleons might be expected to have a longer distribution in the *y* direction than along the *x* axis, the random position fluctuations mean that this is not necessarily always the case. This kind of inverted distribution (*i.e.* when $\sigma_x^2 > \sigma_y^2$) results in negative values of ε_{RP}. Meanwhile, because ε_{part} is calculated relative to the principal axis, the smallest possible value it can have is zero (implying that the participants are evenly distributed in all directions). Therefore, observe that Eq. 3.5 cannot assume a negative value, while Eq. 3.3 can.

The second important feature to note is that the agreement between ε_{RP} and ε_{part} is better when considering heavier nuclei (*i.e.* nuclei with greater numbers of nucleons). This is true in all but the most peripheral events, at which point the limiting behavior of ε_{RP} and ε_{part} differ. The per-event tilting of the participant region ultimately arises from the model's use of a finite number of nucleons as opposed a representation using smooth nuclear density distributions. In a smooth overlap distribution, the participant ellipse will always be oriented along the *x* and *y* axes. When heavier nuclei are modeled, the greater numbers of nucleons are in better agreement with the smooth limit (there is less of a finite-number effect), and the orientation disagreement that distinguishes ε_{RP} from ε_{part} is diminished.

Figure 3.12 provides the mean values of ε_{RP} and ε_{part} as a function of N_{part} for both Au+Au and Cu+Cu collisions. These values are relatively energy independent. A comprehensive survey of the parameter space is provided in [Alv08b].

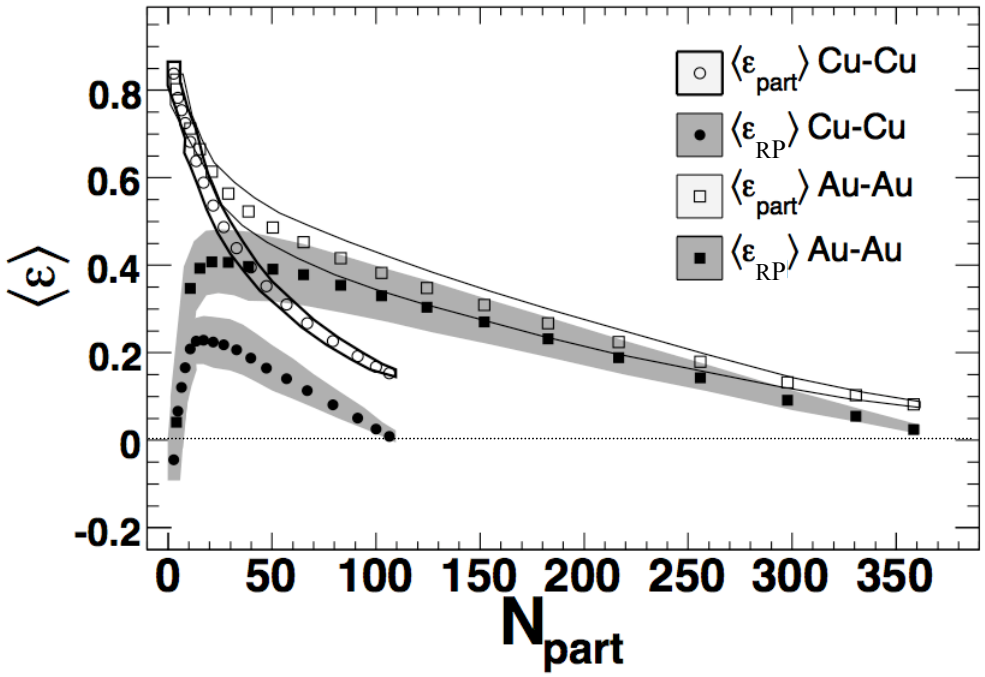

Figure 3.12: Mean values of ε_{RP} and ε_{part} as a function of N_{part} for Au+Au and Cu+Cu collisions from [Alv07]. The bands represent the 90% C.L. systematic errors.

Considering a smooth overlap distribution (such as shown in Fig. 3.2 and Fig. 3.4), collisions with increasing centrality approach the limit of zero eccentricity (*i.e.* the overlap region is circular). In the MC prescription, there are position fluctuations, but on average these do not cause elongation in any particular direction. Sometimes ε_{RP} is positive, and other times it is negative, but at the most central limit, the eccentricity fluctuations average out to zero. The same is not true for ε_{part}. Fluctuations only result in positive values of ε_{part}, and, therefore, for the most central events, the mean is non-zero. Of additional noteworthiness, the difference between ε_{RP} and ε_{part} for the most central

events is more pronounced in the lighter Cu+Cu system (*i.e.* fewer nucleons) for the reason previously described.

This analysis extends down to around 25 participants, below which trigger and vertexing efficiencies become unfavorable. Below this, the limiting behavior at very small N_{part} will not play a role, but it is interesting to consider. It is easiest to examine the very peripheral limit where there are only two participating nucleons (one from each nucleus). The principal axis will pass through the two nucleons, and there is, by definition, no spread perpendicular to that. Therefore, ε_{part} will be 1. Meanwhile, the respective orientation of the participants will be arbitrary in the fixed reaction plane coordinate system. The fluctuations of ε_{RP} will mostly be equally positive and negative, and the mean will tend toward zero.

Chapter 4: Origin and Measurement of Elliptic Flow

4.1: An informal introduction

Let us briefly restate the essentials of a RHIC collision. Approaching at relativistic speeds, the flattened nuclei are effectively walls of hadronic matter. They do not stop *per se*, rather they pass through each other, exciting the vacuum in their wake. The binding energies of the nuclei are miniscule in comparison, and the unopposed spectator matter shears away almost instantly. Depending on the centrality of the collision, the remaining participant matter has a natural spatial anisotropy in the transverse plane. The color field connecting the participant matter stretches longitudinally and then relaxes through the production of matter, antimatter, and photons. The profusion of generated particles leads to a decreased mean free path, and we can suppose that at some time early in the collision evolution (perhaps within a few fm/c) the system comes to thermodynamic equilibrium on a local scale.

The hot expanse of matter is densest at the collision center, and, with the removal of the spectators, the participant system is surrounded by empty space. In a hydrodynamic description, a pressure gradient develops in the transverse plane extending from the collision center outward towards the vacuum. Considering for a moment an elliptical overlap profile, the pressure gradient along the minor axis (in-plane) is steeper than the pressure gradient along the major axis (out-of-plane). This results in an extra 'push' given to the in-plane particles. What began as a spatial anisotropy of the participant matter evolves into a momentum anisotropy, and it is ultimately observed as an anisotropy in the final-state distribution of particles. This collective back-to-back

emission pattern in the transverse plane is called *elliptic flow*, and its magnitude is expected to be proportional to the eccentricity of the participant system. Figure 4.1 illustrates this phenomenon.

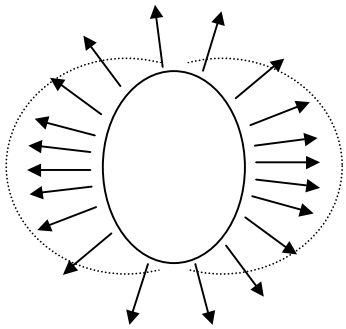

Figure 4.1: A cartoon depicting the initial shape of the participant region (in the *xy* plane), with lines emphasizing the azimuthal density distribution of the emitted particles.

Elliptic flow is sensitive to the very early time evolution of the collision. Just after the impact, the system is in a non-thermal or pre-equilibrium state. As such, hydrodynamic pressure gradients do not develop, and, during this time, any expansion will be isotropic. Under this uniform expansion period, the initial ellipsoidal shape will become more rounded. If pressure gradients form during later times in the collision evolution, when the spatial anisotropy has decreased, then there will be a smaller elliptic flow signal. This is illustrated in Fig. 4.2.

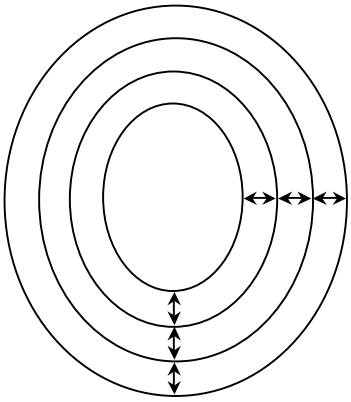

Figure 4.2: As the system expands uniformly, the ellipsoidal matter becomes more rounded (*i.e.* the innermost ellipse has a greater aspect ratio than the outer one).

It was not obvious *a priori* that elliptic flow would be strongly observed at RHIC [Hei99, Ris96b]. The QGP produced at RHIC was initially conceived as a weakly interacting medium, which is to say that the constituent particles would move about independently from one another. Without strong inter-particle interactions, a hydrodynamic pressure gradient would not develop until, perhaps, during the later hadronic phase. By this time, the initial spatial anisotropy would be notably diminished.

The significance of *flow* (the unadorned term referring to any mode of collective expansion) is that it probes the very early stages of the collision. Its presence suggests a rapid thermalization of the system, and, using the framework of hydrodynamics, flow establishes the time scale at which the initial, coherent energy turns into random thermal motion. As was noted in Sec. 1.8, this is an essential ingredient in revealing the temperature of the medium.

4.2: Quantifying elliptic flow

The azimuthal anisotropy of the particles is characterized with a Fourier decomposition. Equation 4.1 shows the commonly used parameterization for the number of particles *N* observed at each azimuthal angle ϕ with respect to the reaction plane angle Ψ_R

$$\frac{dN}{d(\phi - \Psi_R)} \propto 1 + 2\sum_{n=1}^{\infty} v_n \cos(n(\phi - \Psi_R)) \quad . \tag{4.1}$$

Here, *n* represents the Fourier harmonic, and the coefficient v_n is called the *anisotropy parameter*. This is not a true Fourier decomposition because the expected sine terms are omitted. This means that Eq. 4.1 is limited in the array of azimuthal shapes that can be reconstructed. The sine terms are the components that potentially break the mirror symmetry across the reaction plane, and, since this does not match the intended physical picture, these terms are excluded.

The first two instances of v_n in Eq. 4.1 are given names. The parameter v_1 is the *directed flow* anisotropy parameter, while v_2 is the *elliptic flow* anisotropy parameter. Each of the v_n parameters represents the magnitude of a harmonic deviation on top of the uniform transverse distribution of particles, called the *radial flow*.

For illustration, Fig. 4.3 shows the relationship between the variable v_2 and the azimuthal density distribution described by Eq. 4.1.

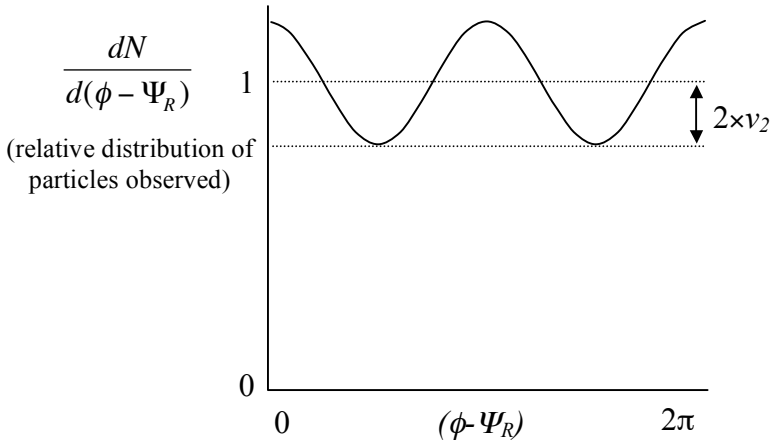

Figure 4.3: A cartoon illustrating an idealized azimuthal distribution (relative to the reaction plane) as described by Eq. 4.1. For illustration purposes, v_2 is the only non-zero term in the expansion.

In the past few years, the v_4 term has received increasing attention [Kol03, Ada05, Abe07]. Figure 4.4 shows that, to fit an ellipsoidal azimuthal distribution, v_4 is useful in correcting a waist that develops for large values of v_2.

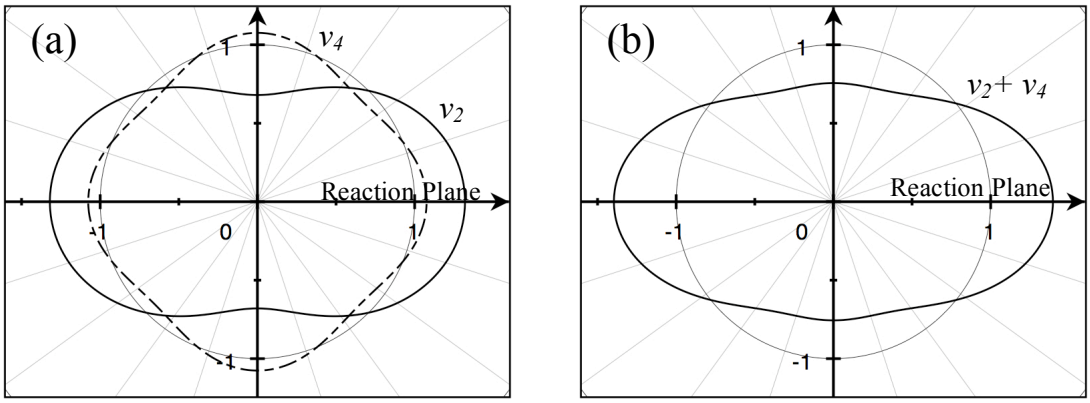

Figure 4.4: These azimuthal plots show the contributions of the 2nd and 4th order harmonics (panel a) to produce a relatively elliptical composite function (panel b). In this case, v_2=0.16 and v_4= 0.038 are the coefficients used in Eq. 4.1. Adapted in part from [Ada05].

The final-state particle distribution may be subdivided, for example into different bins of pseudorapidity or transverse momentum, or grouped according to species (*e.g.* pions, kaons, protons, *etc.*). It is useful to consider the azimuthal distribution $dN / d(\phi - \Psi_R)$ separately for these different subsets in order to gain a more complete understanding of the hydrodynamic expansion. Observations of this sort are called *differential* flow measurements (while those that do not distinguish among the particles are called *integrated* flow measurements).

As a final note, there are a number of phenomena that generate local azimuthal patterns but do not reflect a larger collective motion of particles [Bor00, Bor01, Kov02]. These are generally referred to as *non-flow effects*. For example, *jets* result from hard scattering among the initial colliding particles (*i.e.* during pre-equilibrium), and most commonly they result in the back-to-back ejection of matter. Since this is a scattering phenomenon, not driven by hydrodynamic pressure gradients, a method of measurement is chosen that is generally insensitive to the resulting local anisotropy.

4.3: Measurement of elliptic flow

There are a number of experimental techniques that have been developed throughout the years of flow measurements in heavy ion collisions. A recent overview of the prevalent techniques used at RHIC is provided in [Abe08]. A variation on the well-established event plane technique pioneered by Poskanzer, Voloshin, and Ollitrault [PV98, Oll93] is used in this analysis. This research is an extension of the earlier work at PHOBOS by Carla Vale and Nigel George. The technique was employed in previous measurements of elliptic flow for Au+Au at $\sqrt{s_{NN}} =$ 200 GeV, and it is presented in [Bac05b] and also documented extensively in Carla Vale's thesis [Val04].

Limiting the present discussion to the 2nd harmonic (*i.e.* elliptic flow), the essential point of the event plane technique is as follows: The reaction plane orientation Ψ_R is a parameter of the initial geometry, and it is therefore unknown. It must be reconstructed experimentally using the final-state distribution. To do this, the azimuthal anisotropy of the final-state is *itself* used as the means of determining the collision orientation. For the 2nd order harmonic, one looks for the angle with the greatest back-to-back emission, and this is used as an estimate of Ψ_R. Such an estimate is called an *event plane* angle, and, for the 2nd harmonic, it is designated as Ψ_2. (Note that a back-to-back pattern is periodic beyond π rad, therefore, $0 \le \Psi_2 < \pi$.)

On a per-collision basis, the azimuthal particle distribution (the distribution of ϕ) is reoriented relative to the event plane (becoming the distribution of ϕ-Ψ_2). Neglecting the uncertainty of Ψ_2 as an estimate of Ψ_R, the particles in each event are now in a commonly oriented nuclear coordinate system (*e.g.* ϕ-Ψ_2 = 0 rad means that a particle is in-plane and ϕ-Ψ_2 = ½ π rad means it is out-of-plane). Therefore, the azimuthal distributions taken from separate events can be added together. The ensemble distribution averaged over many events can be described with a slightly modified version of Eq. 4.1. Here, we are only concerned with the 2nd harmonic, and, instead of considering the distribution of ϕ-Ψ_R, we have a distribution of ϕ-Ψ_2. Therefore we arrive at Eq 4.2

$$\frac{dN}{d(\phi - \Psi_2)} \propto 1 + 2v_2^{obs}\cos(2(\phi - \Psi_2)) \ . \qquad 4.2$$

The measured distribution of $dN/d(\phi\text{-}\Psi_2)$ can be fit using the right side of Eq. 4.2 to find v_2^{obs}, which is the observed elliptic flow anisotropy parameter. The 'observed'

designation is an important caveat. It means that the use of Ψ_2 as a statistically limited estimate of Ψ_R must be reconciled in order to find the true value of v_2. This is an important characteristic of the event plane method, and it will be described further in Sec. 4.6. For now, it is sufficient to explain that the average deviation of Ψ_2 (a measured value) from Ψ_R (an exact but unknown value) is described by the *resolution*, and that the true value of v_2 can be found by dividing v_2^{obs} by this resolution. The deviation of Ψ_2 from Ψ_R is not experimentally accessible—at least not directly. Instead the resolution must be determined by comparing two independent measurements of Ψ_2 from the same event (*i.e.* two similarly made estimates of a constant Ψ_R). In the event plane method, the particles are divided into two *subevents*, and the independent measurements made with those subevents are designated as Ψ_{2A} and Ψ_{2B}.

The steps used in this particular analysis are as follows:

1. The 2nd order event plane angle Ψ_2 is determined for each event.
2. The average resolution, taken over many events, is determined using two *subevents* from each collision.
3. The commonly oriented azimuthal distribution (ϕ-Ψ_2) is built up over many events. At this point, it may carry some unwanted distortions resulting from detector imperfections.
4. A *mixed-event background* distribution is constructed. This intentionally eliminates the elliptic flow correlation by relating the azimuthal angles of the particles to event plane angles measured in separate collisions.
5. The background (step 4) is subtracted from the foreground (step 3). This ostensibly leaves only the azimuthal variation coming from the elliptic flow, and

it eliminates the multi-event detector imperfections. This distribution is fit to determine v_2^{obs}.

6. Finally, the observed flow is divided by the resolution to find the true flow.

A generic treatment of these steps will be described in the following sections, along with some of the basic problems endemic to flow analyses in general and this technique in particular. The implementation using the PHOBOS detector will be described Chapter 5.

4.4: Flow correlations and autocorrelations

Within a single event, several different subsets of particles are used. One group of particles is used to determine Ψ_2, while another group is used to build up the ϕ-Ψ_2 distribution. This division into two separate groups avoids trivial *autocorrelations*, a term that describes the case in which a selection parameter biases the measurement.

While this sort of autocorrelation represents a relatively straightforward case, the possible correlations generally run the gamut between the trivial all the way to the important (*e.g.* the collective flow signal itself). Some unwanted correlations are not immediately obvious, and they can impact the measurement to a degree rather than manifesting as an obvious fault. For example, a subtle autocorrelation may still arise even when the event plane Ψ_2 is found using one subset of particles, and the azimuthal distribution ϕ-Ψ_2 is built up using another. Two particles, one assigned to each of these separate steps, may both be the decay products of a single parent particle, thereby connecting two pieces of information that were assumed to be independent. For such closely related pairs of particles, this is considered an autocorrelation as well. In another sense, all of the thermalized particles are correlated if the collision is traced back to its origin. The flow signal is an azimuthal correlation with the reaction plane, and, of

course, it is a result of earlier interactions among particles as well. The distinction, which was pointed out in Sec. 4.2, is that the flow correlation is a global phenomenon rather than a localized effect.

In this analysis, the event plane angle Ψ_2 and the azimuthal distribution ϕ-Ψ_2 are determined using particles in different regions of the detector, separated by a gap in pseudorapidity. This is expected to reduce the contribution of many non-flow particle correlations [Bor01], and there is experimental evidence to suggest that this expectation is reasonable [Ack01].

4.5: Event plane measurement

From the azimuthal angles ϕ_i of a set of *i* particles in a single collision, an *event flow vector* for the 2nd harmonic $\boldsymbol{Q_2}$ is determined. (If the values of ϕ_i are multiplied by 2, then a back-to-back emission pattern will become 2π-periodic, and $\boldsymbol{Q_2}$ will be oriented toward the maximum with a magnitude proportional to the strength of the anisotropy.) The *x* and *y* components of $\boldsymbol{Q_2}$ are given in Eq. 4.3 and Eq. 4.4

$$Q_{2x} = \boldsymbol{Q_2}\cos(2\Psi_2) = \sum_i w_i \cos(2\phi_i) \ , \tag{4.3}$$

$$Q_{2y} = \boldsymbol{Q_2}\sin(2\Psi_2) = \sum_i w_i \sin(2\phi_i) \ . \tag{4.4}$$

The event plane for the 2nd harmonic is given by Eq. 4.5

$$\Psi_2 = \frac{1}{2}\left(\tan^{-1}\frac{Q_{2y}}{Q_{2x}}\right), \tag{4.5}$$

and it has a range of $0 \le \Psi_2 \le \pi$. The weighting coefficient w_i is a means of accounting for possible azimuthal detector asymmetries. Over many randomly oriented events, the average probability of detecting a particle should not depend on the azimuthal direction. Therefore, in this analysis, the weight is inversely proportional to the detection probability taken relative to the probability of detection at other azimuthal angles. (The weighting coefficients may also be used to emphasize those particles that are influenced to a greater extent by the hydrodynamic expansion [Abe08], but this is not done in this analysis.)

As a final note, because the collision is equally likely to be oriented in any direction, a histogram of the event plane angles should be flat (provided that the statistics are sufficient).

4.6: Event plane resolution

In the event plane technique, the observed flow v_2^{obs} is related to the true flow v_2 as

$$v_2 = \frac{v_2^{obs}}{R}, \tag{4.6}$$

where R is the *resolution*, defined in Eq. 4.7

$$R = \left\langle \cos\left(2(\Psi_2 - \Psi_R)\right)\right\rangle. \tag{4.7}$$

The resolution is a way of expressing the average deviation of Ψ_2 from Ψ_R. The angle brackets indicate that this average is taken over many events. The observed flow is always less than the true flow, and the resolution is therefore always less than 1.

The resolution cannot be determined as it is presented in Eq. 4.7 because Ψ_R is not directly accessible experimentally. Instead, the two subevent measurements Ψ_{2A} and Ψ_{2B} (which are each estimates of Ψ_R from a single event) are observed over many events. Their mutual deviation, taken on average, is then expressed in terms of the deviation relative to Ψ_R.

The event plane method specifies that the two subevents used to determine Ψ_{2A} and Ψ_{2B} should have an equal number of particles and an equal magnitude of elliptic flow. Subevents covering equally sized, opposite regions of pseudorapidity meet these criteria. (Both the multiplicity distribution as a function of pseudorapidity and the elliptic flow as a function of pseudorapidity are provided in Appendix C.) Additionally, this choice of subevents eliminates problems arising due to momentum conservation [Dan88].

Assuming only pure flow correlations between the subevents, the relationship between Ψ_{2A} (or Ψ_{2B}) and Ψ_R is given by Eq. 4.8

$$\left\langle \cos\left(2(\Psi_{2A} - \Psi_R)\right)\right\rangle = \sqrt{\left\langle \cos\left(2(\Psi_{2A} - \Psi_{2B})\right)\right\rangle} \quad . \tag{4.8}$$

The full event plane measurement Ψ_2 uses the combined statistics of both subevents. The desired relationship between Ψ_2 and Ψ_R (*i.e.* the resolution needed for equation 4.6) is shown in terms of Ψ_{2A} and Ψ_{2B} in Eq. 4.9

$$R = \sqrt{2}\alpha\sqrt{\left\langle \cos\left(2(\Psi_{2A} - \Psi_{2B})\right)\right\rangle} \quad . \tag{4.9}$$

The value α is a correction factor described in [Val04]. When the resolution is low, as it is in this analysis, α is nearly 1. As the resolution increases, α becomes less than 1, as shown in Fig. 4.5. This correction is used to describe a known multiplicity dependence that grows as the resolution increases [PV98].

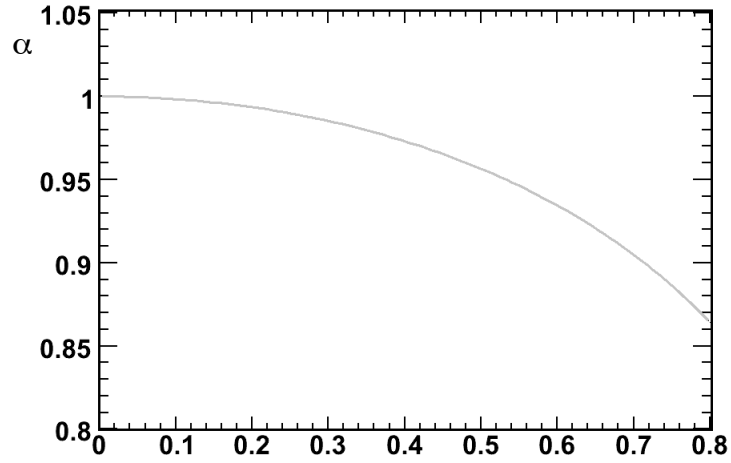

Figure 4.5: The correction factor α as a function of resolution.

4.7: Mixed-event background

A mixed-event background generally implies the sampling of particles from different events in order to eliminate any per-event correlations. This mixed-event background can then be subtracted from a second measurement that retains the inter-particle correlations, in which case only the contributions from the correlations themselves remain as the difference. In this analysis, the particular correlation of interest is the one between the azimuthal angles of the particles in one region of the detector (the ϕ distribution) and Ψ_2 taken from another region. To break this correlation, values of ϕ are matched with Ψ_2 from different events.

In practice, in this analysis, the mixing is not done as an event-by-event procedure. Instead, two histograms, the un-rotated distribution of ϕ and the distribution of Ψ_2 are convoluted in order to generate a distribution of ϕ-Ψ_2 in which there is no elliptic flow correlation. This is then subtracted from the correlated distribution (in which ϕ-Ψ_2 is summed together event-by-event).

The difference between these histograms is the purely correlated signal. This can be fit with the function $2v_2^{obs}\cos(2(\phi-\Psi_2))$. This is nearly the same function as Eq. 4.2, only without the leading term, since the radial flow is now removed with the mixed-event background. Using the resolution determined from the subevents, the remaining step is to divide v_2^{obs} by R to find the true v_2.

Chapter 5: SpecFlow Analysis at PHOBOS

5.1: Data sets and event selection

Four data sets are used in this analysis. The Au+Au 200-GeV and Au+Au 62-GeV data sets were both taken during the 2004 RHIC physics run, and the Cu+Cu 200-GeV and Cu+Cu 62-GeV data sets were both taken during the 2005 RHIC physics run.

The data sets are further divided into PHOBOS runs, which correspond to data collected over perhaps an hour or two within a single RHIC store. Anomalous data were rejected to generate a list of "good" runs for each data set. The data was also divided into different beam orbit regions, delineated by jumps in the average *xy* vertex position.

The events were chosen based on the standard PHOBOS event selection, with the exception that the *z* vertex range was chosen to be -8 to +10 cm rather than -10 to +10 cm. The number of events used in the analysis of each collision system is shown in Table 5.1. For the two Au+Au data sets, the vertex was found using RMSSelVertex for the top 35% centrality and OneTrackVertex and OctMultProb for more peripheral data. In the Cu+Cu data sets, OneTrackVertex and OctMultProb were used exclusively.

Table 5.1: The Number of Events Used in the Analysis of Each Collision System

Collision system	Number of events used	Centrality Range
Au+Au 200 GeV	30,749,078	top 70% central
Au+Au 62 GeV	4,669,771	top 60% central
Cu+Cu 200 GeV	67,443,249	top 50% central
Cu+Cu 62 GeV	20,981,152	top 40% central

5.2: Detector elements used in the measurement

In this analysis, Ψ_2 is determined event-by-event using hits in the octagon and the ring detectors. The azimuthal distribution of particles in each event (the distribution of ϕ) is found using tracks in the two spectrometer arms. These arms each have a very narrow azimuthal acceptance, meaning that in a single event, only a narrow slice of the ϕ distribution is measured. However, the reaction plane changes event-by-event, and therefore the ϕ-Ψ_2 distribution can be built up as a composite over many events.

In order to remove non-flow correlations, a pseudorapidity gap is maintained between the particles in the Ψ_2 determination and those particles that form the ϕ distribution. Since the spectrometer arms measure particles near midrapidity, this means that only the ends of the octagon, rather than its full length, should be used to find Ψ_2. A schematic of this arrangement is shown in Fig. 5.1. The subevents are chosen to be equally sized, opposite regions of pseudorapidity. This means that Ψ_{2A} is found using the positive rings and positive portion of the octagon, while Ψ_{2B} is found using the negative rings and negative portion of the octagon.

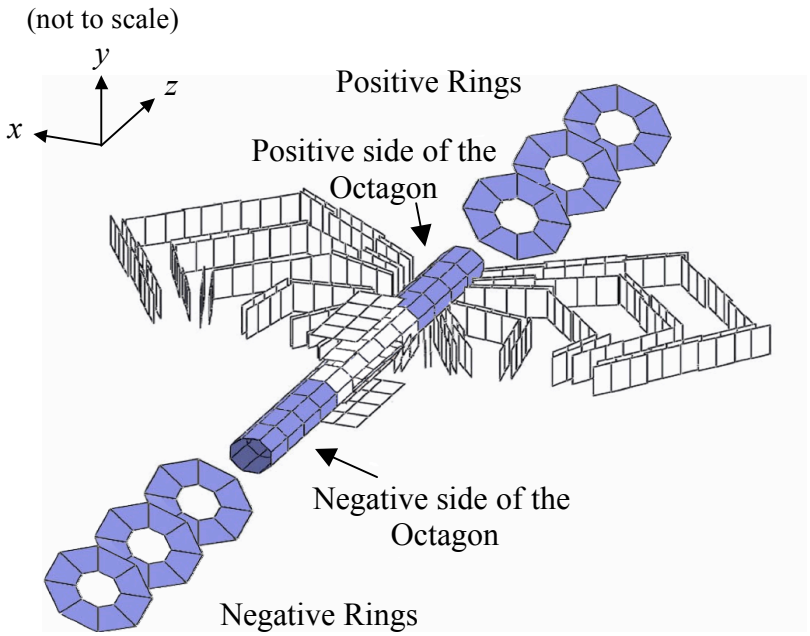

Figure 5.1: A cartoon schematic (not to scale) of the PHOBOS silicon detectors. The shaded regions of the detector were used for the Ψ_2 determination.

The regions of the octagon that are used for the Ψ_2 determination are chosen to avoid the holes near the mid-span that open to the spectrometer and vertex detectors. For a certain *z* vertex position, the two regions are found that provide the largest coverage in pseudorapidity, while being of equal size. An example illustration is provided in Fig. 5.2. Together, the two regions of the octagon that are used are referred to as the *symmetric octagon*, and these regions change in size from event to event.

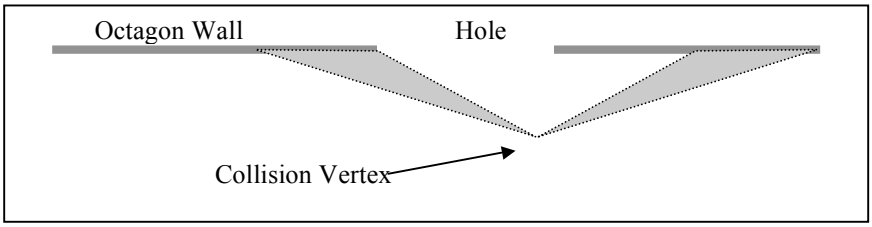

Figure 5.2: A cartoon illustrating the largest angular span covered by the octagon detector while maintaining equal regions of pseudorapidity. The size of the region is largely dependent on the *z* vertex position. It is constrained by the edges of the octagon and the holes leading to the spectrometer and vertex detectors.

Based on these constraints, the angle subtended by the symmetric octagon changes significantly over the possible *z* vertex positions. In contrast, the rings are relatively far away from the interaction region, and the angles that they subtend depend very little on the *z* vertex position. The acceptance in pseudorapidity as a function of vertex position is provided for both of these types of detectors in Fig 5.3.

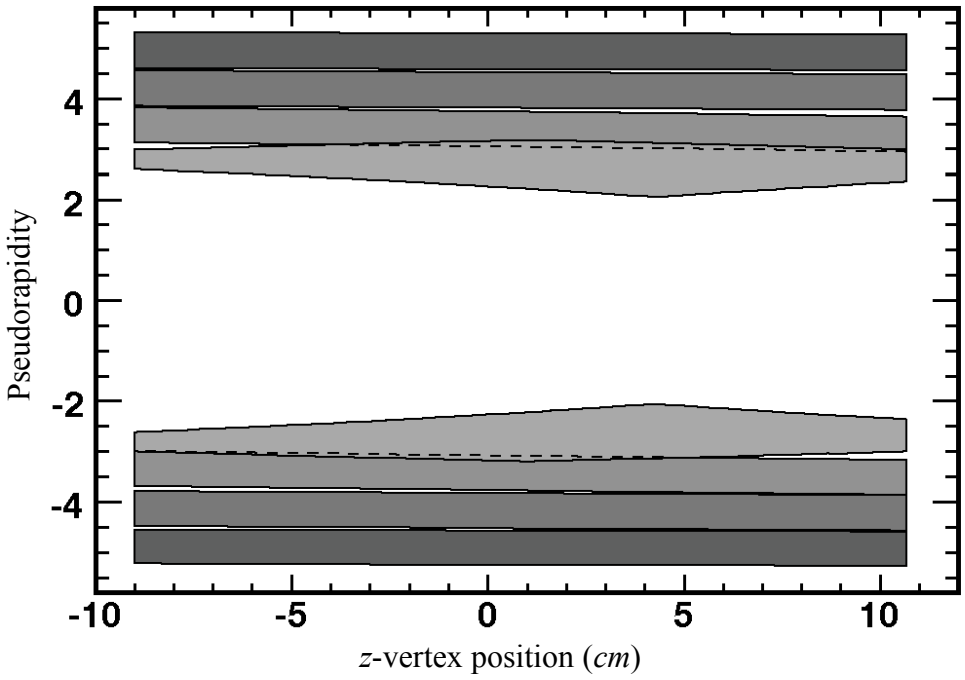

Figure 5.3: The pseudorapidity coverage of the symmetric octagon (innermost region) and the rings (outermost three regions) as a function of *z* vertex position. The dashed lines show the extent to which the angular acceptance of the innermost ring overlaps with the acceptance of the octagon.

5.3: Generating a weight map

Taken over many events, the reaction plane has no particular orientation relative to the laboratory, and, therefore, the average particle distribution will be azimuthally isotropic. However, realistically, a measurement of the average distribution made with an imperfect detector will have inherent azimuthal non-uniformities. Recall that the equations for the flow vector components Q_{2x} and Q_{2y} (Eq. 4.3 and 4.4) include a coefficient w_i for each of the i particles in an event. In this analysis, the coefficient provides a mechanism to correct for any azimuthal non-uniformities of the detector. Moving azimuthally around a narrow annulus in pseudorapidity, the average particle density can be measured, and particles in apparently denser regions are assigned smaller weights, while particles in sparser regions are given more weight.

At PHOBOS, the pixels of the octagon and ring detectors form the basis of a sort of grid in (η,ϕ). The octagon is divided along the z axis into 390 rows with azimuthal divisions into 32 columns. Similarly, the three rings on either side of the experiment each have 8 rows, roughly equally spaced in pseudorapidity, and they are divided azimuthally into 64 columns. In practice, it is the hits on this grid that are used to define Ψ_2. Therefore, instead of a weighting coefficient for the i^{th} particle, the weight is instead associated with the pixel that the particle passes through.

From the nominal vertex position (0,0,0), each of the pixels in a given row resides at roughly the same value of η. That value will change depending on the z vertex position, but, whatever the value, it will still be shared among all of the pixels in the row. Since each row essentially forms a small annulus in pseudorapidity, the pixels at each azimuthal position should be struck, on average, with equal frequency. If this is not the

case, a weight coefficient is used to correct the average deviation (*e.g.* a pixel struck 10% more frequently than the mean of the row is weighted as $w_{pixel} = 1.1^{-1}$).

The average, per-event frequency of hits in the pixels of the octagon and ring detectors is shown in Fig 5.4.

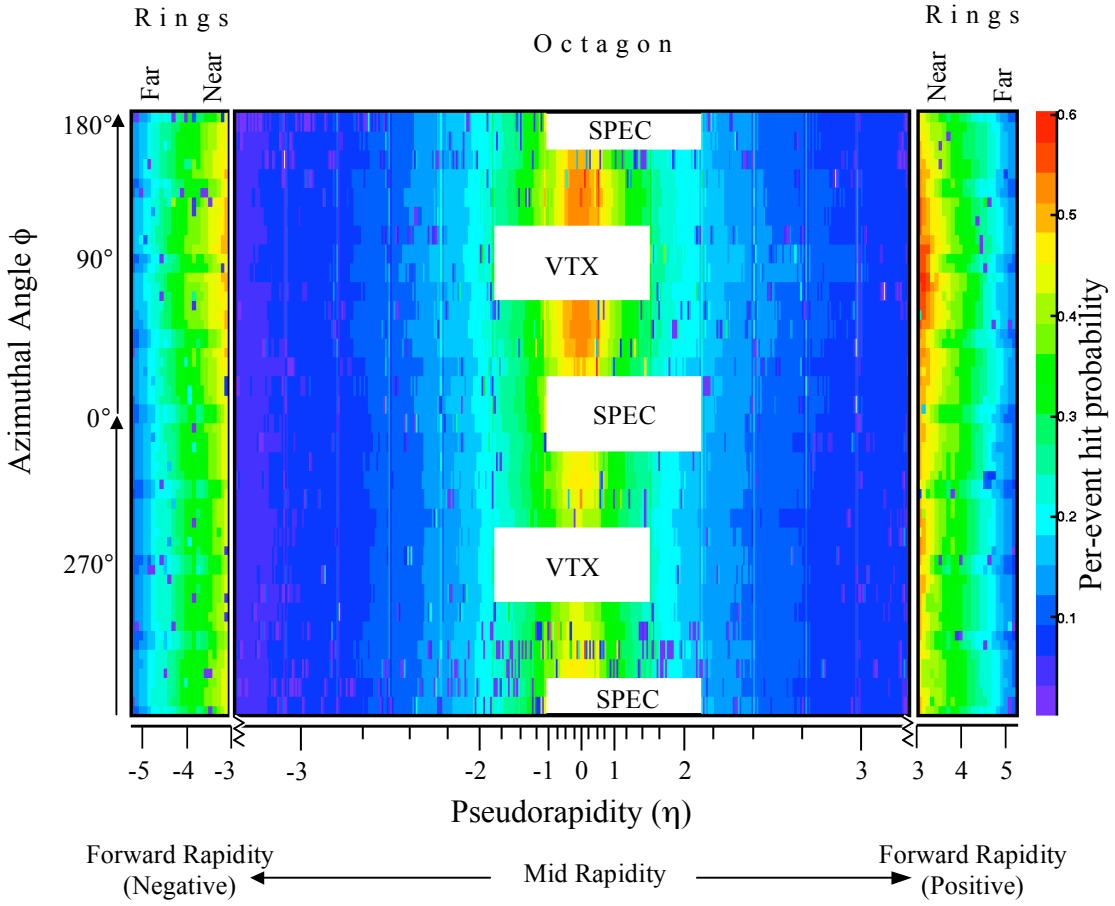

Figure 5.4: The per-event probability of hits in the octagon and ring detectors. The flanking ring arrays are concatenated in this figure. This figure represents a subset of the of the Au+Au 200-GeV data set, for a period of running with a constant beam orbit (*xy* position). These are events in the 10-15% centrality bin, having a *z* vertex between 0 and 2 cm. The pseudorapidity scale is based on a *z* vertex position of +1 cm.

Pixels that deviate too greatly from the others in the row (more than a factor of 2) are not used in the analysis. The resulting matrix of weighting coefficients is shown in Fig. 5.5.

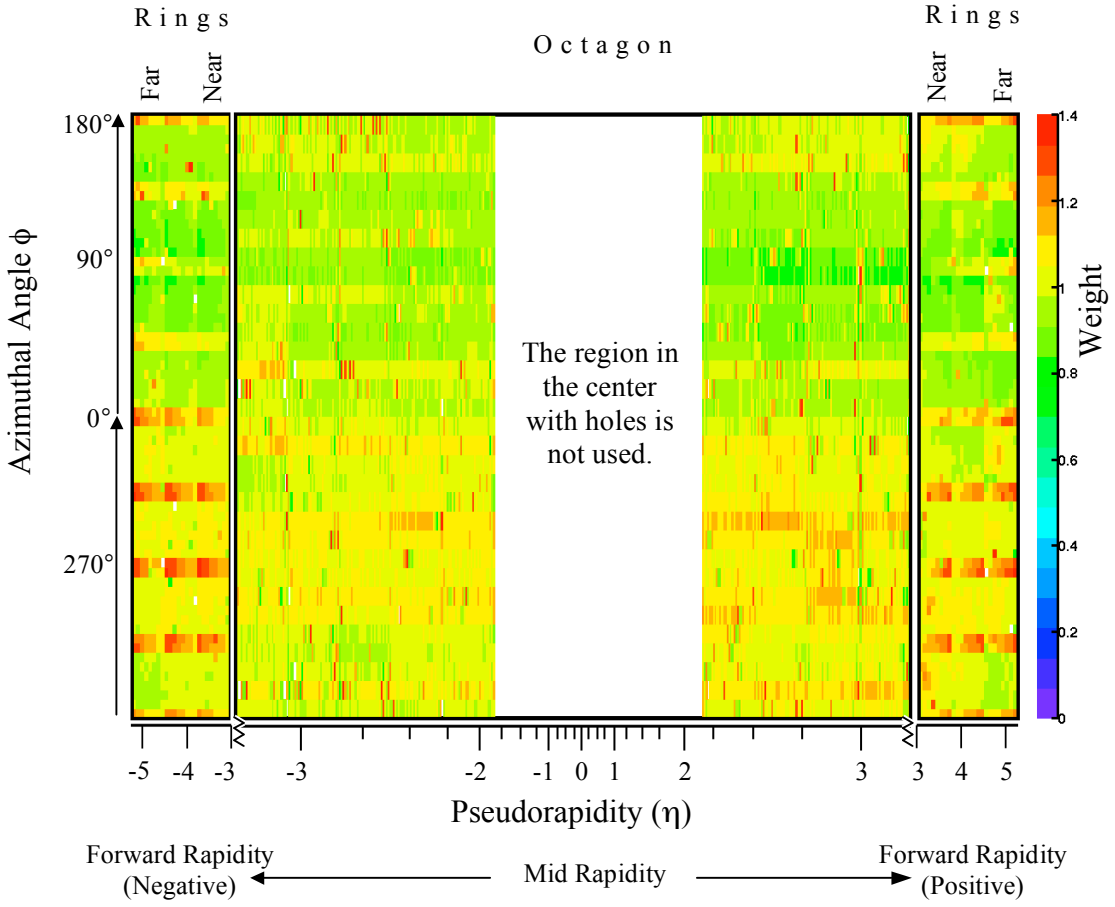

Figure 5.5: The weighting coefficient w_i for each pixel in the octagon and rings. This is derived from the same data as Fig. 5.4.

This sort of weight map is generated for 2-cm z vertex bins over the range of -8 to +10 cm, and also for several centrality bins. Most importantly, a new weight map is produced for each shift in the beam orbit, since even the few-mm deviations from the nominal xy position affects the apparent azimuthal distribution (*i.e.* as it is viewed by the octagon and rings).

5.4: Occupancy correction

This analysis uses a so-called "digital" algorithm to find Ψ_2. This means that the hits in the octagon and rings must pass a threshold energy (50 *k*eV) to be used, but otherwise, the energy information is discarded. This treatment is less complicated than an "analog" method, but it means that there is no immediate way to determine whether or not multiple particles have passed through a single pixel.

Instead, an occupancy correction using Poisson statistics is applied event by event to the struck pixels based on the local hit density within a narrow slice of pseudorapidity. From the number of occupied pixels N_{occ} and unoccupied pixels N_{unocc} in a narrow region of pseudorapidity, the Poisson average μ is given in Eq. 5.1

$$\mu = \ln\left(1 + \frac{N_{occ}}{N_{unocc}}\right) \quad , \tag{5.1}$$

and the average occupancy (*i.e.* the average number of particles represented by each struck pixel) is given in Eq. 5.2

$$Occ(\eta) = \frac{\mu}{1 - e^{-\mu}} \quad . \tag{5.2}$$

The argument η is meant to emphasize that the correction changes for the different slices of pseudorapidity.

5.5: Event plane calculation

With the inclusion of the occupancy correction, Ψ_2, Ψ_{2A}, and Ψ_{2B} are determined over their respective detector regions using Eq. 5.3

$$\Psi_2 = \frac{1}{2}\left(\tan^{-1}\frac{\sum_{pixel} w_{pixel}\cdot Occ(\eta)\cdot\sin(2\phi_{pixel})}{\sum_{pixel} w_{pixel}\cdot Occ(\eta)\cdot\cos(2\phi_{pixel})}\right) \quad . \tag{5.3}$$

This is essentially the same as Eq. 4.4, but now, rather than summing over each particle, each of the pixels that is hit is used in the sum instead. The azimuthal angle ϕ_{pixel} is randomly chosen within the dimensions of the pixel. Each term in the sum is multiplied by the occupancy correction and the weight taken from the weight map corresponding to that beam orbit, *z* vertex, and centrality bin.

5.6: Event plane distributions

The distribution of Ψ_2 should be flat since the reaction plane orientation is random. Therefore, any deviation reflects an overall bias in the Ψ_2 measurement process. In this analysis, there is some small deviation (on the order of a few percent) that is not corrected by the weight map. An example Ψ_2 distribution is shown in Fig 5.6.

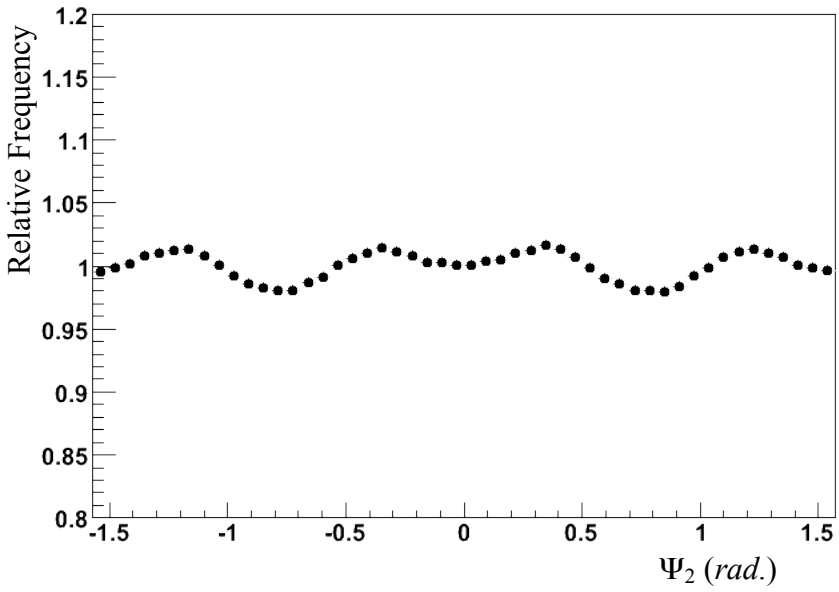

Figure 5.6: The reaction plane distribution for the Cu+Cu 200-GeV data set.

This minor deviation does not affect the final result because it is removed during the subsequent mixed-event background subtraction. (This assertion was tested by further flattening the Ψ_2 distribution using the angle shifting procedure described in [Bar97]. The additional measure was found to have a negligible effect, and it was not used in the final analysis.)

5.7: The event plane resolution

The resolution, found using the subevent procedure, is given in Table 5.1 for each collision system for each of the centrality bins used in this analysis. For all of these values, the fractional uncertainty (statistical) is less than 0.5%.

Table 5.2: The Resolution of Each Collision System for Each of the Centrality Bins

Centrality bin	Resolution for each collision system			
	Au+Au 200 GeV	Au+Au 62 GeV	Cu+Cu 200 GeV	Cu+Cu 62 GeV
0-3%	0.269	0.167	0.223	0.109
3-6%	0.362	0.228	0.240	0.123
6-10%	0.457	0.276	0.260	0.138
10-15%	0.533	0.332	0.272	0.148
15-20%	0.578	0.369	0.281	0.153
20-25%	0.593	0.367	0.279	0.154
25-30%	0.589	0.368	0.268	0.148
30-35%	0.567	0.343	0.250	0.135
35-40%	0.529	0.311	0.229	0.128
40-45%	0.483	0.278	0.204	
45-50%	0.430	0.238	0.181	
50-55%	0.368	0.182		
55-60%	0.301	0.148		
60-65%	0.239			
65-70%	0.181			

The resolution, which can be thought of as a measure of agreement between Ψ_{2A} and Ψ_{2B}, changes with the centrality for two chief reasons. First, as the centrality increases, the multiplicity increases. With the greater statistics, increasingly accurate measurements of Ψ_R are made in the subevent regions, and they tend to agree better. However, at some point, this trend of increasing resolution with increasing centrality breaks because of a second factor working in opposition to the first. For increasingly central collisions, the initial eccentricity decreases, causing a corresponding decrease in the elliptic flow signal. Therefore, though the statistics are greatest for the most central collisions (*i.e.* the 0-3% bin), the flow signal is weakest, and the subevents will not agree particularly well in their respective estimates of Ψ_R.

The resolution also changes as a function of z vertex position because the size of the symmetric octagon changes. In this analysis, the resolution is taken as an average over the entire vertex range. This is used to correct v_2^{obs}, which itself is an average over the same vertex range, derived from the same events. There is, in practice, very little difference in the results whether or not the data is divided into vertex bins to account for the variation of the resolution.

5.8: Track selection

In an integrated flow measurement, there are no delineations made among particles within an event, and all particles within a certain detector region are collectively used to establish $dN/d(\phi-\Psi_R)$. In this analysis, straight tracks are used for the integrated v_2 measurement because there are more of them than there are curved tracks. Table 5.2 shows the average number of curved and straight tracks per event for each collision system for the top 50% centrality (top 40% for Cu+Cu 62 GeV).

Table 5.3: The Average Number of Straight and Curved Tracks Per Event

Collision system	Average number of straight tracks	Average number of curved tracks
Au+Au 200 GeV	17.4	5.6
Au+Au 62 GeV	13.6	4.0
Cu+Cu 200 GeV	6.0	1.7
Cu+Cu 62 GeV	4.8	1.3

For the differential v_2 measurements, curved tracks are used because they carry additional information with which the particles can be categorized. The curved tracks are binned according to their transverse momentum p_T, and they are also categorized according to species. The exact partitioning of the data is shown in Appendix E. Straight

tracks are restricted in pseudorapidity from $0<\eta<1$, and curved tracks are limited from $0<\eta<1.6$ (this is also illustrated in Appendix E).

The tracks used in this analysis were required to have a distance of closest approach (DCA) of less than 0.35 cm from the collision vertex. The curved tracks were additionally required to have a fit probability greater than 0.05. (These standard selection criteria are described further in [Val04].)

5.9: Correlation of tracks to the event plane

The non-uniformity of the distribution of tracks in the spectrometer is evident from Fig. 5.7. This is the result of poor vertical spatial resolution in the spectrometer. Some of the spectrometer pixels are 19 mm high while, in comparison, they are only 0.67 mm wide. This form follows the intended function, which is to observe the bending of particles by the magnet in the horizontal plane. However, particles near $\phi=0$ or π rad are not well reconstructed because their position cannot be determined within the pixel, and adding more pixels in-line does not help much. This is cause of the peak in panel (b) of Fig. 5.7. Since the spectrometer arms are separated by π radians and elliptical flow is π-periodic, the tracks from the two arms are rotated so that they overlap.

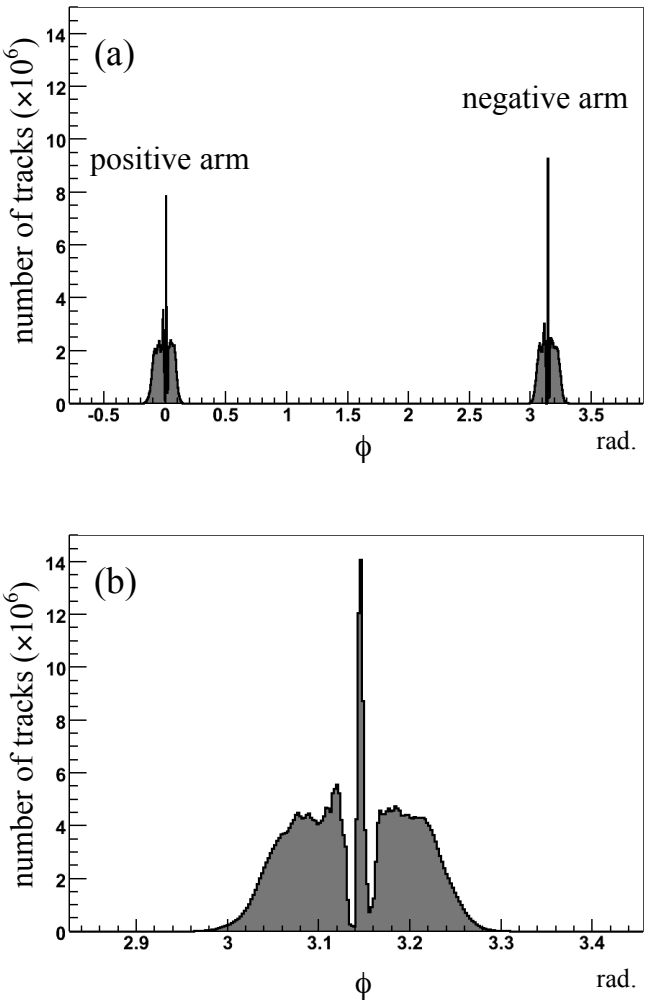

Figure 5.7: Panel (a) shows the azimuthal distribution of straight tracks in the two spectrometer arms for the entire Cu+Cu 200-GeV data set. Panel (b) is the sum of both arms, with the positive arm shifted to overlap with the negative arm.

Event-by-event, the tracks are shifted relative to the event plane to build a complete distribution of ϕ-Ψ_2. The expectation is that there will be an excess of tracks when the spectrometer aligns with the reaction plane (ϕ-$\Psi_2 \approx \pi$) and a deficit when there is an anti-alignment (ϕ-$\Psi_2 \approx (1\pm½)\cdot\pi$), yet this is not immediately evident in the data. An example ϕ-Ψ_2 distribution is presented in Fig. 5.8. The unusual shape of the distribution comes in part as a consequence of the non-uniformity of the Ψ_2 distribution, and this can be seen by comparison to Fig. 5.6.

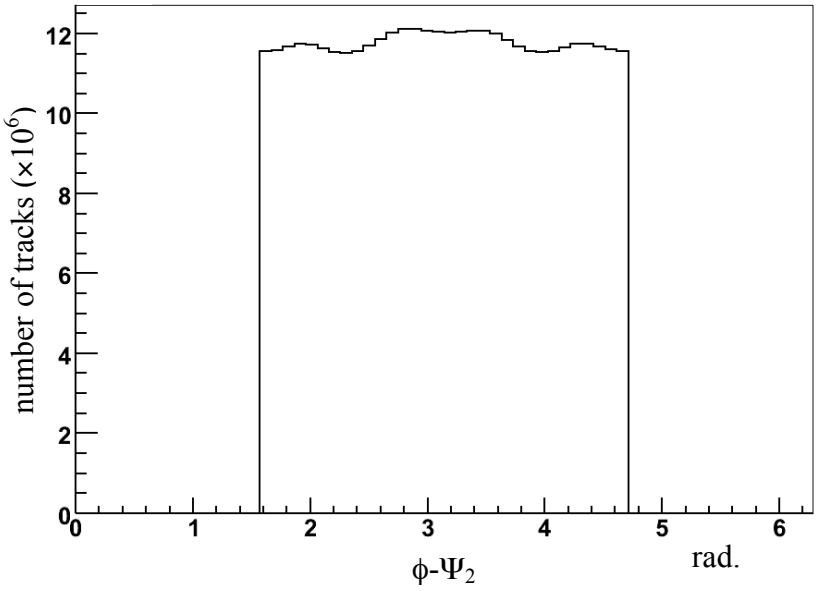

Figure 5.8: The raw azimuthal distribution of straight tracks for the Cu+Cu 200-GeV data set, shifted event-by-event relative to the event plane.

The mixed event background is generated through a convolution of the average track distribution (Fig. 5.7, panel b) with the reaction plane distribution (Fig. 5.6). The product of this convolution is the distribution that would be formed if the spectrometer arms, instead of measuring the varying number of tracks as they depend on Ψ_R, rather measured a static distribution (*i.e.* the average ϕ distribution) in each event. On the whole, the same number of tracks is used, and the tracks are shifted relative to the same average Ψ_2 distribution, but the event-by-event correlation between ϕ and Ψ_R (or Ψ_2) is broken. An example of the mixed event background is shown in Fig. 5.9 as an overlay with the correlated distribution from Fig. 5.8.

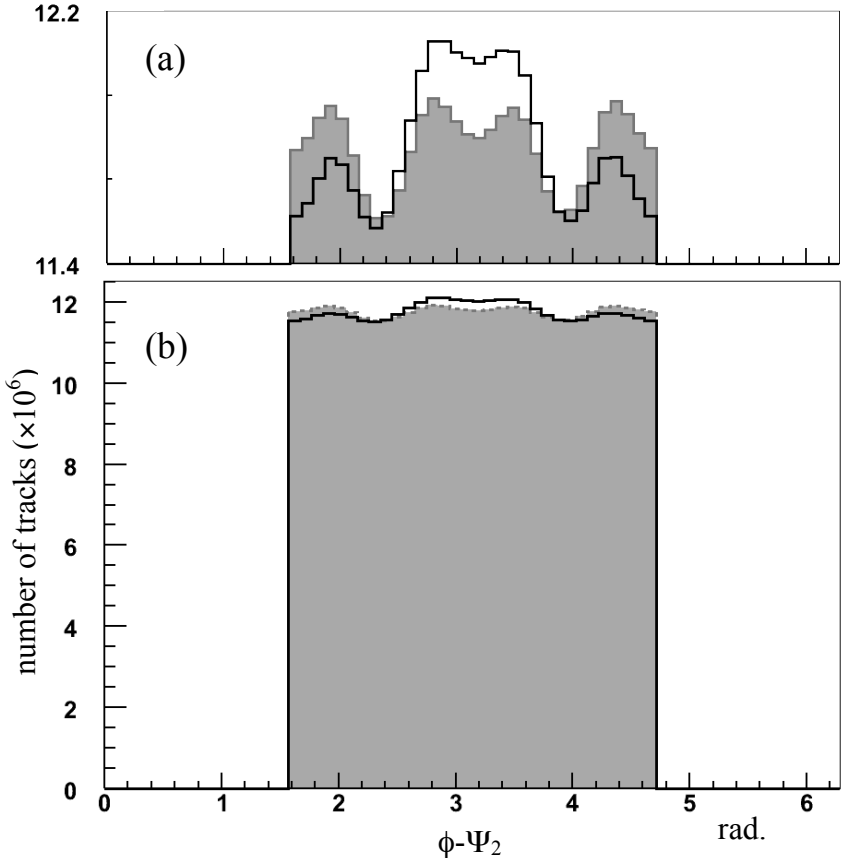

Figure 5.9: Correlated track distribution (black line) compared to the mixed event background (shaded gray) for the Cu+Cu 200-GeV data set. Panal (a) is zoomed in to show the difference between the distributions, while panel (b) shows the full scale.

The difference between the correlated track distribution and the mixed-event background is divided by the mixed-event background to find the percent difference. This represents the relative magnitude of the per-event correlation between ϕ and Ψ_2. An example is shown in Fig. 5.10.

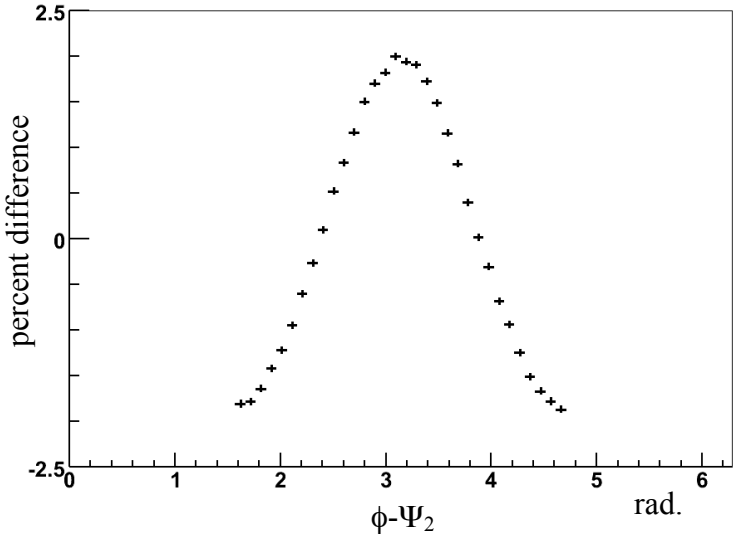

Figure 5.10: The per-event correlation between ϕ and Ψ_2 (*i.e.* the uncorrected correlation between ϕ and Ψ_R) for the Cu+Cu 200-GeV data set. The vertical error bars are statistical and the horizontal bars delineate the bin width.

The per-event correlation is fit with the formula $2 \cdot v_2^{obs} \cdot \cos(2(\phi - \Psi_2))$ to determine the magnitude and statistical uncertainty of the observed flow v_2^{obs}. (This is done using a χ^2 minimization fit with the CERN MINUIT fitting package.) All that remains is to divide by the corresponding resolution to arrive at the final value of v_2.

5.10: Elliptic flow in bins of centrality and transverse momentum

Finding the values of v_2 in a data set that is binned in centrality is a straightforward process. The events are divided up, and the previously described analysis is run in parallel on each bin. In contrast, extracting v_2 values for data binned in transverse momentum requires an extra step. In this case, the distribution of tracks is comprised of particles from the same momentum bin, but those particles do not all originate from events within the same centrality bin. The resolution changes with centrality, so the particle from one event may have a weaker correlation to the reaction plane than another particle. Therefore, the resolution value used to correct v_2^{obs} is determined as a particle-weighted average based on the resolution values of the different contributing centrality bins.

5.11: Systematic errors and cross-checks

In order to determine the systematic uncertainty in the measurement, a number of the analysis parameters are varied by reasonable amounts, one at a time, and then the deviation of the altered v_2 from the standard v_2 is tabulated. These variations are added in quadrature to establish the upper and lower bounds of the range of systematic uncertainty. This range is intended to reflect a 90% confidence level systematic error. Table 5.4 lists the parameters that were varied to arrive at the uncertainty value.

Table 5.4: Parameters Used To Evaluate Systematic Uncertainty

Variation from the Standard Analysis	Standard
Threshold for hits in the rings and octagon varied ±10 keV	50 keV
Weight maps generated for *z* vertex bins of 1 cm and 3 cm	2 cm
Negative and positive spectrometer arms analyzed separately	together
Different magnetic field polarities analyzed separately	together
Distance of closest approach (DCA) ±5 mm	35 mm
Track probability (for curved tracks only) ±0.01	0.05
Resolution determined in *z* vertex bins of 2 cm	no binning

As the parameters are varied, all of the points in a series are examined at the same time for a given data set (*e.g.* all of the centrality bins in an integrated measurement, or all of the transverse momentum bins in a differential measurement). Some variations in the v_2 are clearly distinguishable as systematic changes, for example, when all of the values in a series are collectively higher or lower than the standard result. When the errors are added in quadrature, the upper and lower bounds are calculated seperately so that these obvious asymmetric uncertainties only contribute in one direction. When yet other parameters are varied, the effect is subtler. These parameter variations may not result in a uniform deviation from the standard results, and instead the uncertainty is described in terms of point-to-point errors. To some extent, these point-to-point errors are statistical fluctuations. At the same time, there are suspected systematic effects that contribute differently to the v_2 measured in different centrality and momentum bins. In the spirit of the 90% C.L., the sources suspected of having point-to-point errors are counted along with the more obvious systematic error sources. These contribute symmetrically to both the upper and lower error limits.

In several cases, the parameter variations lead to a decrease of statistics (*e.g.* when only the tracks in one spectrometer arm or the other is used). This is not a problem for the statistically well-resolved Au+Au and Cu+Cu 200-GeV data sets. (Rather, there are problems, but these are systematic problems, and, by comparison, the statistical variation is small.) However, the limited statistics are a problem when calculating the systematic uncertainties for the Au+Au and Cu+Cu 62-GeV data sets. Rather than arrive at a systematic uncertainty value bloated with statistical contributions, it has been decided that the systematics at the lower energy are similar enough to the high-energy systematics that the latter may be applied to the former. In other words, the 62-GeV results will have the same absolute systematic uncertainties as their 200-GeV counterparts. Figures showing the individual contributions of several sources are shown in Appendix I.

Chapter 6: Results

6.1: Fundamental results

Two essential types of measurements form the basis of all of the results in this analysis:

1. The integrated v_2 is measured for different centrality bins. Here it is presented in terms of the centrality variable N_{part} for the four data sets (Au+Au 200 GeV, Au+Au 62 GeV, Cu+Cu 200 GeV, and Cu+Cu 62 GeV) in Fig. 6.1 to Fig. 6.4, respectively.
2. The differential v_2 taken with respect to transverse momentum p_T is likewise shown for the four data sets in Fig. 6.5 through Fig. 6.8. For a consistent comparison, these figures are compiled over the top 40% centrality, which is the largest centrality range that is available across all of the data sets.

Tables of all of these data are provided in Appendix G.

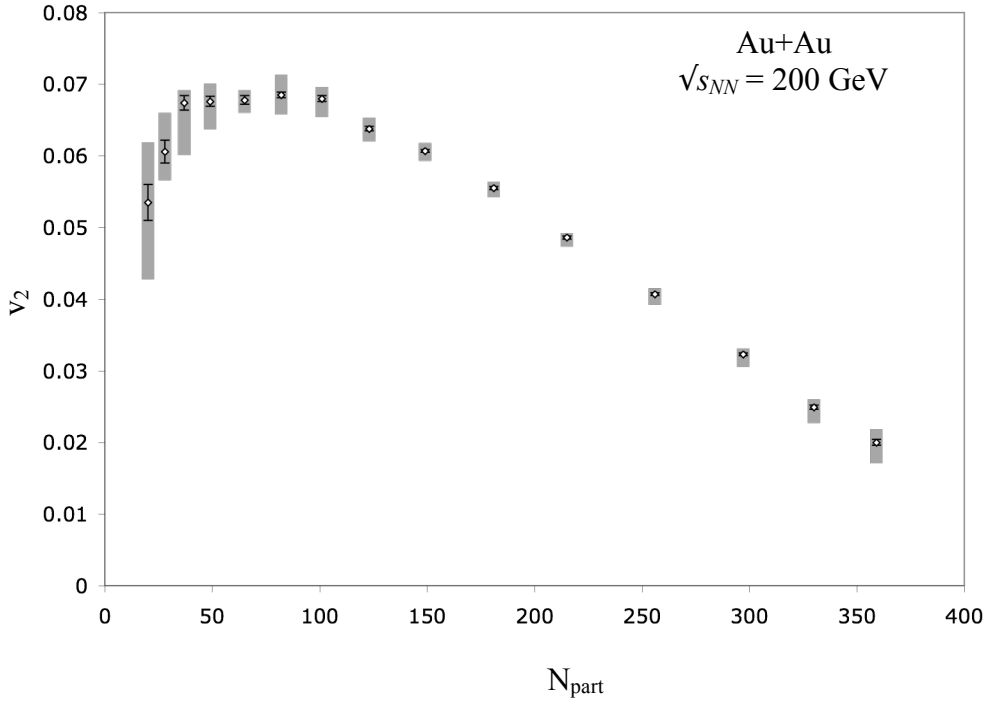

Figure 6.1: $v_2(N_{part})$ for Au+Au collisions at $\sqrt{s_{NN}}$ = 200 GeV. Black lines represent 1σ statistical errors, and gray bars indicate 90% C.L. systematic errors.

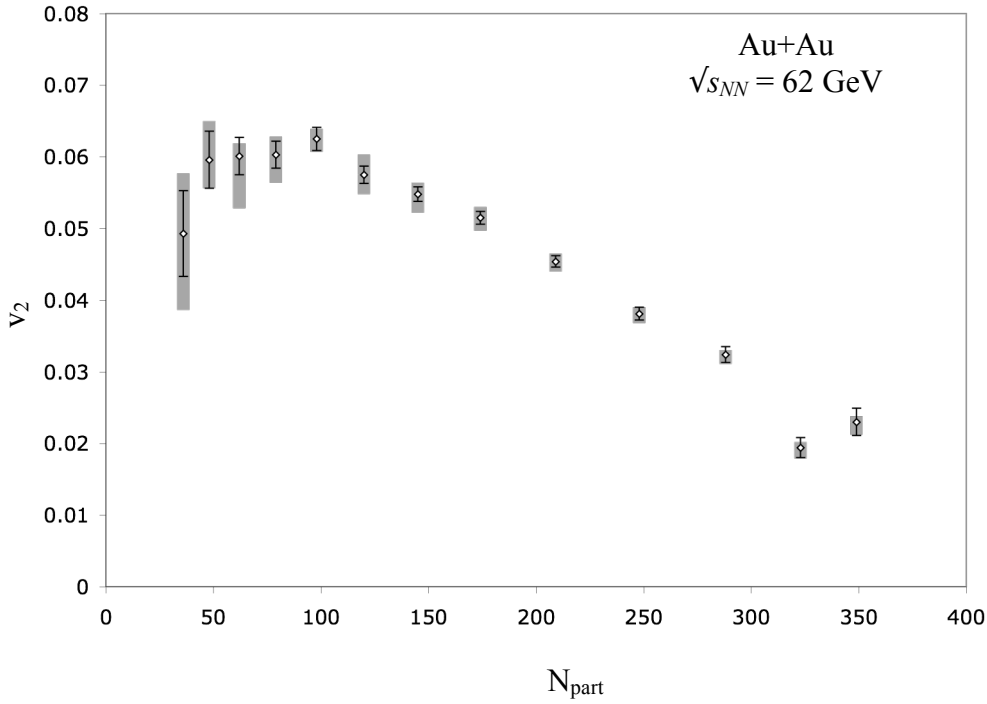

Figure 6.2: $v_2(N_{part})$ for Au+Au collisions at $\sqrt{s_{NN}}$ = 62 GeV. Black lines represent 1σ statistical errors, and gray bars indicate 90% C.L. systematic errors.

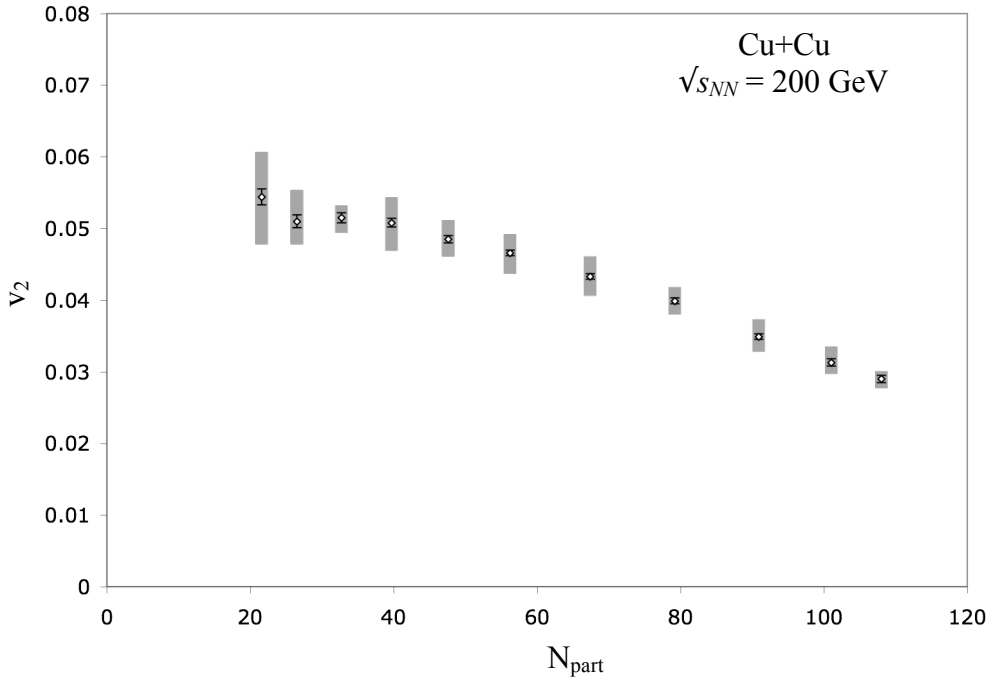

Figure 6.3: $v_2(N_{part})$ for Cu+Cu collisions at $\sqrt{s_{NN}}$ = 200 GeV. Black lines represent 1σ statistical errors, and gray bars indicate 90% C.L. systematic errors.

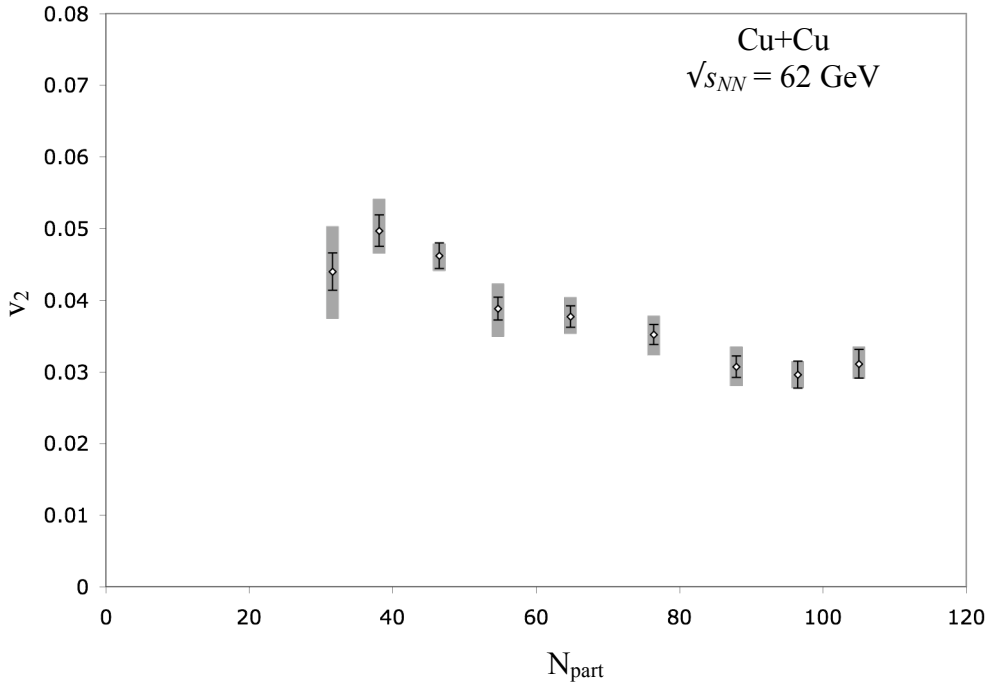

Figure 6.4: $v_2(N_{part})$ for Cu+Cu collisions at $\sqrt{s_{NN}}$ = 62 GeV. Black lines represent 1σ statistical errors, and gray bars indicate 90% C.L. systematic errors.

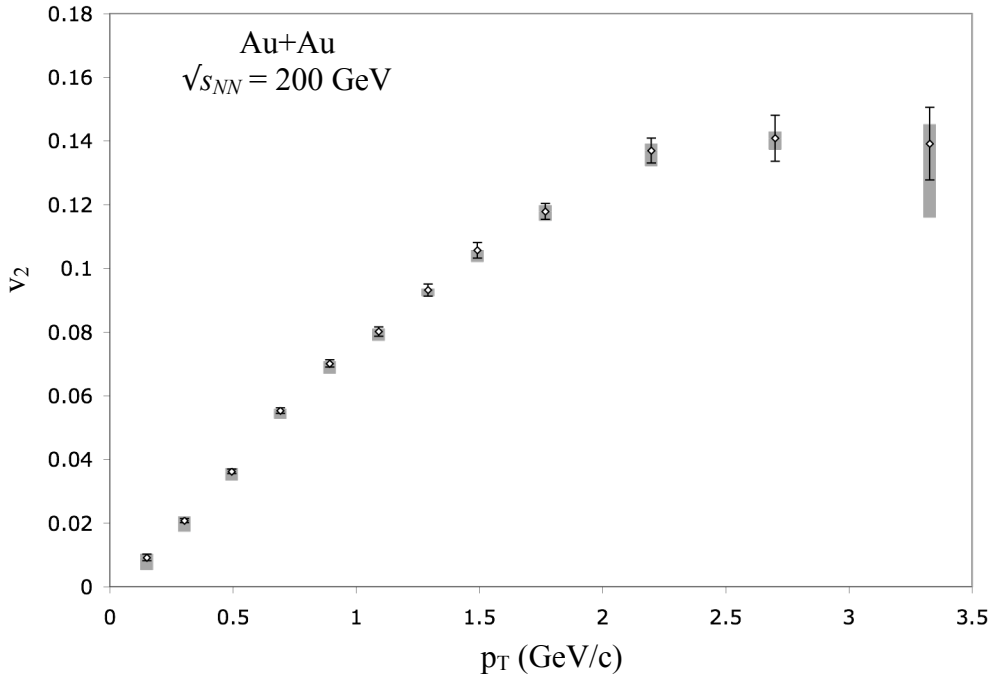

Figure 6.5: $v_2(p_T)$ for Au+Au collisions between 0-40% centrality at $\sqrt{s_{NN}}$ = 200 GeV. Black lines represent 1σ statistical errors, and gray bars indicate 90% C.L. systematic errors.

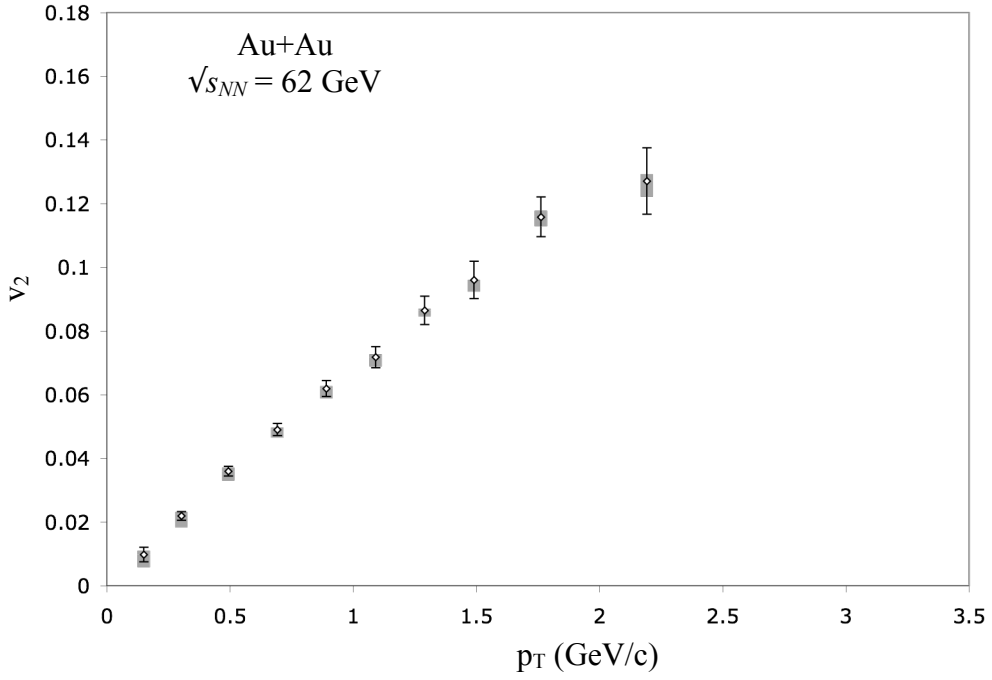

Figure 6.6: $v_2(p_T)$ for Au+Au between 0-40% centrality collisions at $\sqrt{s_{NN}}$ = 62 GeV. Black lines represent 1σ statistical errors, and gray bars indicate 90% C.L. systematic errors.

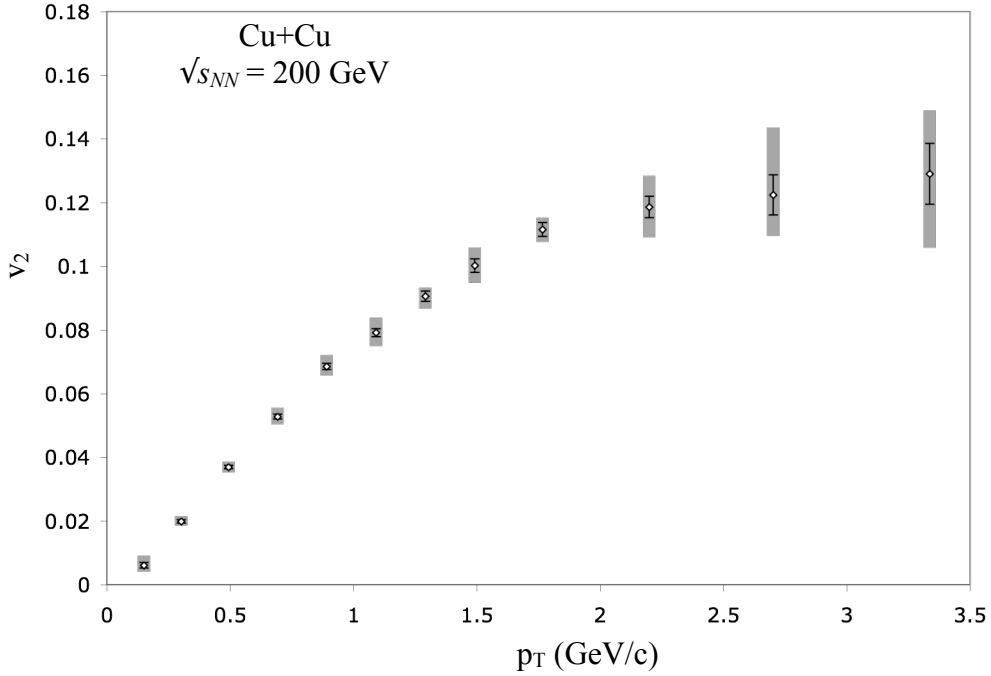

Figure 6.7: $v_2(p_T)$ for Cu+Cu collisions between 0-40% centrality at $\sqrt{s_{NN}}$ = 200 GeV. Black lines represent 1σ statistical errors, and gray bars indicate 90% C.L. systematic errors.

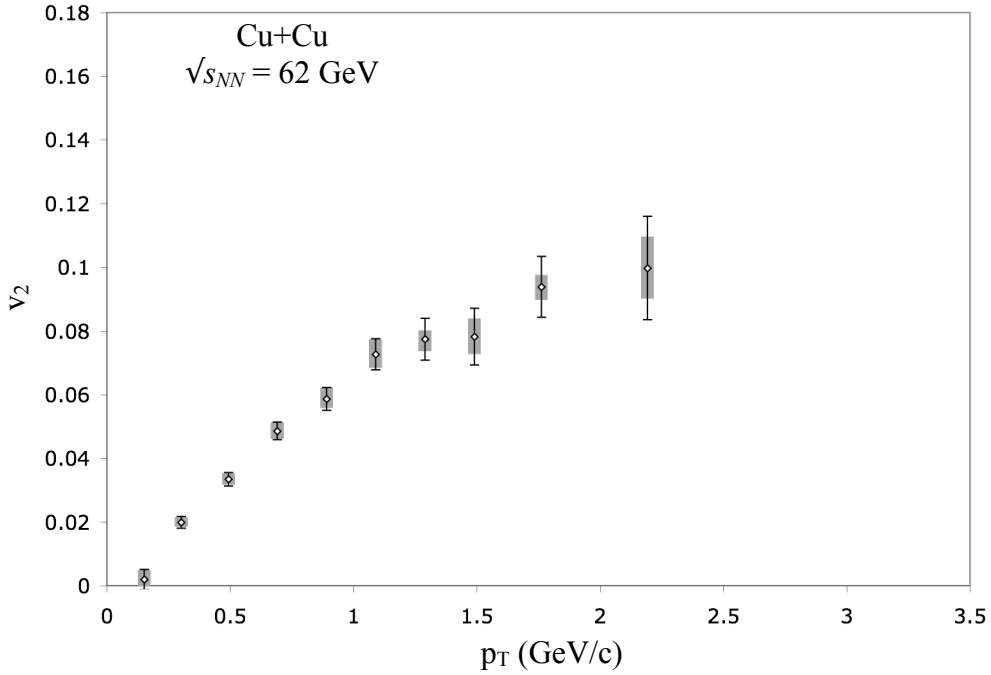

Figure 6.8: $v_2(p_T)$ for Cu+Cu collisions between 0-40% centrality at $\sqrt{s_{NN}}$ = 62 GeV. Black lines represent 1σ statistical errors, and gray bars indicate 90% C.L. systematic errors.

6.2: Trends in the integrated elliptic flow

The integrated v_2 data in Sec. 6.1 invites a few basic comparisons. For example, the energy dependence can be observed for each colliding species. This is shown for Au+Au in Fig. 6.9 and for Cu+Cu in Fig. 6.10. What is seen is that, for a constant collision geometry (*i.e.* constant size and shape of the participant region), the elliptic flow increases with system energy, although this change is not very dramatic.

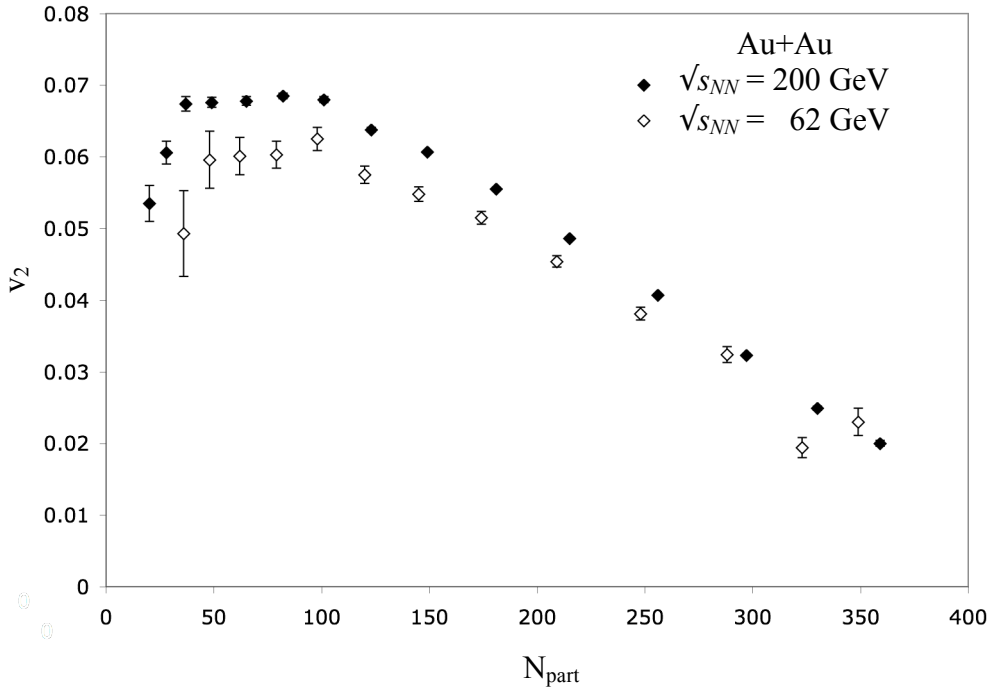

Figure 6.9: $v_2(N_{part})$ for Au+Au collisions at $\sqrt{s_{NN}}$ = 200 GeV (solid points) and at $\sqrt{s_{NN}}$ = 62 GeV (open points). The error bars are 1σ statistical errors.

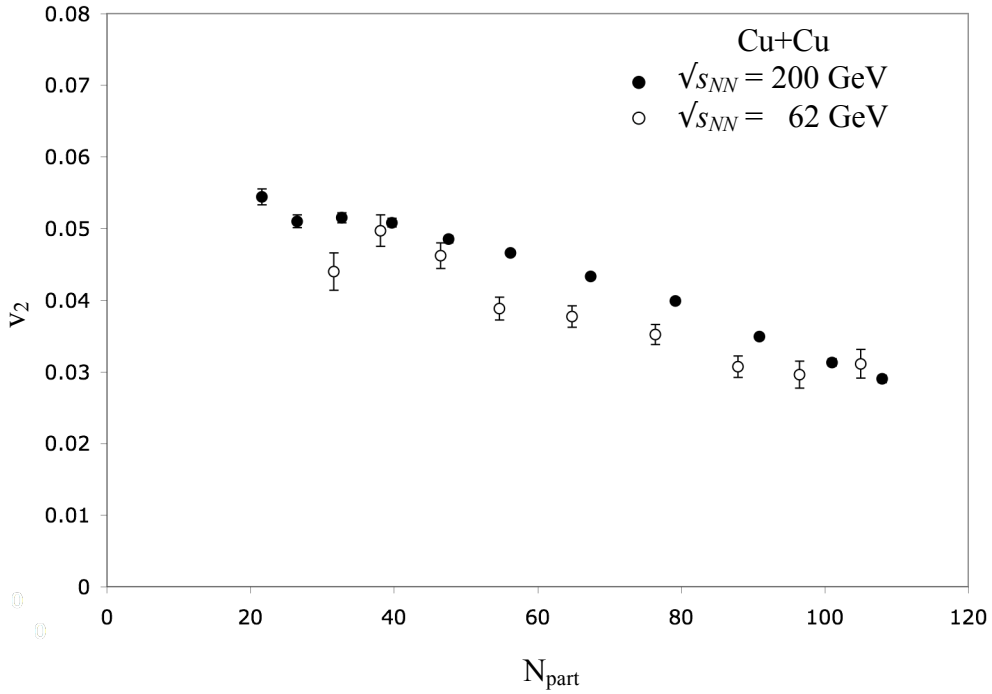

Figure 6.10: $v_2(N_{part})$ for Cu+Cu collisions at $\sqrt{s_{NN}}$ = 200 GeV (solid points) and at $\sqrt{s_{NN}}$ = 62 GeV (open points). The error bars are 1σ statistical errors.

It is also interesting to compare the elliptic flow between the Au+Au and Cu+Cu collision systems. Figure 6.11 demonstrates the relationship of $v_2(N_{part})$ for the two species at $\sqrt{s_{NN}}$ = 200 GeV. One striking aspect is that the elliptic flow is greater for the most central Cu+Cu collisions than it is for central Au+Au collisions. This was initially very surprising. It suggests that the smaller system does a better job translating the initial spatial anisotropy into collective motion than the larger system.

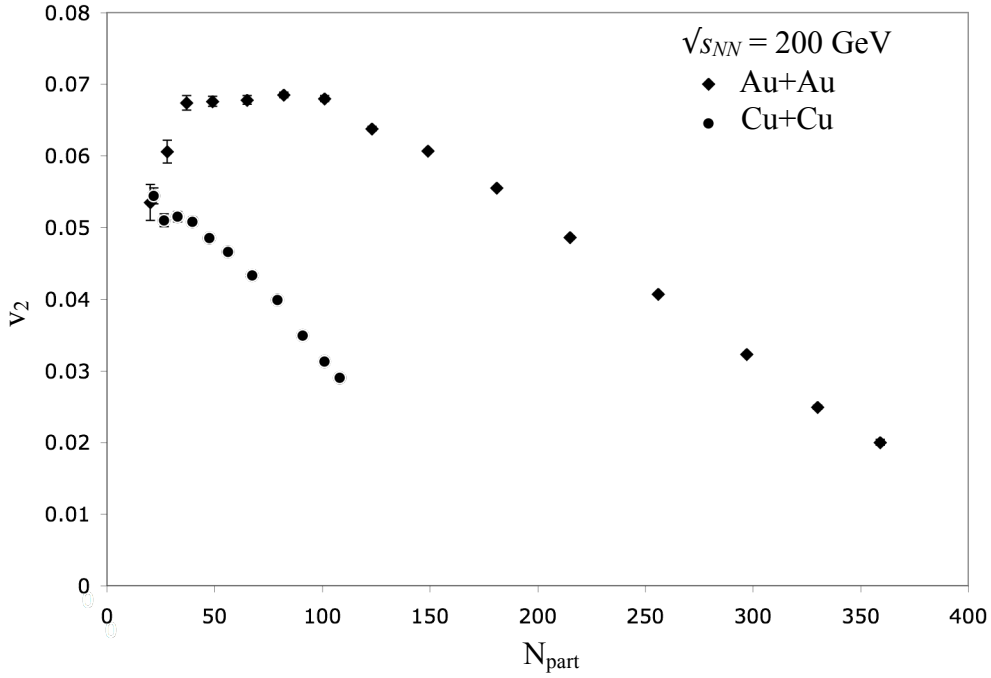

Figure 6.11: $v_2(N_{part})$ for Au+Au collisions (diamonds) and Cu+Cu collisions (circles) at $\sqrt{s_{NN}}$ = 200 GeV. The error bars are 1σ statistical errors.

To make a meaningful comparison between collision species, the initial geometry needs to be modeled, and v_2 should subsequently be divided by the eccentricity (Sec. 3.7). Figure 6.12 shows v_2/ε_{RP} with respect to N_{part} for the two 200-GeV data sets. Figure 6.13 shows the same data divided by ε_{part} instead.

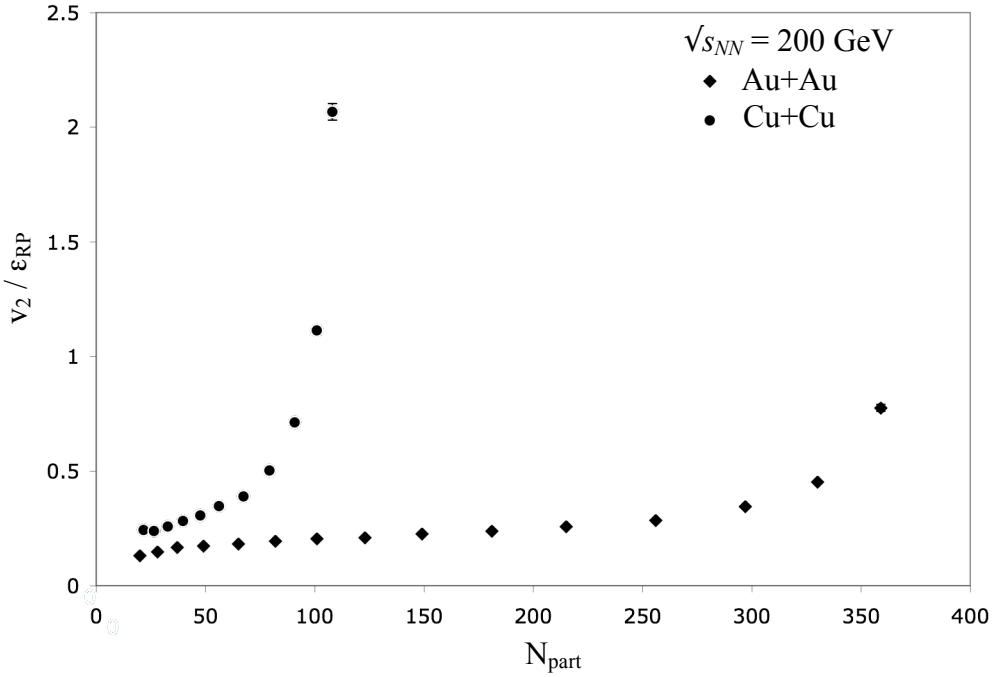

Figure 6.12: v_2/ε_{RP} with respect to N_{part} for Au+Au collisions (diamonds) and Cu+Cu collisions (circles) at $\sqrt{s_{NN}}$ = 200 GeV. The error bars are 1σ statistical errors.

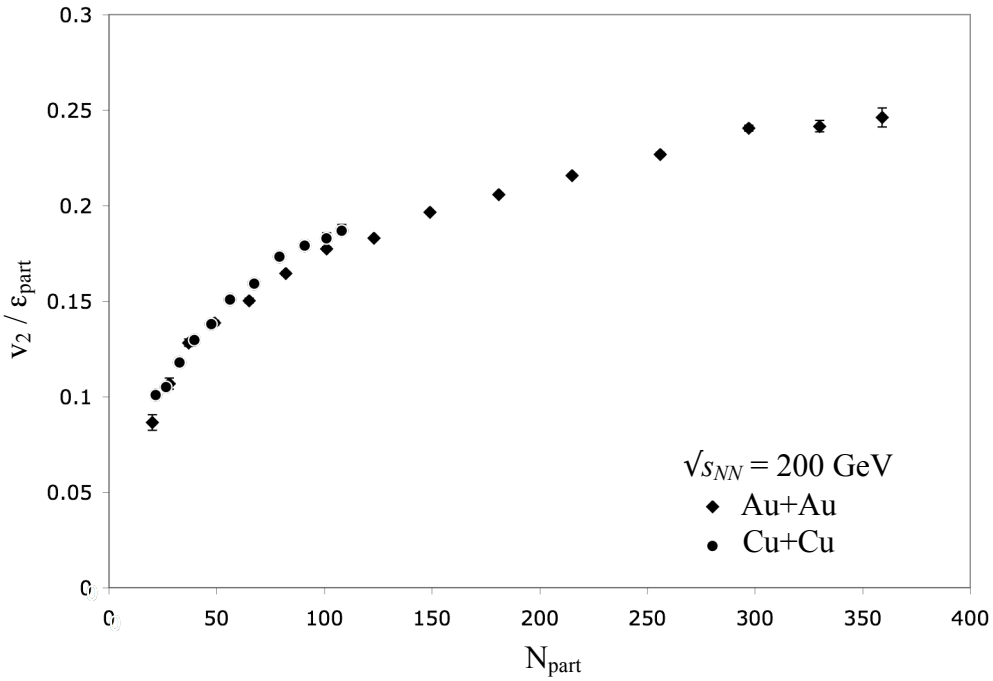

Figure 6.13: v_2/ε_{part} with respect to N_{part} for Au+Au collisions (diamonds) and Cu+Cu collisions (circles) at $\sqrt{s_{NN}}$ = 200 GeV. The error bars are 1σ statistical errors.

Unlike Fig. 6.12, Fig. 6.13 shows a relatively smooth evolution with N_{part}, with both systems falling onto the same "universal" curve. It seems likely that v_2 should depend on the eccentricity and size of the participant region, but not on the particular choice of heavy ion used in a collision. Therefore, the participant eccentricity appears to be more successful of the two interpretations of the Glauber geometry.

In Fig. 6.14, the 62-GeV data is shown alongside the 200-GeV data, both divided by ε_{part}. This figure illustrates that, although the geometry dependence is removed, the elliptic flow still depends on the energy of the collision system (as it did in Fig. 6.9 and Fig. 6.10).

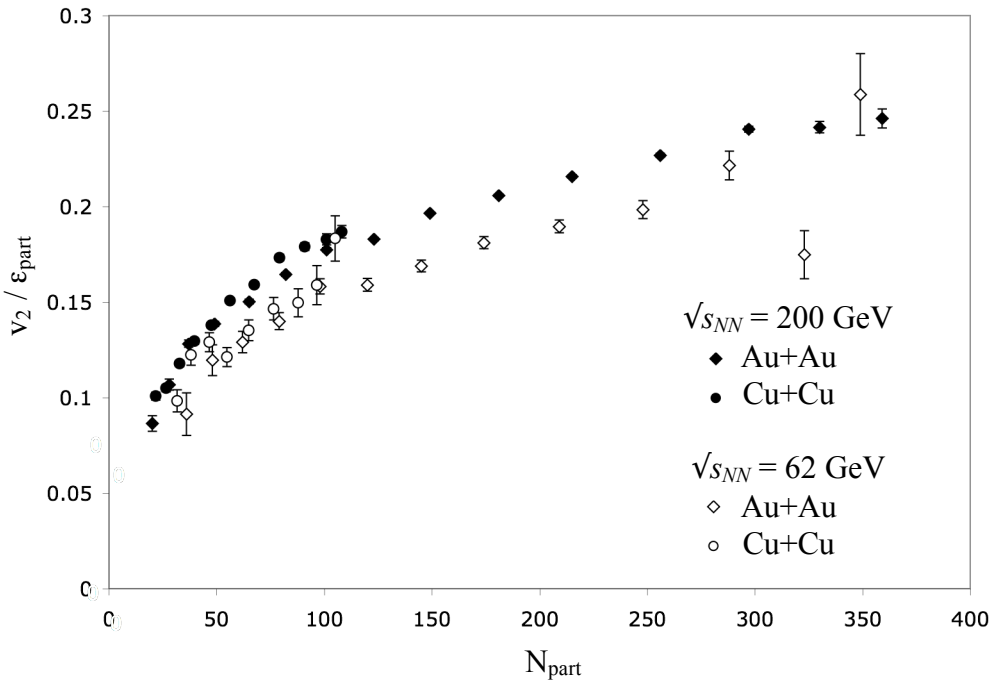

Figure 6.14: v_2/ε_{part} with respect to N_{part} for Au+Au collisions (diamonds) and Cu+Cu collisions (circles) at $\sqrt{s_{NN}}$ = 200 GeV (filled markers) and $\sqrt{s_{NN}}$ = 62 GeV (hollow markers). The error bars are 1σ statistical errors.

6.3: Elliptic flow with respect to transverse momentum

The particle-identified measurement of $v_2(p_T)$ from this analysis is shown in Fig. 6.15 for charged pions, kaons, and (anti)protons, along with similar measurements from the STAR and PHENIX experiments. A characteristic of the hydrodynamic expansion is that the elliptic flow will vary for particles of different mass (smaller flow for heavier particles). This is seen in the data in Fig. 6.15, though the mass splitting is not necessarily of the exact magnitude suggested by hydrodynamics.

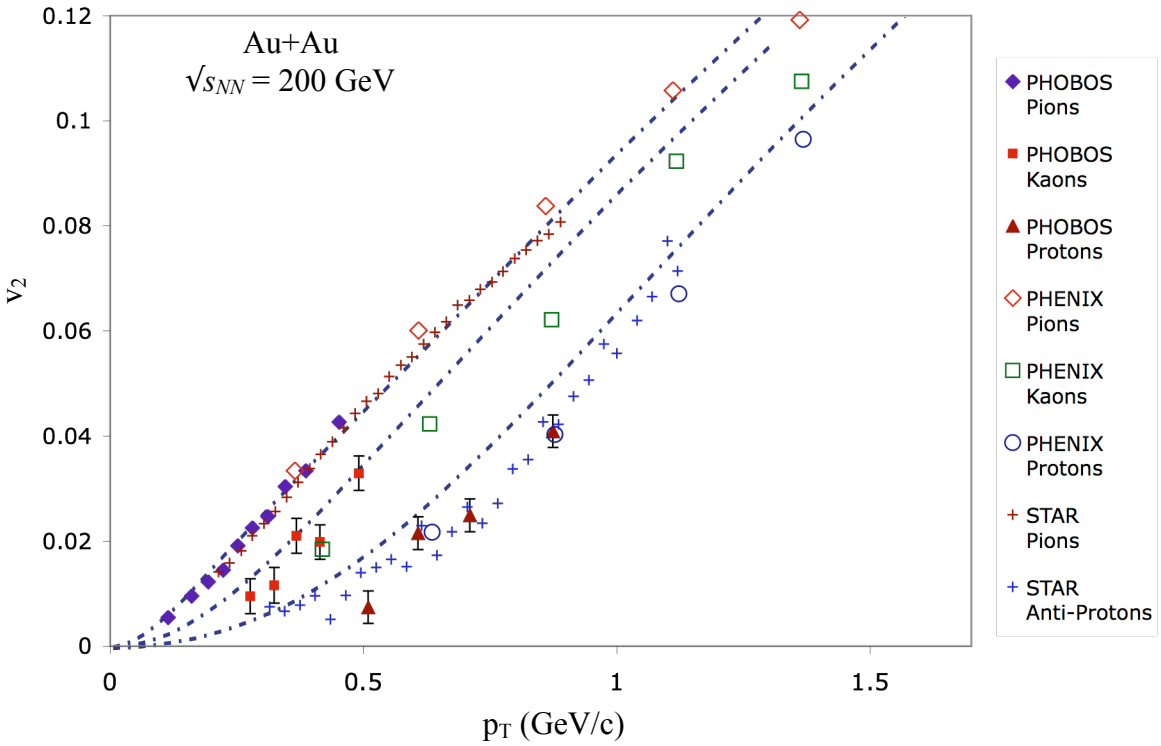

Figure 6.15: Particle identified $v_2(p_T)$ for Au+Au collisions at $\sqrt{s_{NN}}$=200 GeV. The data from this analysis (PHOBOS) was compiled over the 0-70% centrality range and a pseudorapidity range of $0 \le \eta \le 1.6$. The PHENIX data [Ad103] is from 0-70% centrality at midrapidity, and the STAR data [Ada05] is from 0-80% centrality at midrapidity. From top to bottom, the blue dot-dash lines are hydrodynamic calculations (also from [Ada05]) for pions (π^+ and π^-), kaons (K^+ and K^-), and (anti)protons (p and $\bar{p}$), respectively. Error bars are 1σ statistical errors, but they are only shown for the PHOBOS data points.

In Sec. 6.2, the great challenge was unraveling the relationship between the Au+Au v_2 and the Cu+Cu v_2 by introducing the participant eccentricity. Here, it is also useful to examine whether the agreement seen in the integrated measurement of v_2/ε extends to the differential measurement $v_2(p_T)$ as well.

Using the two 200-GeV data sets, centrality slices for Au+Au and Cu+Cu are chosen that agree in N_{part}. In other words, peripheral Au+Au collisions are compared to central Cu+Cu collisions in order to match the size of the participant system. In practice, these regions have irregular widths because they are defined using standard PHOBOS centrality bins, and these do not overlap evenly in N_{part} between collision species. For two regions, A and B, the respective centrality ranges and the average eccentricities $\langle\varepsilon_{part}\rangle$ are provided for the two collision species in Table 6.1. These regions are shown overlaid on the data in Fig. 6.16.

Table 6.1: Regions with Similar Mean N_{part}

Region A	Cu+Cu 25-50% Au+Au 50-70%	$\langle\varepsilon_{part}\rangle$=0.441 $\langle\varepsilon_{part}\rangle$=0.550
Region B	Cu+Cu 3-20% Au+Au 35-50%	$\langle\varepsilon_{part}\rangle$=0.224 $\langle\varepsilon_{part}\rangle$=0.417

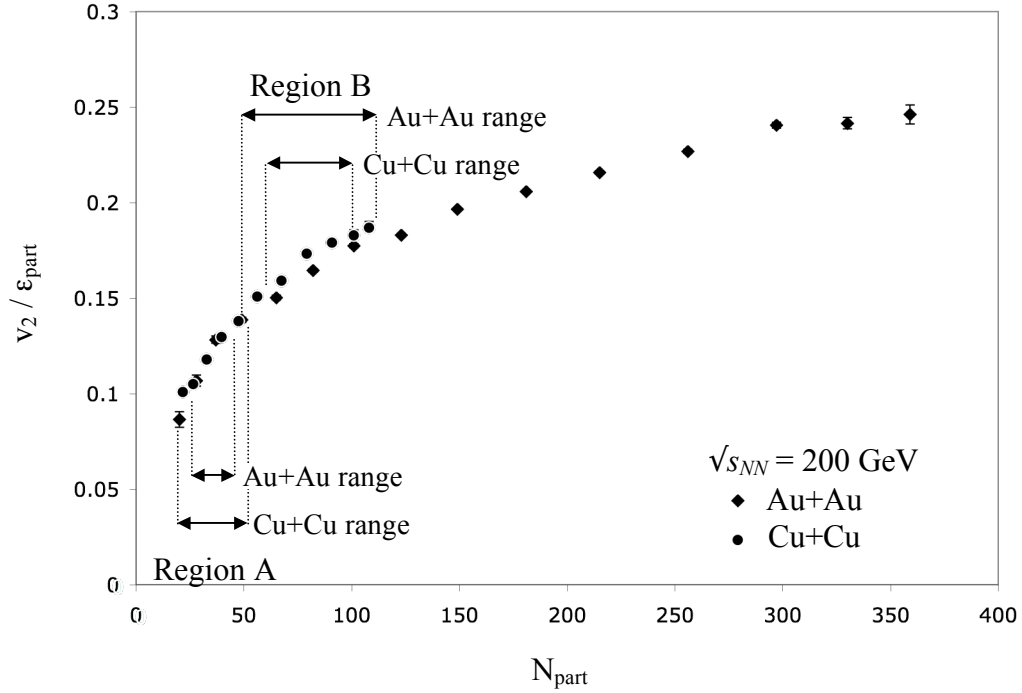

Figure 6.16: This is the same data as Fig. 6.13 with arrows to delineate the two regions with matching mean N_{part}.

Figure 6.17 and Fig 6.18 show $v_2(p_T)$ for the two collision species at $\sqrt{s_{NN}}$=200 GeV for centrality region A and B, respectively. In both cases, there is remarkably good agreement. This suggests that the overlap of v_2/ε_{part} for the two systems is not an accidental coincidence in the integrated measurement, but rather it reflects an equivalence between the collisions that extends to the transverse momentum dimension as well.

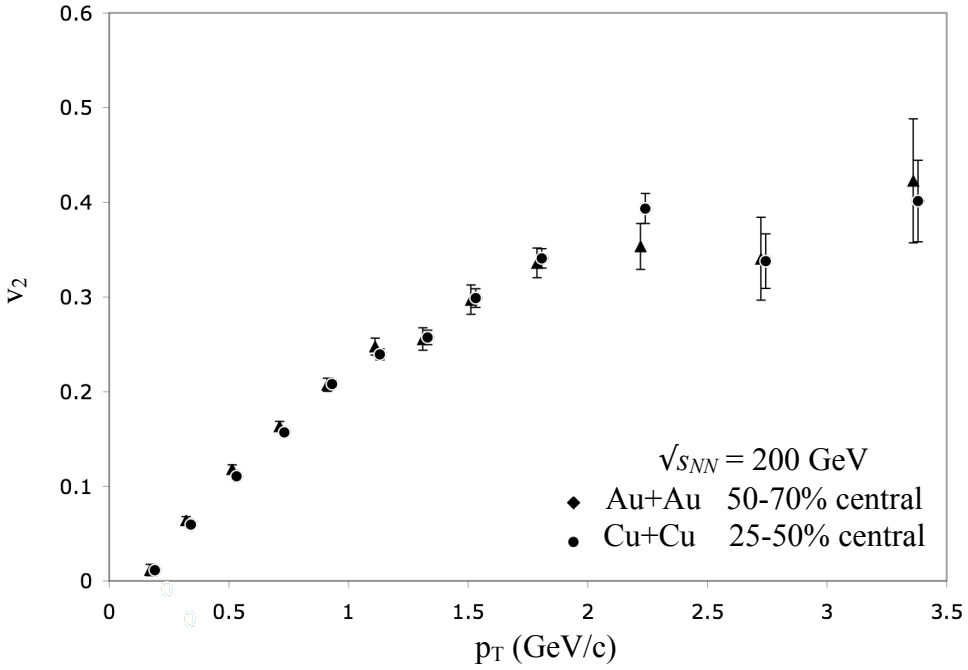

Figure 6.17: $v_2(p_T)$ for the 200-GeV data for Au+Au (diamonds) from 50-70% centrality and Cu+Cu (circles) from 25-50% centrality. The error bars are 1σ statistical errors.

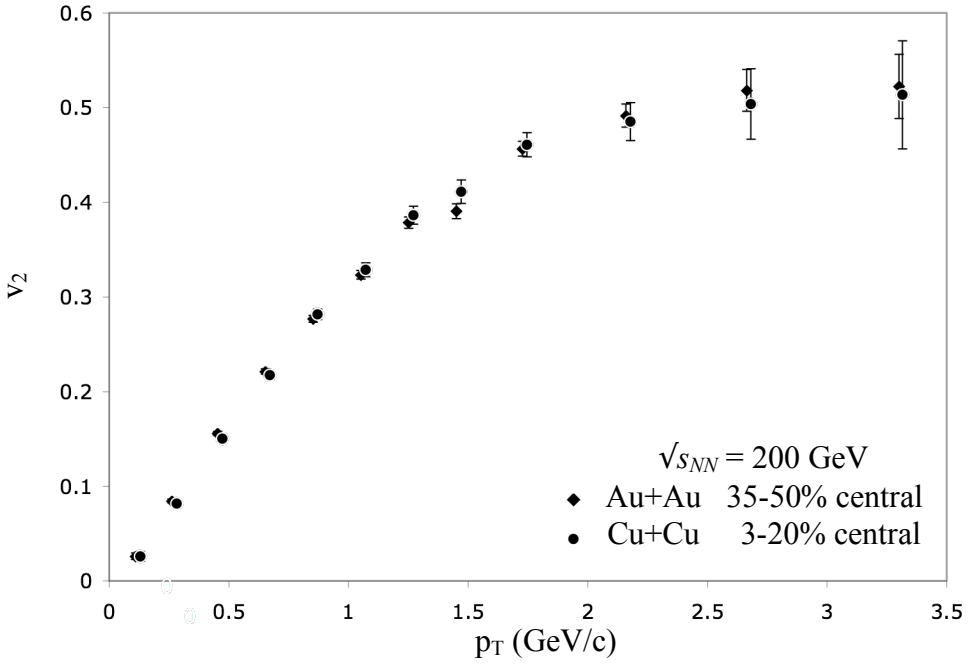

Figure 6.18: $v_2(p_T)$ for the 200-GeV data for Au+Au (diamonds) from 35-50% centrality and Cu+Cu (circles) from 3-20% centrality. The error bars are 1σ statistical errors.

Chapter 7: Discussion

7.1: Eccentricity interpretations

The reaction plane eccentricity ε_{RP} and the participant eccentricity ε_{part} were introduced in Sec. 3.7. In reality, ε_{part} is a much more recent innovation, and, moreover, it was initially motivated by the data in Fig. 6.11. The surprise, as was mentioned in Sec. 6.2, is that central Cu+Cu collisions exhibit greater v_2 than central Au+Au collisions. Considering that the elliptic flow is widely interpreted as a collective behavior arising in many-particle systems, the larger v_2 from the fewer-particle system was difficult to interpret. The reaction plane eccentricity failed to unify the data sets, but there was no evidence of a deeper meaning behind the disagreement.

Following a particularly inspired discussion at a PHOBOS collaboration meeting in 2005, the idea of the participant eccentricity began to develop. Regarding the Glauber Monte Carlo model, it had been previously suggested that, not just the mean, but also the event-by-event fluctuations in the reaction plane eccentricity should be taken seriously [Mil03]. In spite of this, the idea of reorienting the system on a per-event basis relative to the principal axes had not previously been considered.

The participant eccentricity has an attractive physical interpretation. It suggests that the shape of the participant region alone establishes the hydrodynamic expansion, and alignment with the reaction plane is arbitrary. Because the eccentricity is determined relative to the principal axis of the participant matter, there is no place in this interpretation for anti-alignment of the participant ellipse, nor for negative values of v_2. This agrees well with the event plane method, which has no inherent mechanism for

negative v_2 since Ψ_2 is always taken as the direction of the greatest back-to-back expansion.

The participant eccentricity was first introduced by the PHOBOS collaboration at the 2005 Quark Matter conference [Man06]. Since then it has become widely adopted in the RHIC community. The idea of per-event fluctuations in the initial eccentricity has also lately led to efforts to measure the magnitude of event-by-event flow fluctuations [Alv08d]. Finally, it has recently been suggested that the event plane method is sensitive to a value between the mean and RMS participant eccentricity, but it should be noted that there is generally little difference between these values (as is demonstrated in [Alv08b] and [Nou07]).

7.2: The hydrodynamic limit

In Sec. 1.8, it was observed that a hydrodynamic description requires an equation of state. Elliptic flow depends on the stiffness of the EoS, and this, in turn, depends on the degrees of freedom of the medium (*i.e.* hadronic vs. quark matter). Neglecting for a moment the dependence of v_2 on the stiffness, hydrodynamics is sometimes characterized as a constant, limiting behavior. The meaning of the limit is that, for some overlap shape, the ideal hydrodynamic expansion is independent of both the energy scale and the number of particles in the system.

Figure 7.1 shows v_2 for various collision energies, extending from Brookhaven's AGS to the CERN SPS to RHIC. Why does v_2 grow with collision energy when hydrodynamics is energy independent? The idea is that the hydrodynamic behavior is turning on slowly over this range of collision energies. As the energy increases, the density of produced particles increases, the mean free path decreases, and the system is

altogether better treated with thermodynamics and hydrodynamics. In other words, at lower energies the system is only partially thermalized, and, in contrast, the hydrodynamic limit describes v_2 for a completely thermal system (*i.e.* where internal re-scattering far outpaces the timescale of the hydrodynamic expansion).

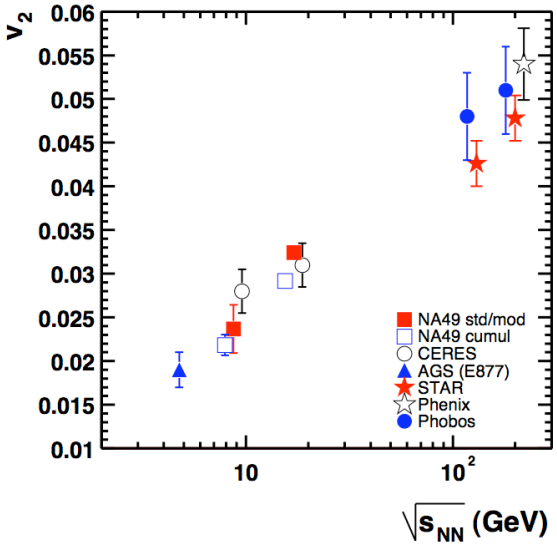

Figure 7.1: The magnitude of v_2 at midrapidity for semi-central collisions (roughly 10% to 35% centrality) from different experiments at various beam energies [Alt03]. These are for Au+Au and Pb+Pb collisions, which are systems of similar size.

In this analysis the v_2 increases with increasing RHIC collision energies. This can be observed in Fig. 6.14. The two collision energies appear slightly separated, with the higher energy corresponding to higher elliptic flow, and this trend can be seen over a broad range of collision centralities. This suggests that, over the range of most of the collisions at RHIC, the hydrodynamic limit has not been reached.

7.3: Area density scaling

How might the eccentricity-scaled v_2 be united over the different collision energies and system sizes? It has been suggested that v_2/ε is proportional to the number of charged particles observed at midrapidity dN_{ch}/dy (approximated as $dN_{ch}/d\eta$ at PHOBOS) divided by the overlap area of the colliding nuclei S as determined by a Glauber model [Vol00, Vol07]. This is sometimes called the *area density*, and it reflects the density within the hydrodynamic source. This expression naturally folds in the collision energy dependence because there are more particles produced (and, therefore, more particles observed at midrapidity in the final state) as the energy increases.

For a historical sense of perspective, Fig. 7.2 shows a pre-RHIC prediction of the hydrodynamic behavior slowly turning on with increasing area density, until it finally reaches the fully thermalized hydrodynamic limit [Vol00]. The limit itself depends upon the EoS and, therefore, the phase of matter. The choice of eccentricity is relatively unimportant in this figure since the ions being collided are relatively large.

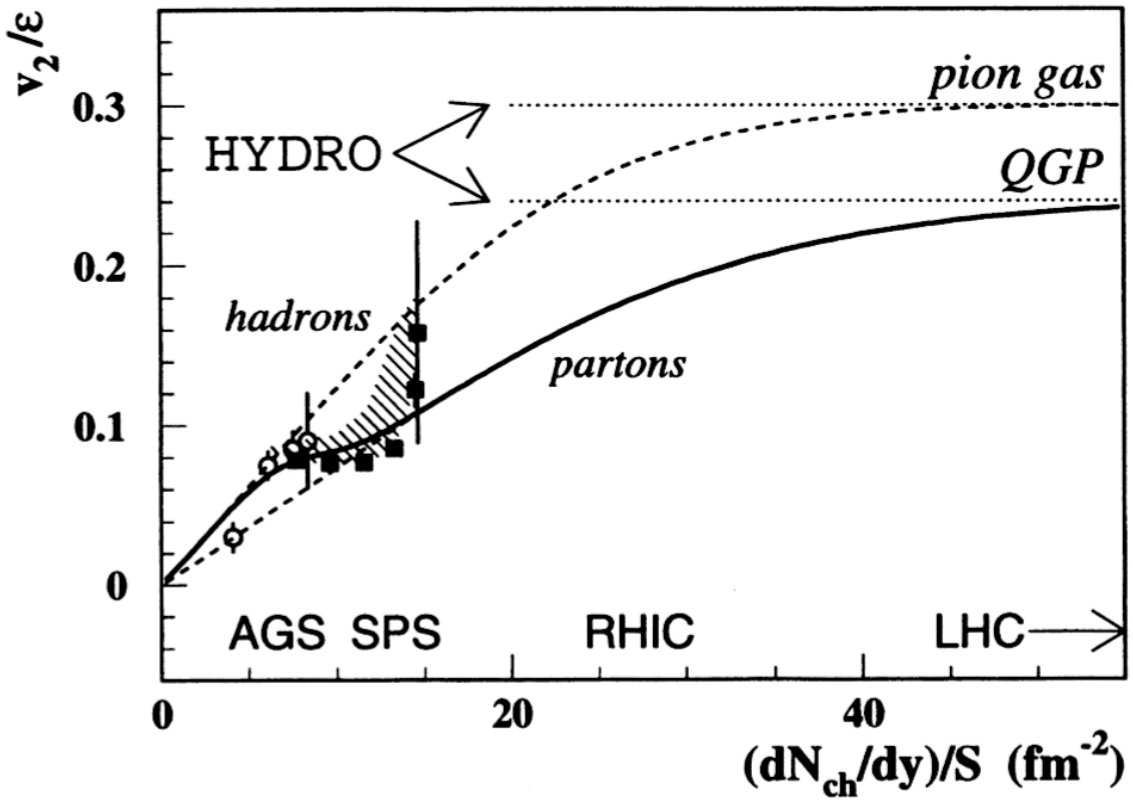

Figure 7.2: Initial predictions of the build-up of hydrodynamics up to limiting values for a pion gas (hadronic) and a quark gluon plasma [Vol00]. The open circles show v_2/ε from the Brookhaven AGS (Au+Au), and the filled squares show v_2/ε from the CERN SPS (Pb+Pb). The shaded area shows a systematic uncertainty in the SPS data, and the bars represent the statistical uncertainty. The solid black line depicts a possible cross-over from the hadronic to QGP phase.

To compare to this prediction to data, Fig. 7.3 shows v_2/ε_{part} as a function of the area density for the four data sets in this analysis. In the preparation of Fig. 7.3, $v_2(y)$ at midrapidity was approximated as $0.9 \times v_2(\eta)$, and the particle density dN/dy was approximated as $1.15 \times dN/d\eta$ for $|\eta| < 1$. This was done following the previous example of [Nou07]. The overlap area S was found using the PHOBOS Glauber MC model. It can be seen that the eccentricity-scaled v_2 grows as the area density increases, and the data from the different collision systems essentially follow the same universal curve.

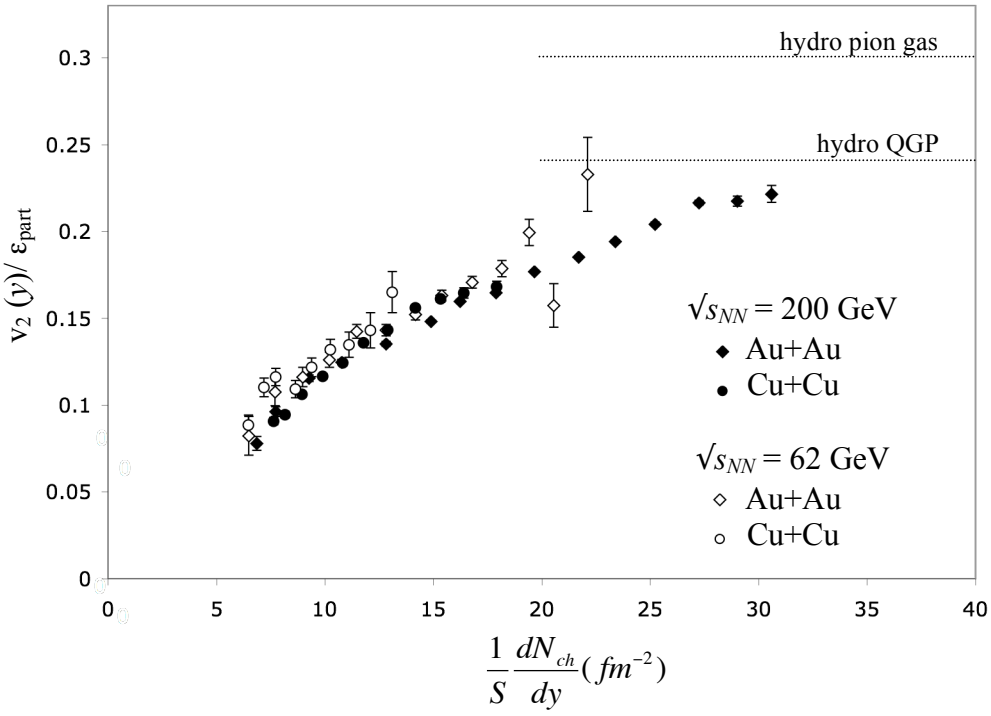

Figure 7.3: $v_2(y)/\varepsilon_{part}$ with respect to the area density for Au+Au collisions (diamonds) and Cu+Cu collisions (circles) at $\sqrt{s_{NN}}$ = 200 GeV (filled markers) and $\sqrt{s_{NN}}$ = 62 GeV (hollow markers). The error bars are 1σ statistical errors. The hydro bands are the early predictions in Fig. 7.2.

7.4: The history of the "perfect liquid" at RHIC

A quick comparison of Fig. 7.2 and Fig. 7.3 shows that the most-central Au+Au 200-GeV collisions are nearly at the hydrodynamic limit. Other estimates suggest the data actually *is* at the limit. Based in large part on the agreement with non-viscous hydrodynamics, an announcement was made at a press conference in 2005 with the message that the four RHIC experiments had observed a so-called "perfect liquid". This occurred just a month after a theoretical study that postulated a quantum-mechanical lower limit of viscosity, so the subtle subtext of the press conference became "as perfect a liquid as nature will allow".

Interestingly, the theoretical quantum limit is one of the most notable of several instances in which string theory has been used to describe RHIC matter (employing the AdS/CFT correspondence). The quantum limit is a lower bound for the value of the shear viscosity η divided by the entropy density s (the entropy per unit volume) in terms of $\hbar/k_B$. In this case, it is convenient to use natural units, where $\hbar = k_B = 1$. Then, the limit is given as $\eta/s \geq 1/4\pi$ [Kov05]. In comparison, water under normal conditions is about 380× the quantum limit. Helium at the λ transition (where it becomes a superfluid) is about 9× the quantum limit. Near to the transition, there is a minimum in η/s as a function of temperature, and this is actually characteristic of phase transitions in many other fluids as well. Such a minimum in η/s has been suggested as a way of finding the QGP phase transition [Cse06], but as will be discussed in Sec. 7.5, measuring the small viscosity at RHIC is non-trivial! Finally, the lithium gas in Appendix A may also be very close to the quantum limit.

The press conference was used as a venue to introduce "white papers" from the four experiments. These provided experimental overviews summarizing what had been learned during the preceding years of RHIC running. The conclusion from PHOBOS, based greatly on the previous Au+Au 200-GeV flow analysis, was that the system thermalizes within 1-2 fm/c, and that the corresponding energy density of the system at that moment is greater than 3 GeV/fm^3. The PHOBOS white paper noted that the initially conceived, weakly-interacting QGP had not been observed, but the data could no longer be characterized simply in terms of hadronic degrees of freedom [Bac05a].

7.5: Viscous hydrodynamic predictions

How does Fig. 7.3 compare to modern hydrodynamic predictions? The latest theoretical approaches are generally more complicated than the ideal, two-dimensional hydrodynamics used in Fig. 7.2. While the former model predicts the basic features of flow in the transverse plane, viscous three-dimensional hydrodynamic models are needed to address the broad variety of features in the data, for example, the pseudorapidity dependence of v_2 [Csa04]. These models are generally followed by a microscopic cascade simulation, which further propagates the kinetics of the hadronic matter [Tea02].

As a baseline, Fig. 7.4 shows the ideal hydrodynamic behavior for collisions with various area densities. On the whole, these data lie on the same limiting hydrodynamic curve. (This curve would be a flat line if the EoS was neglected.)

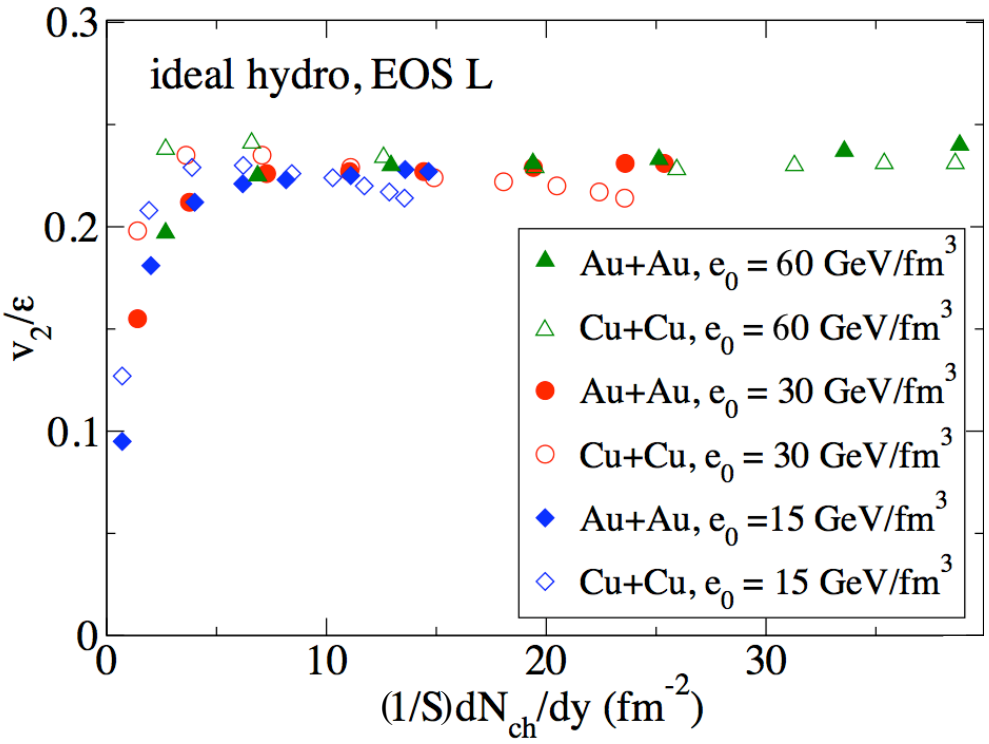

Figure 7.4: Ideal (non-viscous) hydrodynamic simulations of v_2/ε as a function of area density. Values are presented for three initial energy densities (15, 30, and 60 GeV/fm^3) and two systems (Au+Au and Cu+Cu). Within each series, the different points represent different impact parameters. The choice of the EoS is described in [Son08].

In comparison, Fig. 7.5 represents the hydrodynamical limiting behavior of fluids for several values of η/s [Son08]. Curves have been drawn through the Au+Au 200-GeV points for each band of η/s to help guide the eye. The authors note the unrealistic use of a constant value of η/s over a broad range of collisions, but they still make several interesting qualitative arguments based on their model. At low area densities, the experimental data in Fig. 7.3 agrees better with the more viscous simulated data in Fig. 7.5. Conversely, at the highest area densities, the experimental data surpasses even the least-viscous simulation shown (which is near to the $1/4\pi$ limit). This, it is suggested, is a result of the system spending more time in the viscous hadronic phase for low-area density collisions, compared collisions at higher area densities that undergo hydrodynamic expansion in the non-viscous QGP phase.

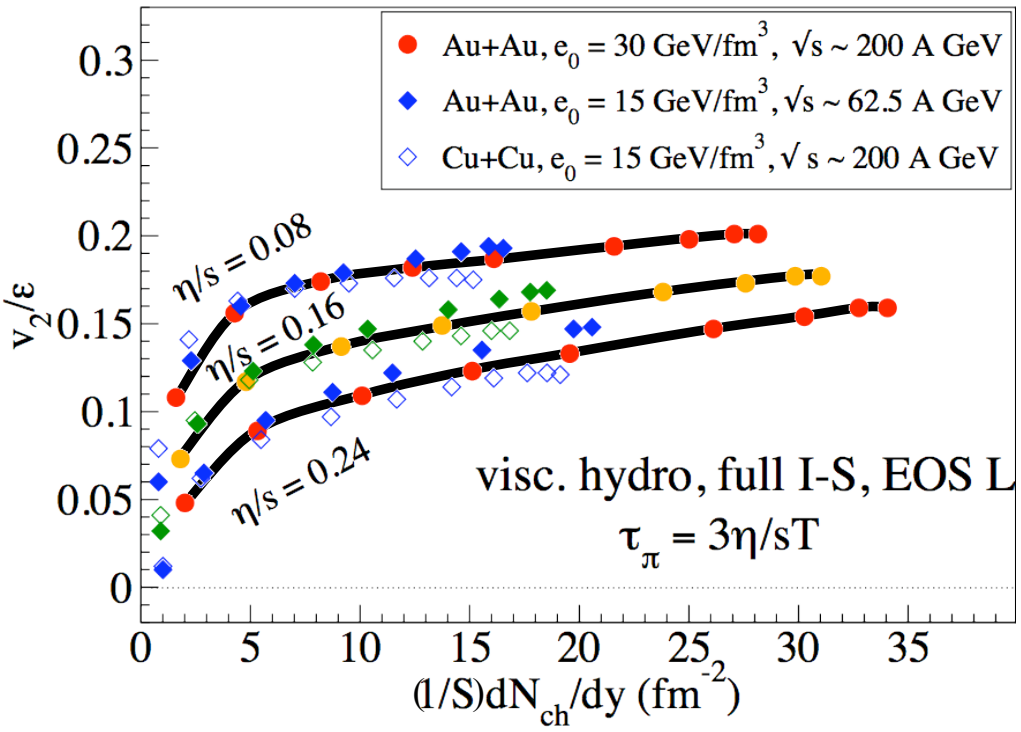

Figure 7.5: Viscous hydrodynamic results illustrating v_2/ε with respect to the area density. Calculations are done for three different fluid viscosities (η/s=0.08, the least viscous, is represented by blue and red markers; η/s=0.16 is represented by orange and green markers; and η/s=0.24 is also represented by blue and red markers). For each viscosity, three initial conditions were chosen. These are meant to reflect Au+Au 200-GeV collisions (solid circles), Au+Au 62-GeV collisions (solid diamonds), and Cu+Cu 200-GeV collisions (open diamonds). Each of the points in a series (*i.e.* having the same viscosity and initial conditions) represents a different impact parameter. The details of the I-S hydronamic equation, the EoS, and the relaxation time τ_π can be found in [Son08]. Lines were drawn through the Au+Au 200-GeV data to help guide the eye.

7.6: Hydrodynamic behavior of $v_2(p_T)$

A characteristic of the hydrodynamic expansion is that the elliptic flow will vary for particles of different mass, and this is seen in the differential measurement of v_2 with respect to transverse momentum (shown in Fig. 6.15). The hydrodynamic trend breaks just beyond this figure at p_T of 1.5 to 2 GeV/c, as reported in [Ad103]. The idea here is that low momentum particles come from the bulk, hydrodynamic expansion, while particles above 1 GeV/c indicate "hard" scattering physics. One interesting trend is that values of $v_2(p_T)$ can be made to roughly agree among many different particle species when v_2 is divided by the number of constituent quarks per particle n_q (*i.e.* 2 or 3) [Ada05]. This is compelling because it suggests that the hydrodynamics is in some way generated at the quark level (presumably in a QGP) rather than the hadronic level. The notable exception to this n_q scaling is the pions, which also happen to be the most abundantly produced particles.

Chapter 8: Conclusions

Heavy ion collisions at RHIC provide unprecedented experimental access to nuclear matter at extreme temperatures. Under these conditions, the hadronic matter has long been theorized to melt into a deconfined quark gluon plasma. One of the great surprises at RHIC, however, is the strong elliptic flow signal. This hydrodynamic behavior is not expected in a weakly interacting system, and, therefore, based on the v_2 measurements, the matter was necessarily recharacterized as a strongly interacting medium. Moreover, the elliptic flow provides an experimental constraint on the length of the thermalization time, which, according to a hydrodynamic interpretation, is 1 or 2 fm/c. Based on the estimates of the expansion rate and the overall energy, the time can be used to establish the energy density of the system just as it thermalizes. The consensus is that the energy density of the thermalized system is at least a few GeV/fm^3, which places central 200-GeV Au+Au collisions unambiguously into the QGP region of the nuclear phase diagram. Furthermore, according to many estimates, the magnitude of elliptic flow has reached an ideal-hydrodynamic limit for these central events, leading to the view that the QGP at RHIC is among nature's least-viscous materials.

With these results in mind, the importance of v_2 as an experimental indicator of hydrodynamic behavior cannot be understated. Therefore, the challenge posed by the Cu+Cu data to the prevailing hydrodynamic interpretation at RHIC was very significant. Initially it was not understood how central Cu+Cu collisions could generate greater elliptic flow than central Au+Au collisions. This was the most striking inconguity, but the deeper problem was seen across all centralities when v_2 was divided by the (reaction plane) eccentricity. The achievement of this analysis is that, not only was the Cu+Cu

elliptic flow measured, but an interpretation of the eccentricity was developed (the participant eccentricity) that unifies the Cu+Cu and Au+Au collision systems in agreement with hydrodynamic expectations.

With the eccentricity dependence removed, the data scales smoothly as a function of the number of participants, with both species resting on the same curve for a given collision energy. The agreement also extends to the differential measurement taken with respect to the transverse momentum. This can be seen when regions with matching mean N_{part} are compared between Cu+Cu and Au+Au. Finally, when the eccentricity-scaled elliptic flow is considered as a function of area density, the data from different collision energies are essentially joined on the same universal curve. The progression of this curve towards the suspected hydrodynamic limit should be interesting as the LHC begins producing collisions of even higher area density.

Appendix A: Interesting Related Phenomenon

Interesting parallels exist between the elliptic flow observed in heavy ion collisions and several phenomena in other fields. Both of the observations below are interesting because they illustrate liquid-like behavior in systems with relatively few particles. Figure A.1 shows the anisotropic expansion of a cold, strongly interacting Fermi gas (Li atoms in a degenerate state) abruptly released from an optical trap [OHa02]. The initial state is highly anisotropic (with roughly an aspect ratio of 1:30), and it contains around 200,000 atoms. In contrast, the multiplicity of the highest-energy lab-observed heavy ion collisions is a few thousand particles.

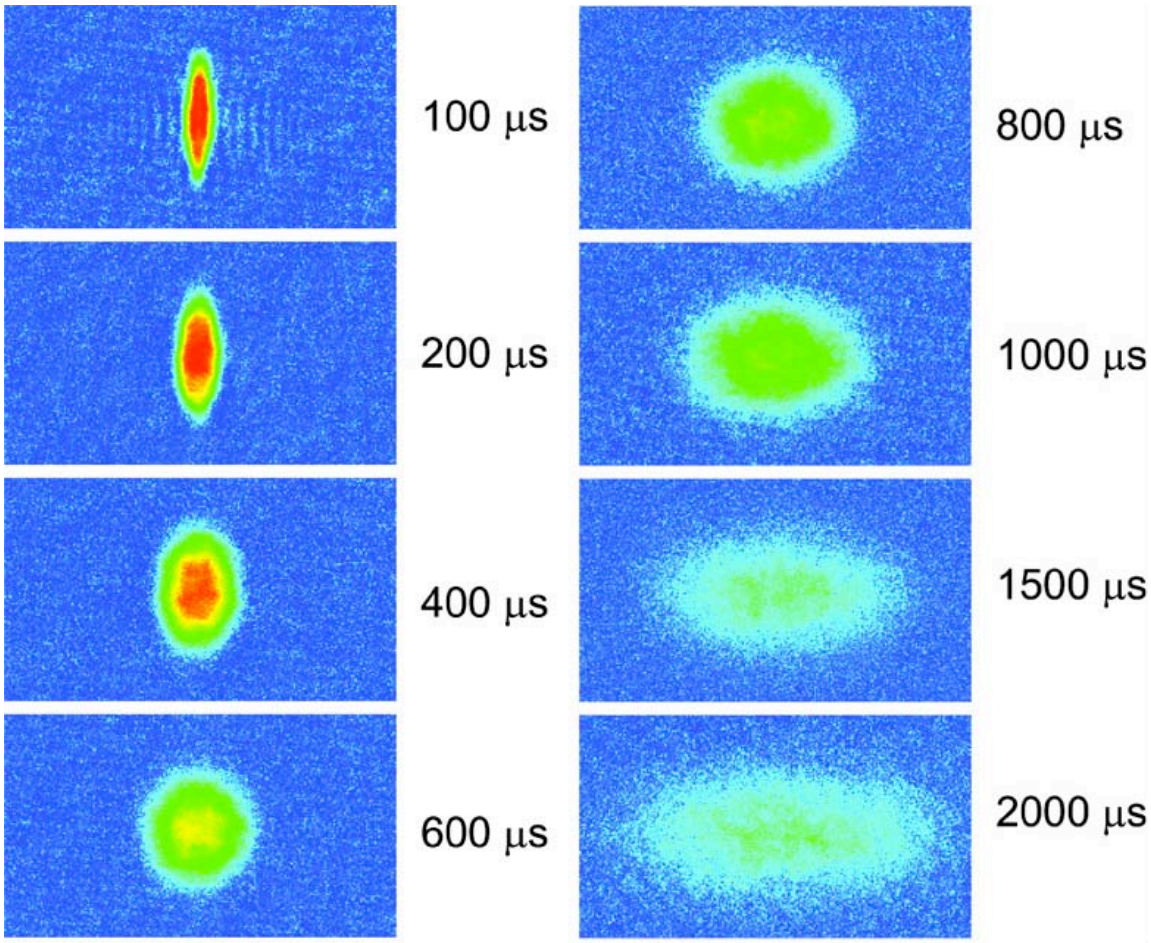

Figure A.1: The anisotropic expansion of a cold, degenerate gas of fermions [OHa02].

Another interesting experiment involves polished (*i.e.* non-cohesive), 100 μm glass beads, propelled together in a column anywhere between 1 to 16 m/s via high-pressure gas, and directed toward a flat target [Che07]. Depending on the size of the target relative to the diameter of the particle stream, the resulting fluid-like movement ranges from a "water bell" spread around the target to the narrow perpendicular spray shown in Fig. A.2.

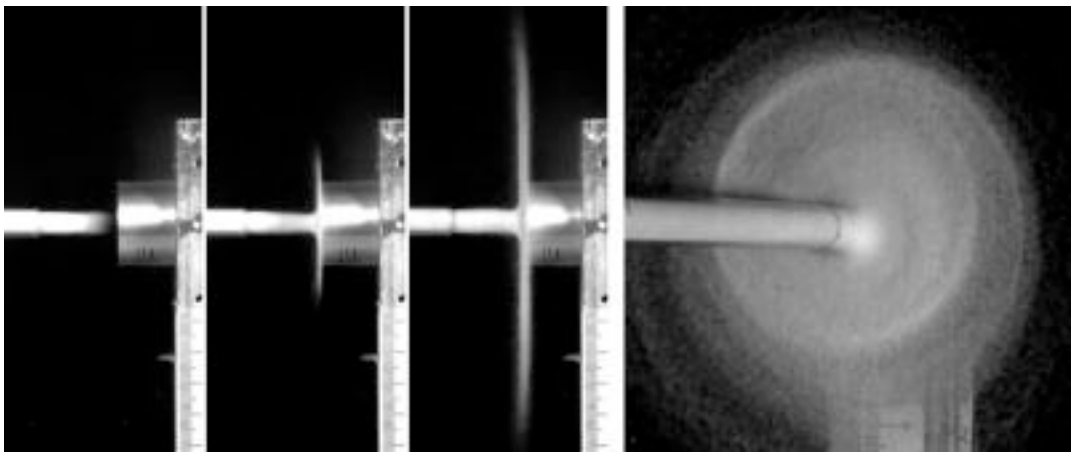

Figure A.2: A stream of 100 μm glass beads moving at 10 m/s exhibits fluid behavior upon hitting a flat target [Che07]. The images show the side view of the jet 0.5 ms before as well as 2.5 ms and 9.5 ms after impact (left to right). Also, an axial view is shown 35.5 ms after impact.

The fluid behavior depends on the density of the particle stream. At lower particle densities, the spray exhibits a less fluid and more particle-like response as seen in Fig. A.3.

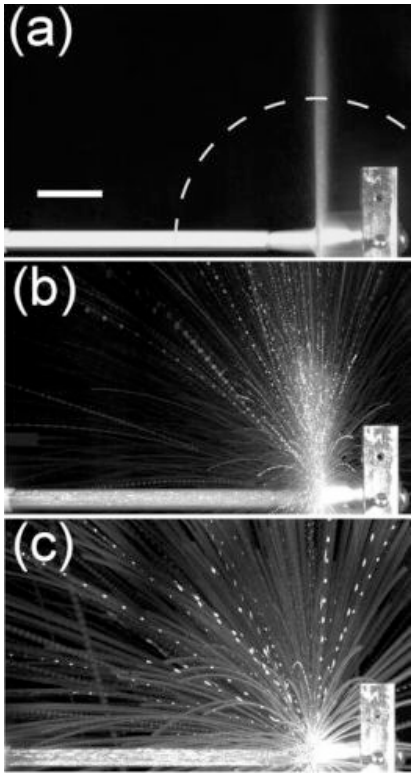

Figure A.3: The behavior of a stream of glass beads with respect to the particle density [Che07]. The density of particles decreases moving from panel (a) to panel (c).

In a further experiment, the column of glass beads was shaped so the initial cross section was rectangular instead of circular, and, interestingly, the expansion was anisotropic similar to the observations in heavy ion collisions. This is of particular interest because it illustrates how particles can behave like a liquid even when there are apparently no attractive or cohesive forces holding the medium together.

Appendix B: A Few Words on Relativity

Relativity means that certain observations will change depending on the frame of reference from which motion is observed. An example is the apparent flattening (as viewed from the laboratory frame) of two approaching relativistic nuclei (which are spherical in their respective rest frames). This is a Lorentz length contraction, and it is accompanied by a complementary phenomenon called time dilation. Both of these transformations are expressed simply with the relativistic variable γ

$$\gamma = 1/\sqrt{1-\beta^2} \quad \text{B.1}$$

Here β is defined as v/c, the particle velocity divided by the speed of light. An initial length dimension is apparently contracted to $L=L_0/\gamma$. Conversely, an initial time interval is apparently lengthened to $t = t_0 \gamma$.

Classical vectors such as velocity and momentum are not conserved when observed from different frames of reference. To maintain a consistent mathematical framework regardless of the frame of motion, several variables are used that require either trivial transformations or are completely invariant under the Lorentz transformation (called "relativistic-invariant" variables elsewhere in this thesis). One example is the nucleon-nucleon collision energy, $\sqrt{s_{NN}}$. This is chosen as the expression of energy because it is the same for all reference frames. Another useful Lorentz invariant variable is the rapidity y, which is a measure of speed of a particle, and is described by

$$y = \frac{1}{2}\ln\left(\frac{E+p_z}{E-p_z}\right) \quad \text{B.2}$$

The longitudinal momentum p_z is the component of the momentum vector along the beam axis (where $p^2=p_x^2+p_y^2+p_z^2$) and the energy of the particle is $E=\gamma mc^2$. Unlike velocity, rapidity is additive at relativistic speeds, and, therefore, when the reference frame is shifted, the rapidity is also shifted by means of a simple addition.

Pseudorapidity η is a polar coordinate variable that is used throughout this thesis. It is defined as

$$\eta = -\ln\left[\tan\left(\frac{\theta}{2}\right)\right], \qquad \text{B.3}$$

where θ is the angle measured with respect to the beam axis. Pseudorapidity is used because, in the limit that a particle is moving at the speed of light, it is equivalent to rapidity. Particles at shallow angles relative to the beam axis are said to reside at *forward rapidities*. *Midrapidity* describes angles perpendicular to the beam axis, particularly those from $-1<\eta<1$.

Appendix C: Some Characteristics of RHIC Collisions

Figure C.1 presents the charged particle multiplicity as a function of pseudorapidity for Cu+Cu and Au+Au at various collision energies and centralities.

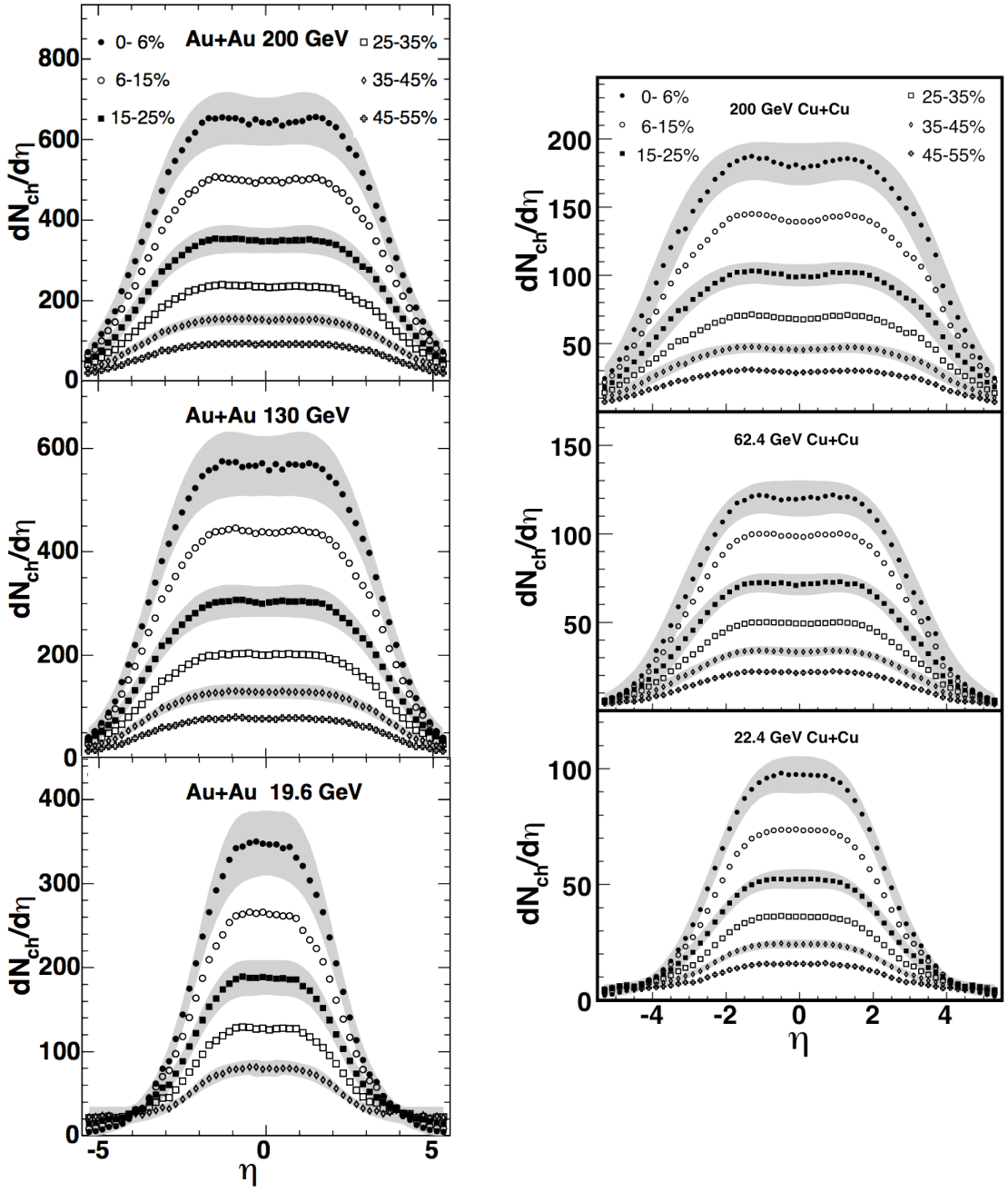

Figure C.1: The charged particle multiplicities for Au+Au and Cu+Cu at several collision energies in different bins of centrality [Alv08c, Bak05a].

The elliptical flow is shown as a function of pseudorapidity in Fig C.2.

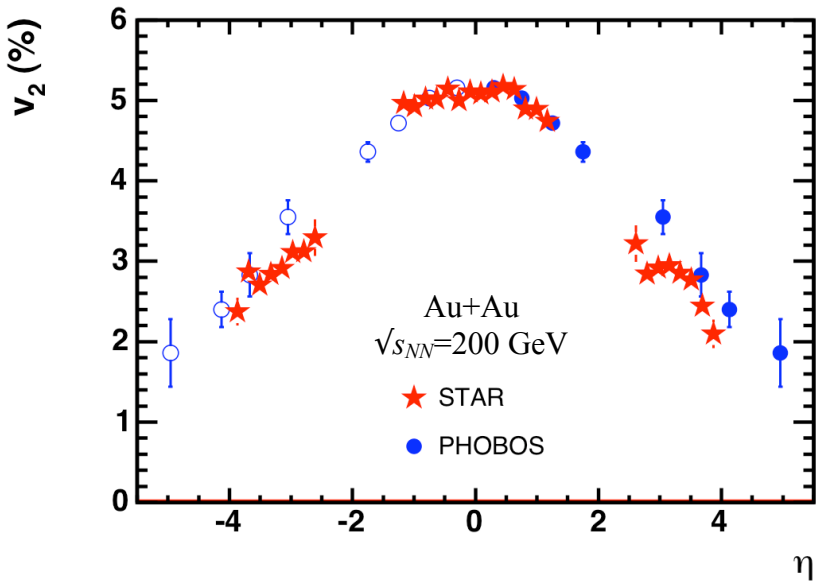

Figure C.2: Elliptic flow as a function of pseudorapidity for Au+Au collisions at $\sqrt{s_{NN}}$=200 GeV as measured by the STAR and PHOBOS experiments. The centrality range is 15-25%.

Appendix D: Quark Contents of Selected Mesons and Baryons

Table D.1: Quark Contents of Selected Mesons

Particle Symbol	Quark Content
π^-	$u\bar{d}$
π^0	$\frac{1}{\sqrt{2}}\left(d\bar{d}-u\bar{u}\right)$
π^+	$u\bar{d}$
K^-	$\bar{u}s$
K^0	$d\bar{s}$
K^+	$u\bar{s}$
$\overline{K}^0$	$\bar{d}s$
D^-	$\bar{c}d$
D^+	$c\bar{d}$
J/Ψ	$c\bar{c}$

Table D.2: Quark Contents of Selected Baryons

Particle Symbol	Quark Content
p	uud
$\bar{p}$	$\bar{u}\bar{u}\bar{d}$
n	udd
Σ^+	uus
Σ^-	dds
Ξ^0	uss
Ξ^-	dss

Appendix E: Cuts and Partitioning of Data from the Spectrometer

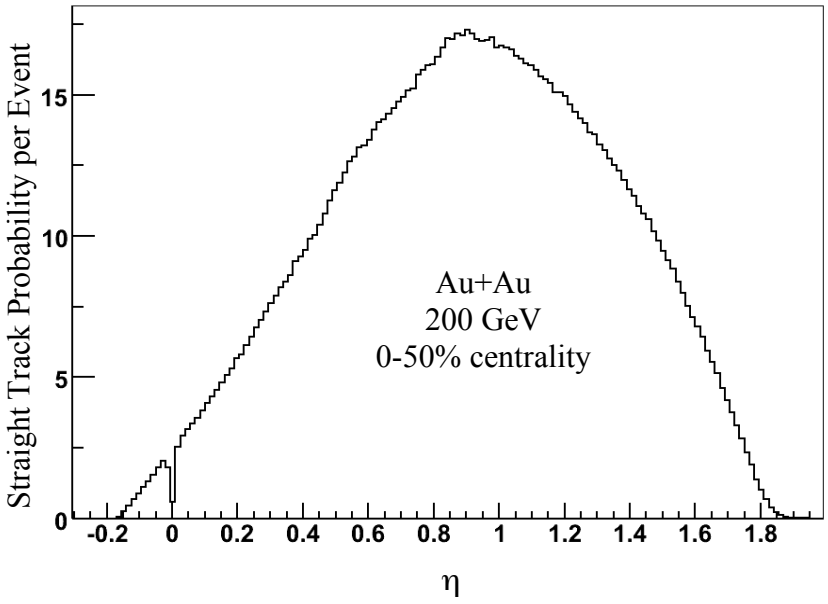

Figure E.1: The probability distribution of straight tracks versus pseudorapidity for Au+Au collisions at 200 GeV. This has been normalized to the average number of tracks in an event. For the integrated flow measurement, straight tracks were used between $0<\eta<1$. The dip at $\eta=0$ comes from a slight inefficiency of the tracking algorithm at this point.

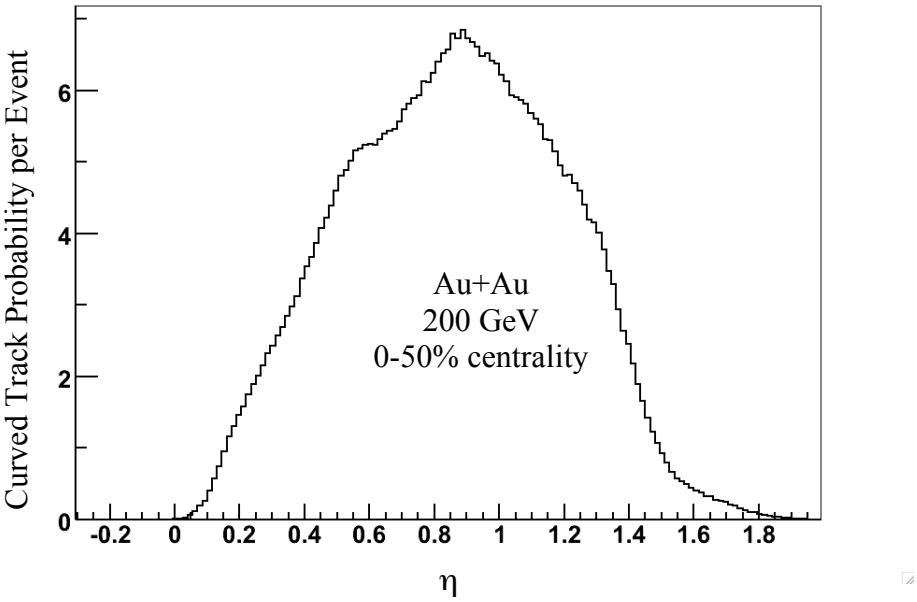

Figure E.2: The probability distribution for curved tracks versus pseudorapidity for Au+Au collisions at 200 GeV. This has been normalized to the average number of tracks in an event. For the differential flow measurement, curved tracks were used between $0<\eta<1.6$.

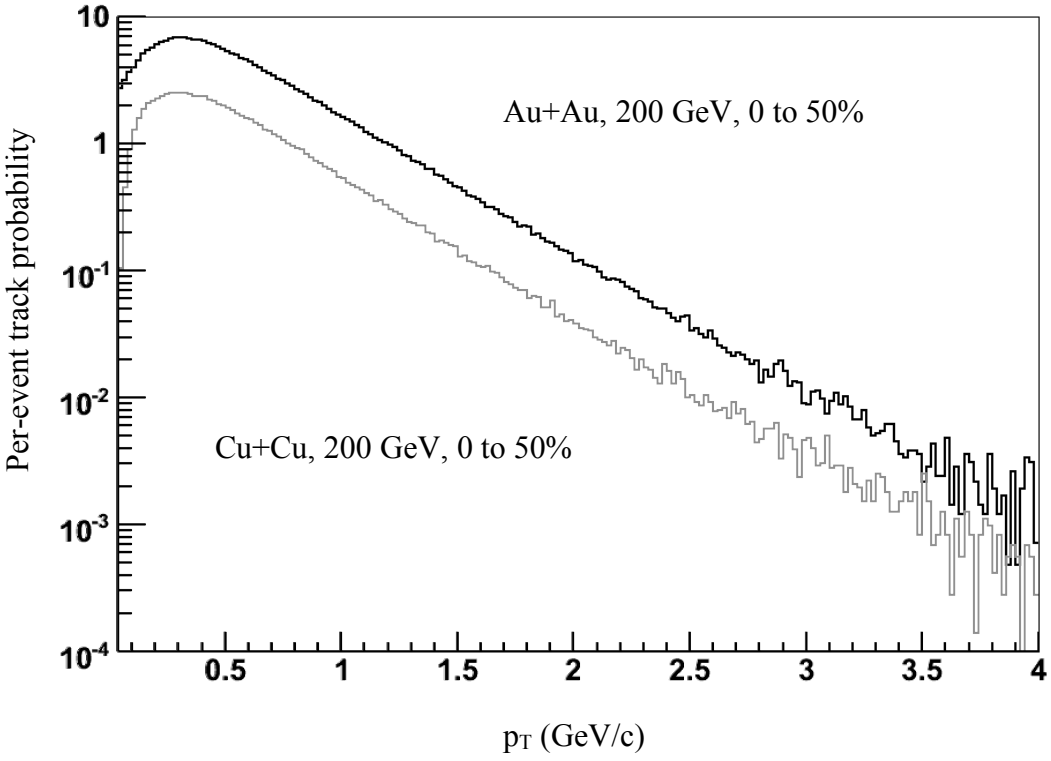

Figure E.3: The probability distribution for the momentum of tracks in an event. The two curves are for Au+Au and Cu+Cu at 200 GeV. These have been normalized respectively to the average number of tracks per event. In the differential v_2 analysis, the p_T bins were from 0 to 0.2 GeV/c, and subsequent 0.2 GeV/c bins up until 1.6 GeV. Afterwards, the bins were 1.6-2.0, 2.0-2.5, 2.5-3.0, and 3.0-4.0 GeV/c.

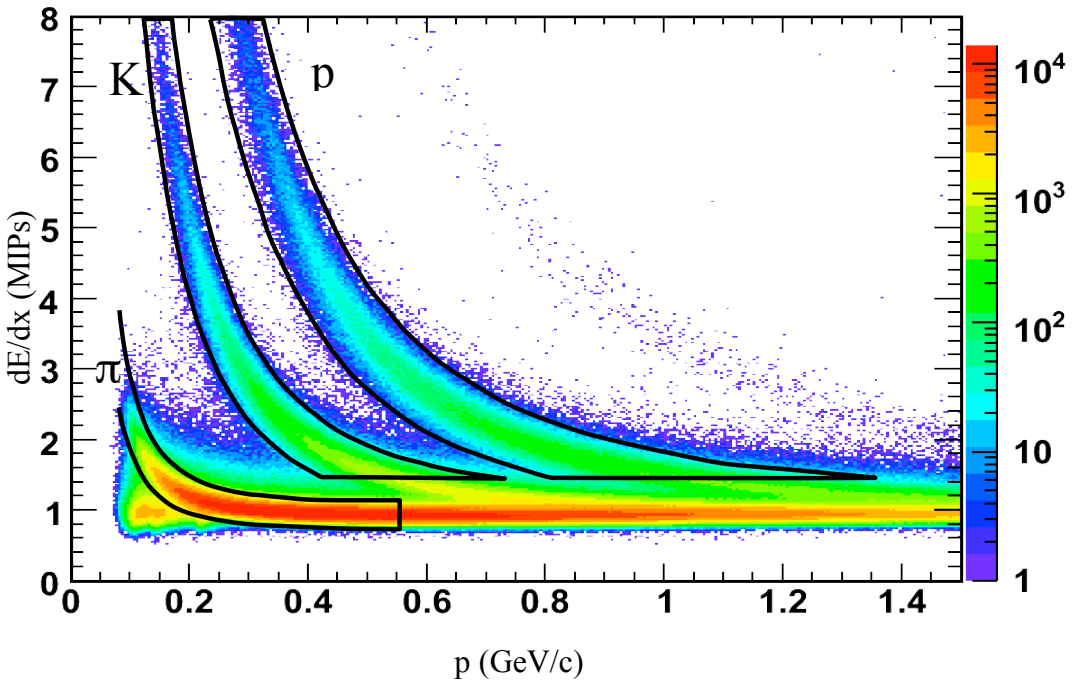

Figure E.4: Particle identification cuts for tracks in the PHOBOS spectrometer based on *dE/dx* versus *p*. Moving left to right, the black curves show the selections of charged pions (π^+ and π^-), kaons (K^+ and K^-), and (anti)protons (p and $\bar{p}$), respectively.

Appendix F: Notes on the Difference Between Subevents

The resolution is determined as $\sqrt{2}\alpha\sqrt{\langle\cos(2(\Psi_{2A}-\Psi_{2B}))\rangle}$. An example of the distribution of $\cos(2(\Psi_{2A}-\Psi_{2B}))$ is shown for illustration in Fig. F.1. Those events with little difference between Ψ_{2A} and Ψ_{2B} contribute to the positive peak, and those anti-aligned events (Ψ_{2A} and Ψ_{2B} separated by ½ π rad) contribute to the negative peak. Clearly, in this analysis, the positive peak must be greater than the negative peak. If Ψ_{2A} and Ψ_{2B} were uncorrelated, then the mean would be zero.

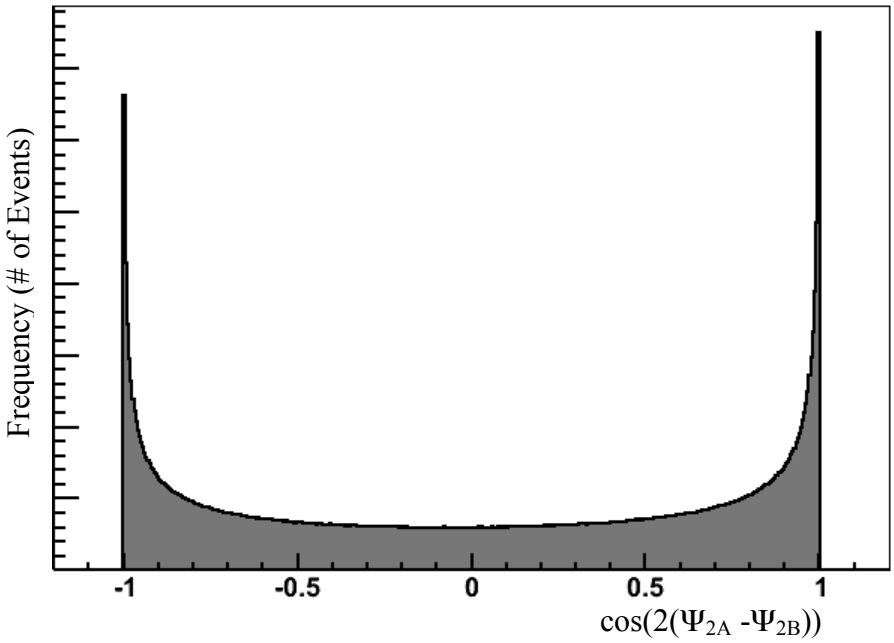

Figure F.1: The distribution of $\cos(2(\Psi_{2A}-\Psi_{2B}))$ for the Cu+Cu 200-GeV data set.

An interesting way of looking at the difference between Ψ_{2A} and Ψ_{2B} is shown in Fig. F.2. Consider that Ψ_{2A} and Ψ_{2B} are both measurements of Ψ_R, therefore, the expectation value for the difference (Ψ_{2A}-Ψ_{2B}) is zero. The distribution governing the spread around this expectation value is apparently Gaussian, though this is not instantly clear. The difference between Ψ_{2A} and Ψ_{2B} cannot be larger than ½ π meaning that the wings of the Gaussian distribution must fold back inward periodically. In effect, the far-out values expected in a normal distribution are "so wrong that they're right".

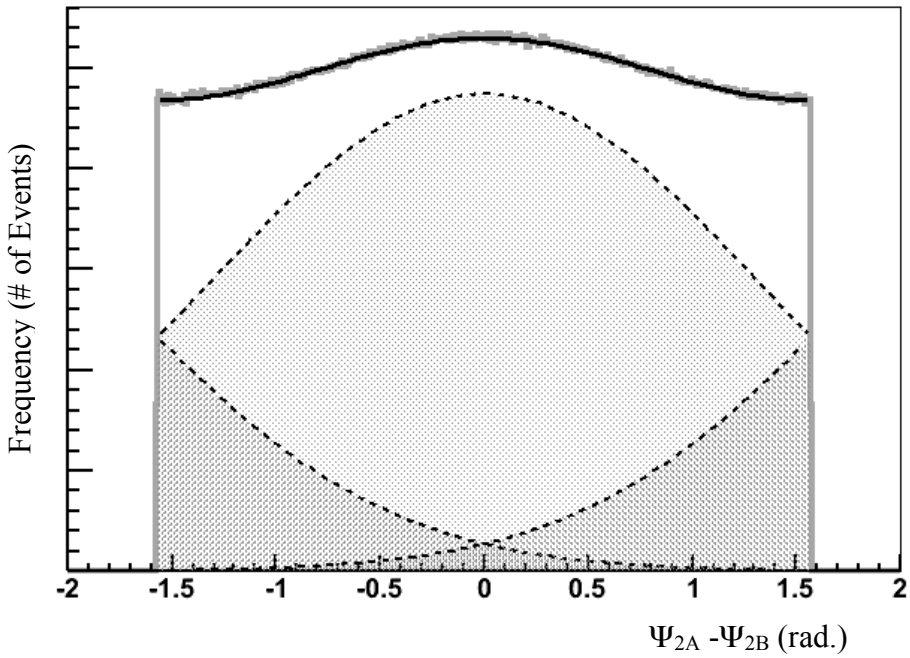

Figure F.2: The difference between two subevent measurements of the reaction plane. The data from the Cu+Cu 200-GeV data set is shown (gray line), along with the fit (solid black line). The fit function is generated by summing the pieces of a folded Gaussian distribution (dotted black line).

Appendix G: Tables of Data

Table G.1: $v_2(N_{part})$ for the Au+Au 200 GeV Data Set

N_{part}	v_2	stat. error	sys. high	sys. low
20	0.0535	0.0025	0.0084	0.0107
28	0.0606	0.0016	0.0054	0.0040
37	0.0674	0.0010	0.0018	0.0073
49	0.0676	0.0007	0.0025	0.0039
65	0.0678	0.0006	0.0014	0.0018
82	0.0685	0.0004	0.0028	0.0027
101	0.0680	0.0004	0.0016	0.0026
123	0.0638	0.0003	0.0015	0.0018
149	0.0607	0.0002	0.0011	0.0014
181	0.0555	0.0002	0.0009	0.0013
215	0.0486	0.0002	0.0006	0.0013
256	0.0407	0.0002	0.0008	0.0015
297	0.0323	0.0002	0.0008	0.0018
330	0.0249	0.0003	0.0011	0.0022
359	0.0200	0.0004	0.0018	0.0029

Table G.2: $v_2(N_{part})$ for the Au+Au 62 GeV Data Set

N_{part}	v_2	stat. error	sys. high	sys. low
36	0.0493	0.0060	0.0084	0.0107
48	0.0596	0.0040	0.0054	0.0040
62	0.0601	0.0026	0.0018	0.0073
79	0.0603	0.0019	0.0025	0.0039
98	0.0625	0.0016	0.0014	0.0018
120	0.0575	0.0012	0.0028	0.0027
145	0.0548	0.0010	0.0016	0.0026
174	0.0515	0.0009	0.0015	0.0018
209	0.0454	0.0008	0.0011	0.0014
248	0.0381	0.0009	0.0009	0.0013
288	0.0324	0.0011	0.0006	0.0013
323	0.0194	0.0014	0.0008	0.0015
349	0.0230	0.0019	0.0008	0.0018

Table G.3: $v_2(N_{part})$ for the Cu+Cu 200 GeV Data Set

N_{part}	v_2	stat. error	sys. high	sys. low
21	0.0544	0.0011	0.0063	0.0066
26	0.0510	0.0009	0.0044	0.0032
32	0.0515	0.0007	0.0017	0.0021
39	0.0508	0.0006	0.0035	0.0039
47	0.0485	0.0005	0.0027	0.0024
56	0.0466	0.0004	0.0026	0.0029
67	0.0433	0.0004	0.0028	0.0027
79	0.0399	0.0004	0.0019	0.0019
90	0.0349	0.0004	0.0024	0.0021
101	0.0313	0.0005	0.0022	0.0016
108	0.0290	0.0005	0.0011	0.0013

Table G.4: $v_2(N_{part})$ for the Cu+Cu 62 GeV Data Set

N_{part}	v_2	stat. error	sys. high	sys. low
31	0.0440	0.0026	0.0063	0.0066
38	0.0497	0.0022	0.0044	0.0032
46	0.0462	0.0018	0.0017	0.0021
54	0.0388	0.0016	0.0035	0.0039
64	0.0377	0.0015	0.0027	0.0024
76	0.0352	0.0014	0.0026	0.0029
87	0.0307	0.0015	0.0028	0.0027
96	0.0296	0.0019	0.0019	0.0019
105	0.0311	0.0020	0.0024	0.0021

Table G.5: $v_2(p_T)$ for the Au+Au 200 GeV Data Set

p_T	v_2	stat. error	sys. high	sys. low
0.15	0.0092	0.0011	0.0012	0.004
0.30	0.0208	0.0007	0.0013	0.0035
0.49	0.0362	0.0007	0.0011	0.0029
0.69	0.0553	0.0009	0.0006	0.0025
0.89	0.0701	0.0011	0.0007	0.0032
1.09	0.0801	0.0015	0.0009	0.0029
1.29	0.0932	0.0019	0.0005	0.0019
1.49	0.1057	0.0025	0.0000	0.0037
1.77	0.1179	0.0025	0.0019	0.0030
2.20	0.1370	0.0039	0.0022	0.0049
2.70	0.1409	0.0072	0.0021	0.0035
3.33	0.1392	0.0114	0.0061	0.0233

Table G.6: $v_2(p_T)$ for the Au+Au 62 GeV Data Set

p_T	v_2	stat. error	sys. high	sys. low
0.15	0.0098	0.0023	0.0012	0.004
0.30	0.0219	0.0014	0.0013	0.0035
0.49	0.0359	0.0015	0.0011	0.0029
0.69	0.0490	0.0019	0.0006	0.0025
0.89	0.0619	0.0025	0.0007	0.0032
1.09	0.0718	0.0033	0.0009	0.0029
1.29	0.0865	0.0044	0.0005	0.0019
1.49	0.0960	0.0059	0.0000	0.0037
1.76	0.1158	0.0062	0.0019	0.0030
2.19	0.1271	0.0104	0.0022	0.0049

Table G.7: $v_2(p_T)$ for the Cu+Cu 200 GeV Data Set

p_T	v_2	stat. error	sys. high	sys. low
0.15	0.0061	0.0009	0.0070	0.0073
0.30	0.0199	0.0005	0.0068	0.0071
0.49	0.0369	0.0006	0.0065	0.0068
0.69	0.0528	0.0007	0.0067	0.0070
0.89	0.0686	0.0009	0.0068	0.0071
1.09	0.0792	0.0012	0.0068	0.0071
1.29	0.0906	0.0016	0.0071	0.0074
1.49	0.1002	0.0021	0.0073	0.0076
1.77	0.1116	0.0022	0.0069	0.0072
2.20	0.1186	0.0034	0.0105	0.0107
2.70	0.1225	0.0063	0.0122	0.0124
3.34	0.1290	0.0096	0.0154	0.0155

Table G.8: $v_2(p_T)$ for the Cu+Cu 62 GeV Data Set

p_T	v_2	stat. error	sys. high	sys. low
0.15	0.0019	0.0032	0.0070	0.0073
0.30	0.0199	0.0019	0.0068	0.0071
0.49	0.0335	0.0021	0.0065	0.0068
0.69	0.0486	0.0027	0.0067	0.0070
0.89	0.0587	0.0036	0.0068	0.0071
1.09	0.0727	0.0049	0.0068	0.0071
1.29	0.0774	0.0066	0.0071	0.0074
1.49	0.0782	0.0089	0.0073	0.0076
1.76	0.0938	0.0096	0.0069	0.0072
2.19	0.0998	0.0162	0.0105	0.0107

Appendix H: Publications

PHOBOS Collaboration (inclusive of all RHIC runs):

B.Alver[4], B.B.Back[1], M.D.Baker[2], M.Ballintijn[4], D.S.Barton[2], B.Becker[2], R.R.Betts[6], A.A.Bickley[7], R.Bindel[7], A.Budzanowski[3], W.Busza[4], A.Carroll[2], Z.Chai[2], V.Chetluru[6], M.P.Decowski[4], E.Garcia[6], T.Gburek[3], N.George[{1,2}], K.Gulbrandsen[4], S.Gushue[2], C.Halliwell[6], J.Hamblen[8], I.Harnarine[6], A.S.Harrington[8], M.Hauer[2], G.A.Heintzelman[2], C.Henderson[4], D.J.Hofman[6], R.S.Hollis[6], R.Holynski[3], B.Holzman[2], A.Iordanova[6], E.Johnson[8], J.L.Kane[4], J.Katzy[{4,6}], N.Khan[8], W.Kucewicz[6], P.Kulinich[4], C.M.Kuo[5], J.W.Lee[4], W.Li[4], W.T.Lin[5], C.Loizides[4], S.Manly[8], D.McLeod[6], A.C.Mignerey[7], R.Nouicer[{2,6}], A.Olszewski[3], R.Pak[2], I.C.Park[8], H.Pernegger[4], C.Reed[4], L.P.Remsberg[2], E.Richardson[7], M.Reuter[6], C.Roland[4], G.Roland[4], L.Rosenberg[4], J.Sagerer[6], P.Sarin[4], P.Sawicki[3], H.Seals[2], I.Sedykh[2], W.Skulski[8], C.E.Smith[6], M.A.Stankiewicz[2], P.Steinberg[2], G.S.F.Stephans[4], A.Sukhanov[2], A.Szostak[2], J.-L.Tang[5], M.B.Tonjes[7], A.Trzupek[3], C.Vale[4], G.J.van Nieuwenhuizen[4], S.S.Vaurynovich[4], R.Verdier[4], G.I.Veres[4], P.Walters[8], E.Wenger[4], D.Willhelm[7], F.L.H.Wolfs[8], B.Wosiek[3], K.Wozniak[3], A.H.Wuosmaa[1], S.Wyngaardt[2], B.Wyslouch[4], J.Zhang[4]

1 Physics Division, Argonne National Laboratory, Argonne, IL, USA
2 Physics and C-A Departments, Brookhaven National Laboratory, Upton, NY, USA
3 Institute of Nuclear Physics, Krakow, Poland
4 Laboratory for Nuclear Science, Massachusetts Institute of Technology, Cambridge, MA, USA
5 Department of Physics, National Central University, Chung-Li, Taiwan
6 Department of Physics, University of Illinois at Chicago, Chicago, IL, USA
7 Department of Chemistry, University of Maryland, College Park, MD, USA
8 Department of Physics and Astronomy, University of Rochester, Rochester, NY, USA

Publications coauthored PHOBOS collaboration:

"Identified Charged Antiparticle to Particle Ratios near Midrapidity in Cu+Cu Collisions at sqrt(s_NN)=62.4 and 200 GeV", *Phys. Rev.* **C77**, 061901(R) (2008).

"The Importance of Correlations and Fluctuations on the Initial Source Eccentricity in High-Energy Nucleus-Nucleus Collisions", *Phys. Rev.* **C77**, 014906 (2008).

"Cluster properties from two-particle angular correlations in p+p collisions at sqrt(s) = 200 and 410 GeV", *Phys. Rev.* **C75**, 054913 (2007).

"System Size, Energy, Pseudorapidity, and Centrality Dependence of Elliptic Flow", *Phys. Rev. Lett.* **98**, 242302 (2007).

"Identified hadron transverse momentum spectra in Au+Au collisions at sqrt(s_NN)=62.4 GeV", *Phys. Rev.* **C75**, 024910 (2007).

"Centrality and Energy Dependence of Charged-Particle Multiplicities in Heavy Ion Collisions in the Context of Elementary Reactions", *Phys. Rev.* **C74**, 021902(R) (2006).

"Forward-Backward Multiplicity Correlations in sqrt(s_NN)=200 GeV Au+Au Collisions", *Phys. Rev.* **C74**, 011901(R) (2006).

"System size and centrality dependence of charged hadron transverse momentum spectra in Au+Au and Cu+Cu collisions at sqrt(s_NN)=62.4 and 200 GeV", *Phys. Rev. Lett.* **96**, 212301 (2006).

"Energy dependence of directed flow over a wide range of pseudorapidity in Au+Au collisions at RHIC", *Phys. Rev. Lett.* **97**, 012301 (2006).

"Charged Particle Pseudorapidity Distributions in Au+Au collisions at sqrt(s_NN) = 62.4 GeV", *Phys. Rev.* **C74**, 021901(R) (2006).

"The PHOBOS Perspective on Discoveries at RHIC", *Nucl. Phys.* **A757**, 28 (2005), BNL 73847-2005 Formal Report.

"Scaling of Charged Particle Production in d+Au Collisions at sqrt(s_NN)=200 GeV", *Phys. Rev.* **C72**, 031901(R) (2005).

"Charged antiparticle to particle ratios near midrapidity in p+p collisions at sqrt(s_NN) = 200 GeV", *Phys. Rev.* **C71**, 021901(R) (2005).

"Transverse momentum and rapidity dependence of HBT correlations in Au+Au collisions at sqrt(s_NN) = 62.4 and 200 GeV", *Phys. Rev.* **C73**, 031901(R) (2006).

"Centrality and pseudorapidity dependence of elliptic flow for charged hadrons in Au+Au collisions at sqrt(s_NN)= 200 GeV", *Phys. Rev.* **C72**, 051901(R) (2005).

"Energy dependence of elliptic flow over a large pseudorapidity range in Au+Au collisions at RHIC", *Phys. Rev. Lett.* **94**, 122303 (2005).

"Pseudorapidity dependence of charged hadron transverse momentum spectra in d+Au collisions at sqrt(s_NN)=200 GeV", *Phys. Rev.* **C70**, 061901(R) (2004).

"Collision Geometry Scaling of Au+Au pseudorapidity density from sqrt(s_NN) = 19.6 to 200 GeV", *Phys. Rev.* **C70**, 021902(R) (2004).

"Centrality dependence of charged hadron transverse momentum spectra in Au+Au collisions from sqrt(s_NN) = 62.4 to 200 GeV", *Phys. Rev. Lett.* **94**, 082304 (2005).

"Particle production at very low transverse momenta in Au+Au collisions at sqrt(s_NN)=200 GeV", *Phys. Rev.* **C70**, 051901(R) (2004).

"Pseudorapidity Distribution of Charged Particles in d+Au collisions at sqrt(s_NN)=200 GeV", *Phys. Rev. Lett.* **93**, 082301 (2004).

"Centrality dependence of charged antiparticle to particle ratios near mid-rapidity in d+Au collisions at sqrt(s_NN)=200 GeV", *Phys. Rev.* **C70**, 011901(R) (2004).

"Centrality Dependence of the Charged Hadron Transverse Momentum Spectra in d+Au Collisions at sqrt(sNN)=200 GeV", *Phys. Rev. Lett.* **91**, 072302 (2003).

"Charged hadron transverse momentum distributions in Au+Au collisions at sqrt(s_NN) = 200 GeV", *Phys. Lett.* **B578**, 297 (2004).

"Significance of the fragmentation region in ultrarelativistic heavy ion collisions", *Phys. Rev. Lett.* **91**, 052303 (2003).

"Ratios of charged antiparticles to particles near mid-rapidity in Au+Au collisions at sqrt(sNN)=200 GeV", *Phys. Rev.* **C67**, 021901(R) (2003).

"The PHOBOS Detector at RHIC", *Nucl. Inst. Meth.* **A499**, 603 (2003).

"Pseudorapidity and centrality dependence of the collective flow of charged particles in Au+Au collisions at sqrt(sNN)=130 GeV", *Phys. Rev. Lett.* **89**, 222301 (2002).

"Centrality Dependence of the Charged Particle Multiplicity near Mid-Rapidity in Au+Au Collisions at sqrt(sNN)=130 and 200 GeV", *Phys. Rev.* **C65**, 061901(R) (2002).

"Measurements of Mutual Coulomb Dissociation in sqrt(sNN)=130 GeV Au+Au Collisions, M. Chui, et al., RHIC ZDC Collaboration", *Phys. Rev. Lett,* **89** 012302 (2002).

"Energy dependence of particle multiplicities near mid-rapidity in central Au+Au collisions", *Phys. Rev. Lett.* **88**, 22302 (2002).

"Centrality Dependence of Charged Particle Multiplicity at Midrapidity in Au+Au Collisions at sqrt(sNN)=130 GeV", *Phys. Rev.* **C65**, 31901(R) (2002).

"Charged-particle pseudorapidity density distributions from Au+Au collisions at sqrt(sNN)=130 GeV", *Phys. Rev. Lett*. **87**, 102303 (2001).

"Ratios of charged particles to antiparticles near mid-rapidity in Au+Au collisions at sqrt(sNN)=130 GeV", *Phys. Rev. Lett.* **87**, 102301 (2001).

"Charged particle multiplicity near mid-rapidity in central Au+Au collisions at sqrt(s) = 56 and 130 AGeV", *Phys. Rev. Lett.* **85**, 3100 (2000).

Other publications:

R. Bindel, R. Baum, E. Garcia, A.C. Mignerey, and L.P. Remsberg, "Array of Cherenkov radiators for Phobos at RHIC", *Nucl. Inst. Meth.* **A488**, 94 (2002).

R. Bindel, E. Garcia, A.C. Mignerey, and L.P. Remsberg, "Array of Scintillator Counters for PHOBOS at RHIC", *Nucl. Instr. Meth.* **A474**, 38-45 (2001).

Appendix I: Systematic Error Figures

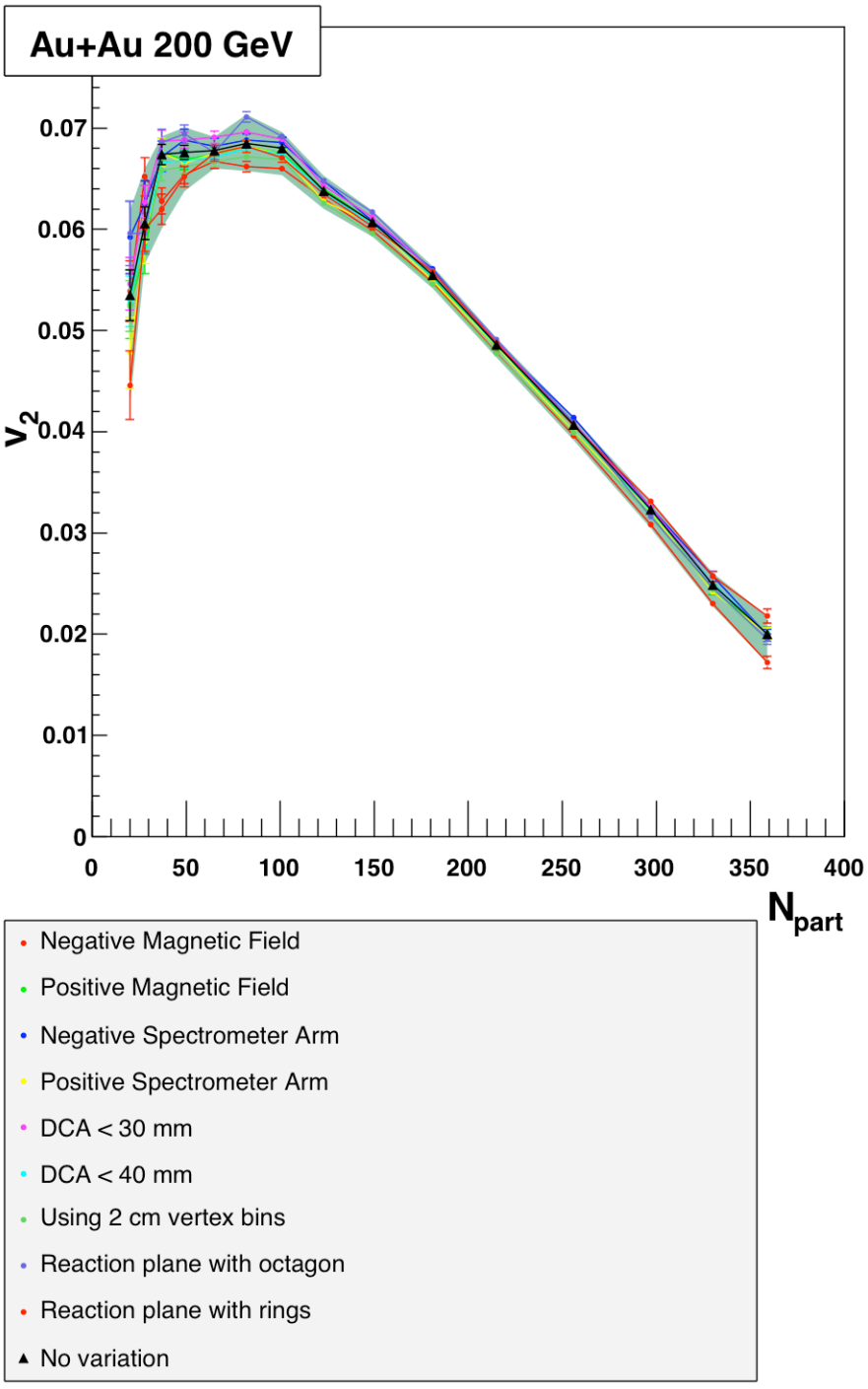

Figure I.1: These are the variations in $v_2(N_{part})$ for Au+Au collisions at $\sqrt{s_{NN}}$ = 200 GeV as several analysis parameters are changed. The black triangles show the standard result. The green band shows the limits of the systematic error, taken from these individual contributions as discussed in Sec. 5.11. The error bars represent 1σ statistical errors.

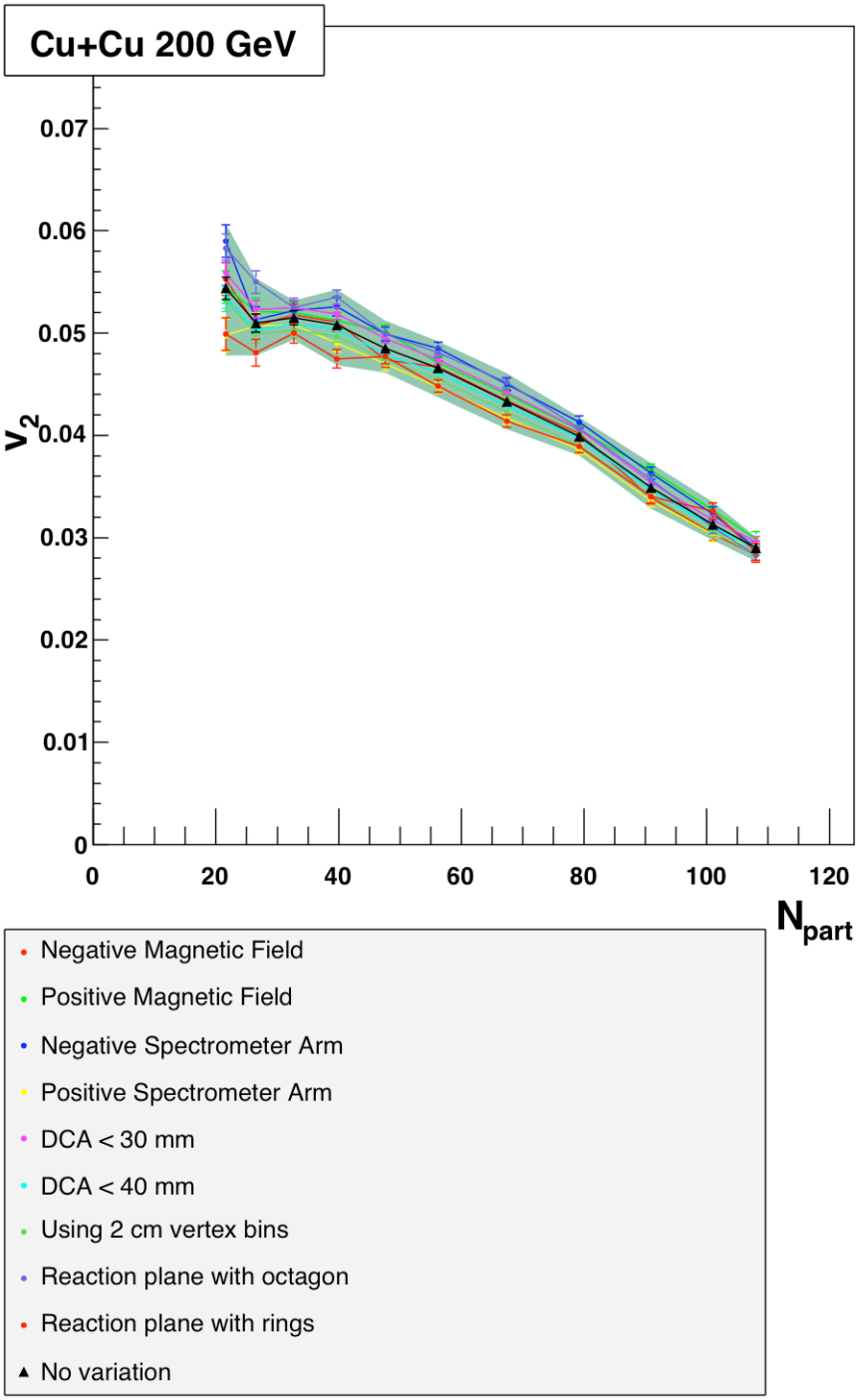

Figure I.2: These are the variations in $v_2(N_{part})$ for Cu+Cu collisions at $\sqrt{s_{NN}}$ = 200 GeV as several analysis parameters are changed. The black triangles show the standard result. The green band shows the limits of the systematic error, taken from these individual contributions as discussed in Sec. 5.11. The error bars represent 1σ statistical errors.

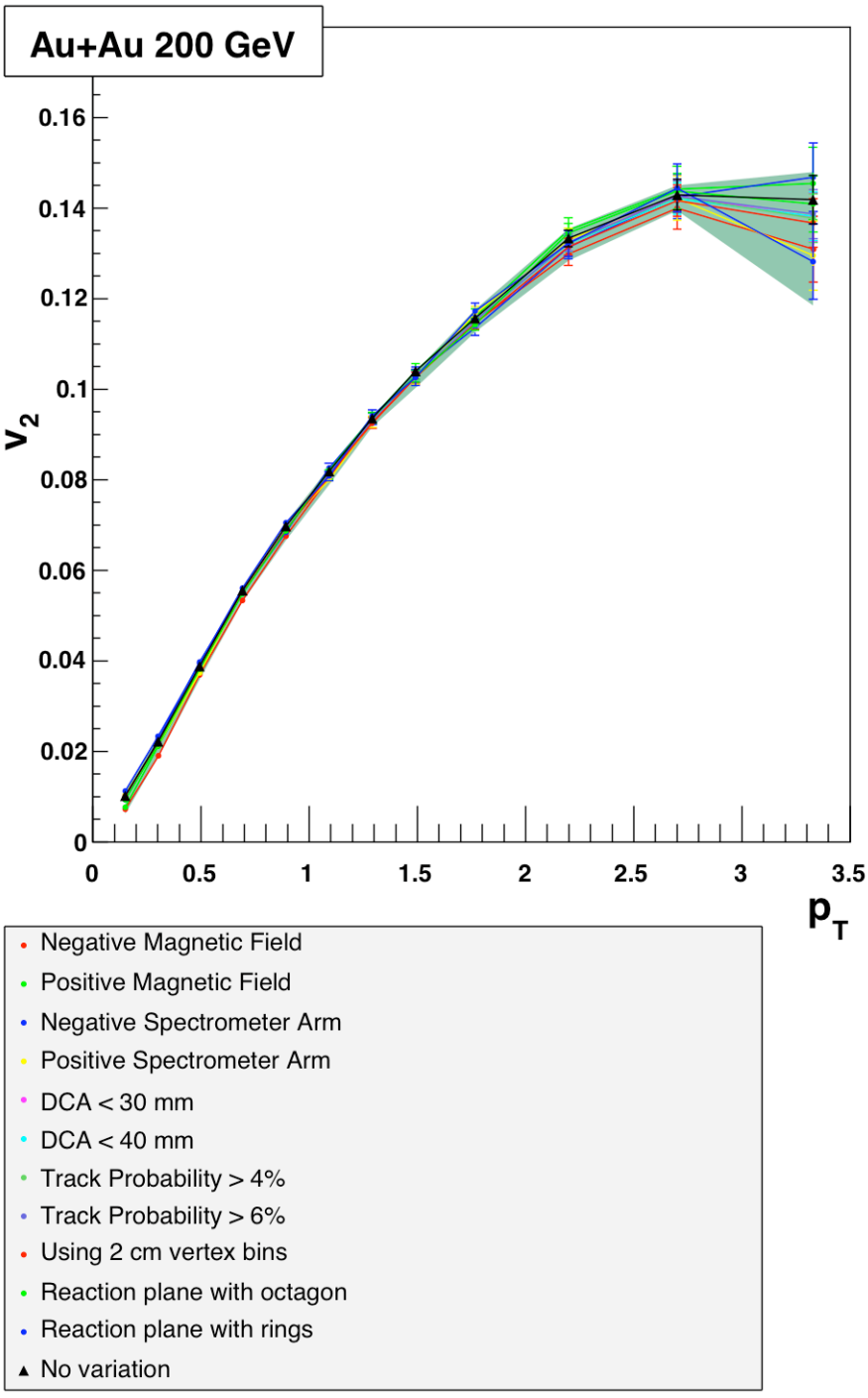

Figure I.3: These are the variations in $v_2(p_T)$ for Au+Au collisions at $\sqrt{s_{NN}}$ = 200 GeV as several analysis parameters are changed. The black triangles show the standard result. The green band shows the limits of the systematic error, taken from these individual contributions as discussed in Sec. 5.11. The error bars represent 1σ statistical errors.

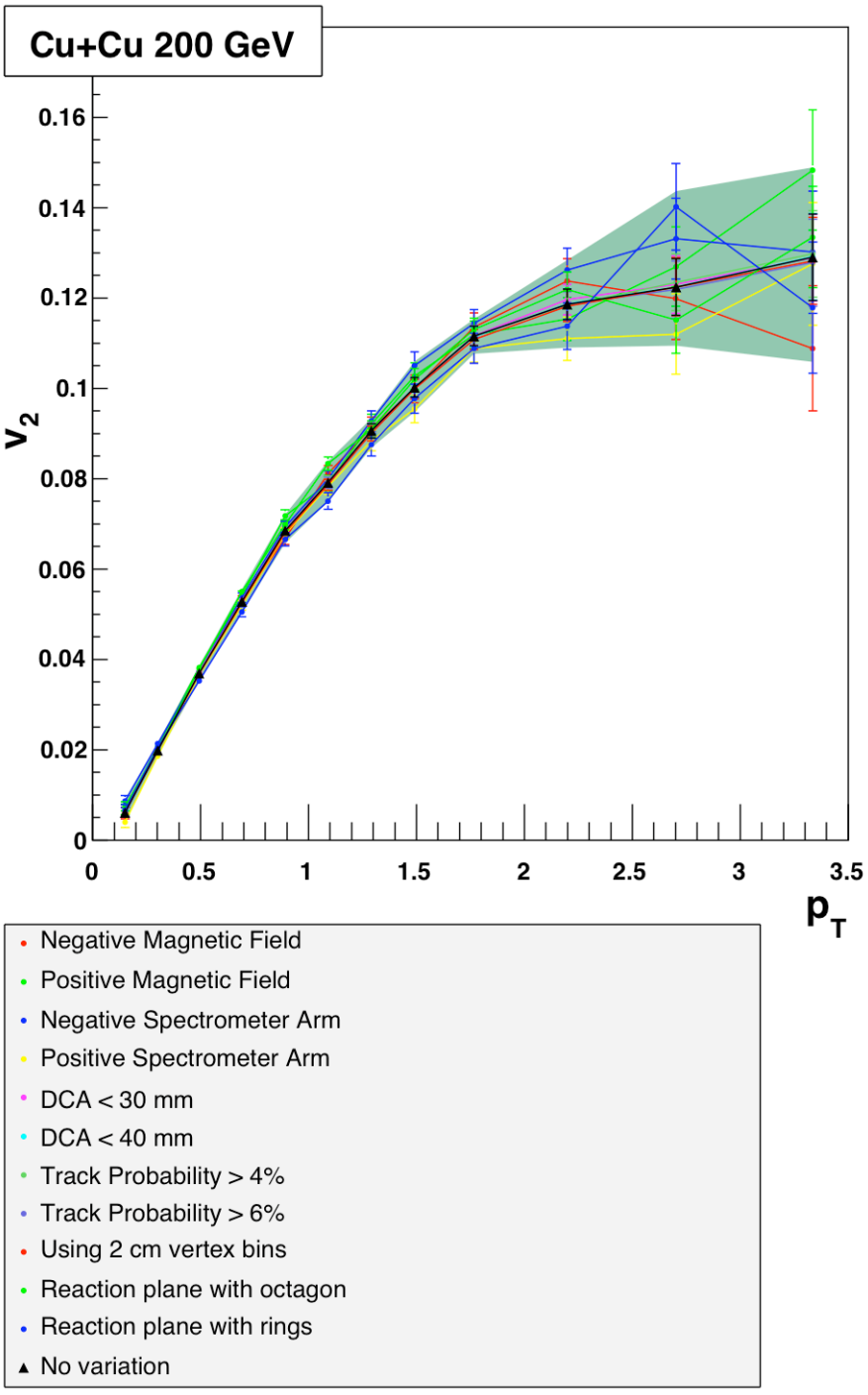

Figure I.4: These are the variations in $v_2(p_T)$ for Cu+Cu collisions at $\sqrt{s_{NN}}$ = 200 GeV as several analysis parameters are changed. The black triangles show the standard result. The green band shows the limits of the systematic error, taken from these individual contributions as discussed in Sec. 5.11. The error bars represent 1σ statistical errors.

Appendix J: Tracking Example

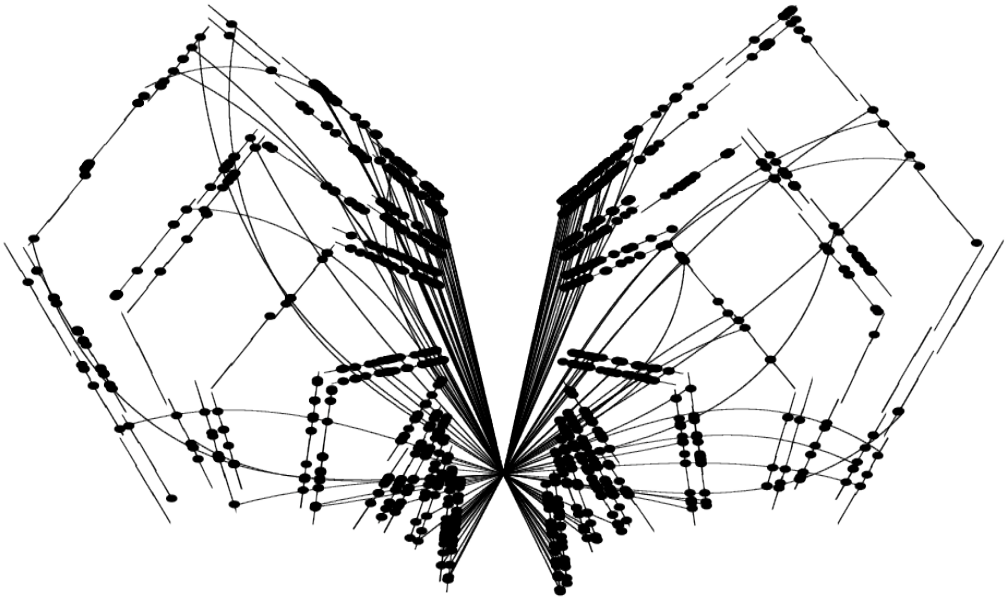

Figure J.1: Tracks reconstructed from hits in the PHOBOS spectrometer for Au+Au at 200 GeV [Gul04].

References:

Some citations refer to papers available on the arXiv preprint servers at *http://arxiv.org*.

[Abe07] B. I. Abelev, *et al.* [STAR Collaboration], "Mass, quark-number, and sqrt s(NN) dependence of the second and fourth flow harmonics in ultra-relativistic nucleus-nucleus collisions", *Phys. Rev. C* **75**, 054906 (2007).

[Abe08] B. I. Abelev, *et al.* [STAR Collaboration], "Centrality dependence of charged hadron and strange hadron elliptic flow from sqrt(s_NN) = 200 GeV Au+Au collisions", *Phys. Rev. C* **77**, 054901 (2008).

[Ack01] K. H. Ackermann, *et al.* [STAR Collaboration], "Elliptic flow in Au+Au collisions at sqrt(s_NN) = 130 GeV", *Phys. Rev. Lett.* **86**, 402 (2001).

[Ada05] J. Adams, *et al.* [STAR Collaboration], "Azimuthal Anisotropy in Au+Au Collisions at sqrt(sNN) = 200 GeV", *Phys. Rev. C* **72**, 014904 (2005).

[Adl03] S. S. Adler, *et al.* [PHENIX Collaboration], "Elliptic Flow of Identified Hadrons in Au+Au Collisions at sqrt(s_NN) = 200 GeV", *Phys. Rev. Lett.* **91**, 182301 (2003).

[Alt03] C. Alt, *et al.* [NA49 Collaboration], "Directed and elliptic flow of charged pions and protons in Pb+Pb collisions at 40A and 158A GeV", *Phys. Rev. C* **68**, 034903 (2003).

[Alv07] B. Alver, *et al.* [PHOBOS Collaboration], "System Size, Energy, Pseudorapidity, and Centrality Dependence of Elliptic Flow", *Phys. Rev. Lett.* **98**, 242302 (2007).

[Alv08a] B. Alver, *et al.*, "The PHOBOS Glauber Monte Carlo", arXiv:*nucl-ex/0805.4411v1*

[Alv08b] B. Alver, *et al.* [PHOBOS Collaboration], "Importance of correlations and fluctuations on the initial source eccentricity in high-energy nucleus-nucleus collisions", *Phys. Rev. C* **77**, 014906 (2008).

[Alv08c] B. Alver, *et al.* [PHOBOS Collaboration], "Identified Charged Antiparticle to Particle Ratios near Midrapidity in Cu+Cu Collisions at sqrt(s_NN)=62.4 and 200 GeV", accepted for publication in *Phys. Rev. C*. arXiv:*nucl-ex/0802.1695*

[Alv08d] B. Alver, *et al.* [PHOBOS Collaboration], "Elliptic flow fluctuations in Au+Au collisions at sqrt(s_NN) = 200 GeV", submitted for publication in *Phys. Rev. Lett.* arXiv:*nucl-ex/0702036*

[And06] A. Andronic, P. Braun-Munzinger, and J. Stachel. "Hadron production in central nucleus nucleus collisions at chemical freeze-out", *Nucl. Phys. A* **772**, 167 (2006).

[Ani80] R. Anishetty, P. Koehler, and L. McLerran, "Central collisions between heavy nuclei at extremely high energies: The fragmentation region", *Phys. Rev. D* **22**, 2793 (1980).

[ARW99] M. Alford, K. Rajagopal, and F. Wilczek, "Color-Flavor Locking and Chiral Symmetry Breaking in High Density QCD", *Nucl. Phys. B* **537**, 443 (1999).

[Bac03] B. B. Back, *et al.* [PHOBOS Collaboration], "The PHOBOS Detector at RHIC", *Nucl. Inst. Meth. A* **499**, 603 (2003).

[Bac05a] B. B. Back, *et al.* [PHOBOS Collaboration], "The PHOBOS perspective on discoveries at RHIC", *Nucl. Phys. A* **757**, 28 (2005).

[Bac05b] B. B. Back, *et al.* [PHOBOS Collaboration], "Centrality and pseudorapidity dependence of elliptic flow for charged hadrons in Au+Au collisions at sqrt(s_NN)= 200 GeV", *Phys. Rev. C* **72**, 051901(R) (2005).

[Bac07] B. B. Back, *et al.* [PHOBOS Collaboration], "Identified hadron transverse momentum spectra in Au+Au collisions at sqrt(s_NN) = 62.4", *Phys. Rev. C* **75**, 024910 (2007).

[Bak04] M. Baker, private communication (2004).

[Bar97] J.Barrette, *et al.*, "Proton and pion production relative to the reaction plane in Au + Au collisions at 11A GeV/c", *Phys. Rev. C* **56**, 3254 (1997).

[Bau98] G. Baur, K. Hencken, and D. Trautmann, "Photon-photon physics in very peripheral collisions of relativistic heavy ions", *J. Phys. G* **24**, 1657 (1998).

[Bia76] A. Bialas, M. Bleszynski, and W. Czyz, "Multiplicity Distributions In Nucleus-Nucleus Collisions At High-Energies", *Nucl. Phys. B* **111**, 461 (1976).

[Bin01] R. Bindel, *et al.*, "Array of Scintillator Counters for PHOBOS at RHIC", *Nucl. Instr. Meth. A* **474**, 38 (2001).

[Bjo83] J. D. Bjorken, "Highly relativistic nucleus-nucleus collisions: The central rapidity region", *Phys. Rev. D* **27**, 140 (1983).

[Bor00] N. Borghini, P. M. Dinh, and J.-Y. Ollitrault, “Is the analysis of flow at the CERN Super Proton Synchrotron reliable?”, *Phys. Rev. C* **62**, 034902 (2000).

[Bor01] N. Borghini, P. M. Dinh, and J.-Y. Ollitrault, “New method for measuring azimuthal distributions in nucleus-nucleus collisions”, *Phys. Rev. C* **63**, 054906 (2001).

[Cas79] A. Casher, H. Neuberger, and S. Nussinov, “Chromoelectric flux tube model of particle production”, *Phys. Rev. D* **20**, 179 (1979).

[Che07] X. Cheng, *et al.*, “Collective Behavior in a Granular Jet: Emergence of a Liquid with Zero Surface Tension”, *Phys. Rev. Lett.* **99**, 188001 (2007).

[Cho74] A. Chodos, *et al.*, “A New Extended Model Of Hadrons”, *Phys. Rev. D* **9**, 3471 (1974).

[Com95] G. Compagno, G. M. Palma, R. Passante, and F. Persico, “Atoms dressed and partially dressed by the zero-point fluctuations of the electromagnetic field”, *J. Phys. B* **28**, 1105 (1995.)

[Coo56] L. N. Cooper, “Bound Electron Pairs in a Degenerate Fermi Gas", *Phys. Rev.* **104**, 1189 (1956).

[Cre83] M. Creutz, *Quarks, Gluons and Lattices*. Cambridge University Press, Cambridge, U.K. (1983).

[Csa04] M. Csanad, T. Csorgo, and B. Lorstad, “Buda-Lund hydro model and the elliptic flow at RHIC”, *Nukleonika* **49**, S45 (2004).

[Cse06] L. P. Csernai, J. I. Kapusta, and L. D. McLerran, “On the Strongly-Interacting Low-Viscosity Matter Created in Relativistic Nuclear Collisions”, *Phys. Rev. Lett.* **97**, 152303 (2006).

[Dan88] P. Danielewicz, *et al.*, “Collective motion in nucleus-nucleus collisions at 800 MeV/nucleon”, *Phys. Rev. C* **38**, 120 (1988).

[deV87] H. de Vries, C. W. de Jager, and C. de Vries, “Nuclear Charge-Density-Distribution Parameters from Elastic Electron Scattering”, *Atom. Data Nucl. Data Tabl.* **36**, 495 (1987).

[Fei98] E. L. Feinberg, "A wonderful story about a remarkable paper by Landau", *Phys.-Usp.* **41**, 617 (1998).

[Fey63] R. P. Feynman, R. B. Leighton, and M. Sands, *The Feynman lectures on physics*. Addison-Wesley Pub. Co., Reading, Mass. (1963-65).

[Gar07] E.Garcia, *et al.*, "Vertex Reconstruction Using a Single Layer Silicon Detector", *Nucl. Inst. Meth. A* **570**, 536 (2007).

[Gri89] D. Griffiths, *Introduction to Elementary Particles*, Wiley, New York, NY. (1989).

[GW73] D. J. Gross and F. Wilczek, "Asymptotically free gauge theories. I", *Phys. Rev. D* **8**, 3633 (1973).

[Han01] S. Hands, "The Phase Diagram of QCD", *Contemp. Phys.* **42**, 209 (2001).

[Har96] J. W. Harris, B. Müller, "The Search for the Quark-Gluon Plasma", *Annu. Rev. Nucl. Part. Sci.* **46**, 71 (1996).

[Hei99] H. Heiselberg, and A. Levy, "Elliptic Flow and HBT in non-central Nuclear Collisions", *Phys.Rev. C* **59**, 2716 (1999).

[Hol05] R. S. Hollis, "Centrality Evolution of Charged-Particles Produced in Ultra-Relativistic Au+Au and d+Au Collisions", PhD dissertation, University of Illinois at Chicago (2005).

[Hug81] R. J. Hughes, "More comments on asymptotic freedom", *Nucl. Phys. B* **186**, 376 (1981).

[Kar02] F. Karsch, "Lattice results on QCD thermodynamics", *Nucl. Phys. A* **698**, 199 (2002).

[Kei76] B. D. Keister and L. S. Kisslinger, "Free Quark Phases In Dense Stars", *Phys. Lett.* **64B**, 117 (1976).

[KH03] P. Kolb, U. Heinz, "Hydrodynamic description of ultrarelativistic heavy-ion collisions" in *Quark Gluon Plasma 3*: R.C. Hwa and X.-N. Wang, Eds., World Scientific, Singapore (2004).

[Kol03] P. F. Kolb, "v4 - A small, but sensitive observable for heavy ion collisions", *Phys. Rev. C* **68**, 031902 (2003).

[Kov02] Y.V. Kovchegov and K.L. Tuchin, "Elliptic flow from minijet production in heavy ion collisions", *Nucl. Phys. A* **708**, 413 (2002).

[Kov05] P. K. Kovtun, D. T. Son, and A. O. Starinets, "Viscosity in Strongly Interacting Quantum Field Theories from Black Hole Physics", *Phys. Rev. Lett.* **94**, 111601 (2005).

[Lan53] L.D. Landau, "On the multiple production of particles in high energy collisions", *Izv. Akad. Nauk Ser. Fiz.* **17**, 51 (1953).

[Man06] S. Manly, "System size, energy and pseudorapidity dependence of directed and elliptic flow at RHIC", *Nucl. Phys. A* **774**, 523 (2006).

[McL03] L. McLerran, "The Quark Gluon Plasma and The Color Glass Condensate: 4 Lectures", arXiv:*hep-ph/0311028v1* (2003).

[Mil07] M. L. Miller, K. Reygers, S. J. Sanders and P. Steinberg, "Glauber Modeling in High-Energy Nuclear Collisions", *Annu. Rev. Nucl. Part. Sci.* **57**, 205 (2007).

[Nie81] N. K. Nielsen, "Asymptotic freedom as a spin effect", *Am. J. Phys.* **49**, 1171 (1981).

[Nou07] R. Nouicer, "Elliptic flow and initial eccentricity in Cu+Cu and Au+Au collisions at RHIC", *J. Phys. G* **34**, S887 (2007).

[OHa02] K. M. O'Hara, *et al.*, "Observation of a Strongly Interacting Degenerate Fermi Gas of Atoms", *Science* **298**, 2179 (2002).

[Oll93] J.-Y. Ollitrault, "Determination of the reaction plane in ultrarelativistic nuclear collisions", *Phys. Rev. D* **48**, 1132 (1993).

[Ols86] M. G. Olsson and C. Suchyta, "Quark vacuum polarization and the luscher term", *Phys. Rev. Lett.* **57**, 37 (1986).

[PV98] A. M. Poskanzer and S. A. Voloshin. "Methods for analyzing anisotropic flow in relativistic nuclear collisions", *Phys. Rev. C* **58**, 1671 (1998).

[Rhic00] "RHIC Design Manual", *http://www.agsrhichome.bnl.gov/NT-share/rhicdm/00_toc1i.htm*, accessed May 2008.

[Rio92] M. Riordan, "The Discovery of Quarks", *Science* **256**, 1287 (1992).

[Ris96a] D. H. Rischke and M. Gyulassy, "The Maximum Lifetime of the Quark-Gluon Plasma", *Nucl. Phys. A* **597**, 701 (1996).

[Ris96b] D. H. Rischke, "Hydrodynamics and collective behaviour in relativistic nuclear collisions", *Nucl. Phys. A* **610**, 88c (1996).

[Roh94] J. W. Rohlf, *Modern Physics from α to Z^0*. Wiley, New York, NY (1994).

[Roy99] D. P. Roy, "Basic Constituents of Matter and their Interactions - A Progress Report", arXiv:*hep-ph/9912523v1* (1999).

[Son08] H. Song and U. W. Heinz, "Multiplicity scaling in ideal and viscous hydrodynamics", arXiv:*nucl-th/0805.1756v1* (2008). Submitted to *Phys. Rev. C*.

[Sor03] P.R. Sorenson, "Kaon and Lambda Production at Intermediate pT: Insights into the Hadronization of the Bulk Partonic Matter Created in Au+Au Collisions at RHIC", PhD dissertation, University of California (2003).

[Stei05] P. Steinberg, "Landau Hydrodynamics and RHIC Phenomena", *Acta Phys. Hung. A* **24**, 51 (2005).

[Step04] M. A. Stephanov, "QCD phase diagram and the critical point", *Prog. Theor. Phys. Suppl.* **153**, 139 (2004)

[Stes01] D.B. Steski, et al., "Operation of the RHIC Au Ion Source", BNL Report Number 68730. OSTI ID 789434. (2001).

[Tea02] D. Teaney, J. Lauret, and E. V. Shuryak, "Hydro+Cascade, Flow, the Equation of State, Predictions and Data", *Nucl. Phys. A* **698**, 479, (2002).

[Val04] C.M. Vale, "Elliptic Flow in Au+Au Collisions at 200 GeV per Nucleon Pair", PhD dissertation, Massachusetts Institute of Technology (2004).

[Vol00] S. A. Voloshin and A. M. Poskanzer, "The physics of the centrality dependence of elliptic flow", *Phys. Lett. B* **474**, 27 (2000).

[Vol07] S. A. Voloshin, "Energy and system size dependence of charged particle elliptic flow and v_2/ε scaling", *J. Phys. G* **34**, S883 (2007).

[Wan91] X.-N. Wang, M. Gyulassy, "HIJING: A Monte Carlo model for multiple jet production in pp, pA, and AA collisions", *Phys. Rev. D* **44**, 3501 (1991).

[Wit84] E. Witten, "Cosmic Separation Of Phases", *Phys. Rev. D* **30**, 272 (1984).

[Woz06] K. Woźniak, "Vertex reconstruction algorithms in the PHOBOS experiment at RHIC", *Nucl. Inst. and Meth. A* **566**, 185 (2006).

[WS54] R. D. Woods and D. S. Saxon, "Diffuse Surface Optical Model for Nucleon-Nuclei Scattering", *Phys. Rev.* **95**, 577 (1954).

[Yao06] W.-M. Yao, *et al.* [Particle Data Group], "Review of Particle Physics", *J. Phys. G* **33**, 1, (2006).